

TECHNISCHE UNIVERSITÄT MÜNCHEN

Fakultät für Medizin

The site of initial activation determines the central nervous system infiltration characteristics of T helper cells in a preclinical model of multiple sclerosis

Michael Thomas Hiltensperger

Vollständiger Abdruck der von der Fakultät für Medizin der Technischen Universität München zur Erlangung des akademischen Grades eines

Doktors der Naturwissenschaften

genehmigten Dissertation.

Vorsitz: Prof. Dr. Marc Schmidt-Supprian

Prüfer der Dissertation:

1. Prof. Dr. Thomas Korn
2. Prof. Dr. Dietmar Zehn
3. Prof. Dr. Alexander Flügel

Die Dissertation wurde am 27.12.2021 bei der Technischen Universität München eingereicht und durch die Fakultät für Medizin am 08.11.2022 angenommen.

Table of contents

1	Abbreviations	i
2	Summary	v
3	Zusammenfassung	vi
4	Introduction	1
4.1	Organ-specific autoimmunity	1
4.1.1	Multiple sclerosis	2
4.1.2	Experimental autoimmune encephalomyelitis	3
4.2	T helper cell subsets	4
4.2.1	T cell development in the thymus.....	5
4.2.2	T cell priming	5
4.2.3	T cell plasticity	6
4.2.4	Impact of environmental cues on the T cell phenotype	7
4.2.5	T cell trafficking to the CNS	8
4.3	Spatiotemporal labeling of CD4 ⁺ T cells	10
4.3.1	Photoconvertible fluorescent proteins (PFPs)	10
4.3.2	Photoactivatable mitochondria mouse line	12
4.4	Aim of the study	12
5	Material and methods	14
5.1	Materials	14
5.1.1	Instruments.....	14
5.1.2	Consumables.....	15
5.1.3	Chemicals and reagents	15
5.1.4	Buffers and solutions	17
5.1.5	Kits	19
5.1.6	Antibodies.....	19
5.1.7	Oligonucleotides	21
5.1.8	Software	22
5.2	Methods	24

5.2.1	Animals and animal-related procedures.....	24
5.2.1.1	Animals	24
5.2.1.2	Earmarking and tail biopsy collection.....	24
5.2.1.3	FTY720 treatment.....	25
5.2.1.4	EAE induction.....	25
5.2.1.5	OVA immunization.....	26
5.2.1.6	Surgical lymph node preparation for photoconversion and two-photon imaging.....	26
5.2.1.7	Adoptive transfer of T cells	27
5.2.2	Extraction of genomic DNA and PCR-based genotyping	27
5.2.3	Cell isolation and cell cultures.....	29
5.2.3.1	Preparation of single cell suspension and isolation of mononuclear cells from the CNS.....	29
5.2.3.2	Cultures for retrovirus production.....	29
5.2.3.3	Retroviral T cell transduction	29
5.2.3.4	³ H thymidine incorporation assay.....	30
5.2.4	Immunohistochemistry.....	30
5.2.5	Two-photon imaging of Ca ²⁺ signaling in transduced T cells.....	30
5.2.6	Flow cytometry analysis and cell sorting.....	31
5.2.6.1	Surface antigen staining	31
5.2.6.2	Intracellular antigen staining	31
5.2.6.3	Tetramer staining.....	32
5.2.6.4	Cell hashing for scRNA-seq.....	32
5.2.6.5	Fluorescence-activated cell sorting.....	32
5.2.7	Sequencing	32
5.2.7.1	scRNA-seq	32
5.2.7.2	scRNA-seq data processing	33
5.2.7.3	RNA-seq.....	34
5.2.7.4	ATAC-seq.....	35
5.2.8	Quantification and statistical analysis	35

5.2.9	Data availability	36
6	Results	37
6.1	Characterization of light-mediated CD4 ⁺ T cell labeling	37
6.2	Lymph node dynamics of CD4 ⁺ T cells in naïve and immunized mice	38
6.3	Migration pattern of i- and m-T cells during CNS autoimmunity	41
6.4	i- and m-T cells in the CNS are distinct	43
6.5	Antigen-specific priming of CD4 ⁺ T cells occurs in iLN and mLN	44
6.6	Clonal expansion of i- and m-T cells.....	47
6.7	i- and m-T cells show a distinct phenotype	49
6.8	Imprinting of a specific core signature is based on the priming site	52
6.9	i- and m-T cells show differential transcription factor activity	54
6.10	i- and m-T cell gene signatures are robust in alternative models	56
6.11	CNS infiltration pattern is distinct in i- and m-T cells.....	58
6.12	CNS infiltration pattern of m-T cells resembles <i>Cxcr6</i> ^{-/-} T cells	62
7	Discussion	63
7.1	The PhAM ^T mouse line for provenance-guided study of T cells.....	63
7.2	iLN and mLN are unique priming sites for CNS-infiltrating T cells.....	64
7.3	i- and m-T cells constitute distinct T cell subsets during EAE	66
7.4	Integrity of the site-specific priming effects in alternative settings.....	70
7.5	Functional phenotypes of CNS-infiltrating i- and m-T cells	70
7.6	Deciphering the underlying factors for differential CNS homing.....	71
7.7	The role of tissue imprinting of immune cells on the immunopathology in remote organs.....	72
8	Bibliography.....	73
9	Appendix	84
9.1	List of figures.....	84
9.2	List of tables.....	84
9.3	Attributions	85
9.4	Acknowledgements	86

1 Abbreviations

%	percentage
°C	degree Celsius
2D2	transgenic T cell receptor (TCR) ^{MOG}
AFN	atipamezole, flumazenil, and naloxone
AhR	aryl hydrocarbon receptor
APCs	antigen-presenting cells
AT	adoptive transfer
ATAC-seq	assay for transposase-accessible chromatin with sequencing
BBB	blood-brain barrier
BCR	B cell receptor
bp	base pairs
BST	brainstem
c.p.m.	count per minute
CD29	β1-integrin
CD49d	α4-integrin
CD62L	L-selectin
CFA	complete Freund's adjuvants
CLA	cutaneous lymphocyte antigen
CLP	common lymphoid progenitor
CLR	centered log ratio
CNS	central nervous system
CSF	cerebrospinal fluid
cTECs	cortical thymic epithelial cells
DCs	dendritic cells
DN	"double negative"
DP	"double positive"
DR15	HLA DRB1*1501 allele
EAE	experimental autoimmune encephalomyelitis
eATP	extracellular adenosine triphosphate
FC	fold change
g	gram
<i>g</i>	gravitational acceleration
GFP	green fluorescent protein
GM	grey matter
GSEA	gene set enrichment analysis

h	hour
HEVs	high endothelial venules
HLA	human leucocyte antigen
HTO	hashtag oligonucleotide
i.v.	intravenous
IFN- γ	interferon γ
IL-17	interleukin 17
IL-4	interleukin 4
iLN	inguinal lymph node
i-T cells	iLN- derived T cells
Itga4	α 4-integrin
Itgb1	β 1-integrin
l	liter
LFA-1	α L β 2-integrin
LNs	lymph nodes
MAdCAM-1	mucosal addressin cell adhesion molecule-1
mD2	mito-Dendra2
mD2 ^{GR}	mD2 ^{GREEN}
MFI	mean fluorescent intensity
mg	milligram (10^{-3} g)
MHC	major histocompatibility complexes
min	minute
ml	milliliter (10^{-3} l)
mLN	mesenteric lymph node
mm	millimeter (10^{-3} m)
mM	millimolar (10^{-3} M)
MMF	cocktail of medetomidine, midazolam and fentanyl
MOG	myelin oligodendrocyte glycoprotein
MS	multiple sclerosis
m-T cells	mLN- derived T cells
mTECs	medullary thymic epithelial cells
OVA	ovalbumin
PEI	polyethylenimine
PFA	paraformaldehyde
PFPs	photoconvertible fluorescent proteins
pH	power of hydrogen, a measure of hydrogen ion concentration
PhAM	photoactivatable mitochondria

PML	progressive multifocal leukoencephalopathy
PRMS	progressive-relapsing MS
PTx	pertussis toxin
RNA-seq	RNA sequencing
ROI	region of interest
RRMS	relapsing-remitting MS
s	second
s.c.	subcutaneous
S1P	sphingosine-1-phosphate
S1P1	sphingosine-1-phosphate receptor-1
SAA	serum amyloid A
SC	spinal cord
SC(L)	lumbar spinal cord
SCFAs	short-chain fatty acids
scRNA-seq	single cell RNA sequencing
scTCR-seq	single cell TCR sequencing
SFB	segmented filamentous bacterium
SP	“single-positive”
SPMS	secondary progressive MS
Tcm	central memory T cells
Tcon	conventional T
TCR	T cell receptor
Tem	effector memory T cells
Tfh	T follicular helper
TH	transgenic B cell receptor (BCR) ^{MOG}
Th	T helper
TRBV	T cell receptor β -chain variable
Treg	regulatory T
TRM	resident memory T
tSNE	t-distributed stochastic neighbour embedding
TSO	template switch oligo
UMI	unique molecular identifier
v/v	volume/volume
VLA-4	$\alpha 4\beta 1$ -integrin
w/v	mass/volume
WM	white matter
WT	wild-type

Δ RN	delta normalized reporter value
μ g	microgram (10^{-6} g)
μ l	microliter (10^{-6} l)
μ m	micrometer (10^{-6} m)
μ M	micromolar (10^{-6} M)

2 Summary

T helper cells have long been categorized according to signature cytokines specific for Th1 cells (IFN- γ), Th2 cells (IL-4), and Th17 cells (IL-17). Autoimmune diseases have been used as paradigms to illustrate the distinct functions of T helper cell subsets. For instance, organ-specific autoimmune disorders have been considered as Th1 diseases, and more recently as Th17 diseases. The pathogenic concept for most autoimmune disorders posits that autoreactive T cells are primed in the systemic immune compartment before they invade the target tissue and initiate immunopathology. However, recent multidimensional single cell analyses of T cells derived from the target tissue of autoimmune diseases have not found bona fide Th1 cells or Th17 cells, fueling the debate about either extensive plasticity or "mixed" priming of T helper cell subsets *in vivo*. In this work, I developed an experimental framework to probe the idea that the site of priming in the systemic immune compartment imprints unique effector properties in T helper cells with distinct consequences for the immunopathology they induce in remote organs. By site-specific *in vivo* labeling of antigen-specific T cells in different peripheral lymph node stations, I could show that myelin-specific T cells isolated from the central nervous system (CNS) (in a paradigmatic CNS autoimmune disease) are distinct depending on whether they were primed in skin-draining inguinal (i) or gut-draining mesenteric (m) lymph nodes. While i-T cells were positive for Cxcr6 and β 1-integrins, m-T cells expressed α 4-integrins and were predominantly negative for Cxcr6. Notably, m-T cells infiltrated primarily the white matter of the CNS. In contrast, i-T cells were recruited to grey matter as well as white matter. Introducing the definition of T helper cell subsets based on their site of peripheral priming might open a new and relevant avenue to understand and productively intervene with T helper cell biology in various target tissues of autoimmune diseases.

3 Zusammenfassung

T-Helferzellen werden seit langem nach charakteristischen Zytokinen kategorisiert, die für TH1-Zellen (IFN- γ), TH2-Zellen (IL-4) und TH17-Zellen (IL-17) spezifisch sind. Autoimmunerkrankungen wurden als klinische Paradigmen verwendet, um die unterschiedlichen Funktionen von T-Helferzellen-Kategorien zu veranschaulichen. Organspezifische Autoimmunerkrankungen wurden beispielsweise als TH1-Erkrankungen und neuerdings als TH17-Erkrankungen betrachtet. Das pathogene Konzept für die meisten Autoimmunerkrankungen geht davon aus, dass autoreaktive T-Zellen im systemischen Immunkompartiment geprimt werden, bevor sie in das Zielgewebe eindringen und Immunpathologie initiieren. Jüngste multidimensionale Einzelzellanalysen von T-Zellen, die aus dem Zielgewebe von Autoimmunerkrankungen stammen, haben jedoch keine echten TH1-Zellen oder TH17-Zellen gefunden, was die Debatte über entweder ausgeprägte Plastizität oder "gemischtes" Priming von T-Helferzell-Kategorien *in vivo* befeuert. In der vorliegenden Arbeit habe ich einen experimentellen Ansatz entwickelt, um zu testen, ob der Ort des Primings von T-Helferzellen im systemischen Immunkompartiment determiniert, welche Effektoreigenschaften diese T Zellen in distalen Organen aufweisen und welche Art von Immunpathologie sie dort induzieren. Durch ortsspezifische *in vivo* Markierung antigenspezifischer T-Zellen in verschiedenen peripheren Lymphknotenstationen konnte ich zeigen, dass aus dem autoimmun-entzündlichen zentralen Nervensystem (ZNS) isolierte myelinspezifische T-Zellen unterschiedlich sind, je nachdem ob sie in hautdränierenden inguinalen (i) oder darmdränierende mesenterialen (m) Lymphknoten geprimt wurden. Während i-T-Zellen positiv für Cxcr6 und β 1-Integrine waren, exprimierten m-T-Zellen α 4-Integrine und waren überwiegend negativ für Cxcr6. Bemerkenswerterweise infiltrierten m-T-Zellen hauptsächlich die weiße Substanz des ZNS. Im Gegensatz dazu wurden i-T-Zellen sowohl in die graue Substanz als auch in die weiße Substanz rekrutiert. Eine molekulare Kategorisierung von T-Helferzellen basierend auf dem Ort ihres peripheren Primings könnte neue Wege eröffnen, die Biologie von T-Helferzellen im Zielgewebe von Autoimmunerkrankungen besser zu verstehen und therapeutisch zu manipulieren.

4 Introduction

The immune system has been shaped and optimized over millions of years, starting from a simple apparatus in invertebrates, plants, and fungi to a highly complex network in vertebrates. Its function is to protect the organism against a plethora of dangers in the form of pathogens and even cancer. In its complex form it uses an early line of defense, called the innate immune system, and a second line of defense, termed the adaptive immune system. The innate immune system is evolutionary the older one of the two and is present to some extent in all species (Suckale et al., 2005). Its host defense mechanisms include prevention of pathogen entry by structural barriers, like the skin, phagocytosis of pathogens, and complement activation (Suckale et al., 2005). In contrast, the adaptive immune system is only present in vertebrates and developed approximately 500 million years ago in jawed fish (Flajnik and Kasahara, 2010). The adaptive immune system is comprised of a cellular part (T and B lymphocytes) and a humoral part (antibodies) which equip us with an immunologic memory regarding previous encounters with pathogens. However, when the immune system that normally only recognizes and destroys infectious agents (e.g. viruses and bacteria) instead targets self-antigens, autoimmunity and autoimmune tissue destruction can be a consequence (Cho and Gregersen, 2011).

4.1 Organ-specific autoimmunity

Autoimmune diseases present a huge social and economical burden and are the third leading cause of morbidity and mortality after cancer and heart disease in the industrial world (Harel and Shoenfeld, 2006). There are over 80 different disorders that can affect almost every organ in the human body (Selgrade et al., 1999) and the cause for most autoimmune diseases is still unclear despite tremendous scientific effort. In general, for an autoimmune disease to occur it is believed that auto-reactive T cells are activated by self-antigen-presenting dendritic cells (DCs) (Benson et al., 2010). The underlying risk factors for developing an autoimmune disease are considered to be multifactorial and can be grouped into genetic (e.g. polymorphisms in human leucocyte antigen (HLA) genes), immune (e.g. defects in regulatory T (Treg) cells, immunoglobulin deficiencies), hormonal (e.g. thymic hormones, corticosteroids), and environmental factors (e.g. infections, antibiotics, diet) (Brickman and Shoenfeld, 2001; Shoenfeld et al., 2008; Shoenfeld and Isenberg, 1989).

We distinguish between systemic autoimmune diseases, like systemic lupus erythematosus, rheumatoid arthritis, and Sjögren's syndrome, that affect multiple organs and organ-specific autoimmune diseases that target a particular organ or tissue. Patients with Graves disease for example suffer from an autoimmune response against their thyroid gland (Girgis et al., 2011), whereas patients with type 1 diabetes have their pancreatic beta cells targeted (Katsarou et

al., 2017), and patients with multiple sclerosis (MS) mount an autoimmune response against their central nervous system (CNS) (Compston and Coles, 2008).

4.1.1 Multiple sclerosis

MS is considered an immune-mediated chronic disabling disease of the CNS. As a consequence of inflammation within the CNS, patients suffer from a loss of myelin sheaths that surround axons and are crucial for signal transduction (Alizadeh et al., 2015). This can result in multiple areas of scarring, known as sclerosis, and causes a variety of neurological symptoms, including muscle weakness, tingling and numbness, fatigue, loss of vision, and balance problems or bladder issues (Ghasemi et al., 2017). It is hypothesized that autoreactive B and T cells are activated in the periphery, cross the blood-brain barrier (BBB) and initiate an autoimmune response against antigens in the CNS (Hemmer et al., 2015). This has been demonstrated in animal models for MS and likely also occurs in humans.

The BBB allows for strict control of exchange of molecules, ions, and cells between the blood and the CNS, which is mainly orchestrated by BBB endothelial cells and is essential for maintaining CNS homeostasis (Daneman and Prat, 2015). Historically, the CNS was considered “immune-privileged” due to its unique compartmentalization from the peripheral immune system precluding the entry of cellular or humoral constituents of the systemic immune compartment into the CNS. However, more recently it has become evident that there is indeed an intense surveillance of the CNS by the immune system with DCs and T cells patrolling the CNS, which is critical to fend off certain infections (Ousman and Kubes, 2012). The mechanisms of immune surveillance of the meningeal space and the CNS parenchyma might be different and the patho-anatomical substrates of the afferent (lymphatic drainage) and efferent limb (immune cell infiltration) of these distinct CNS compartments are under debate (Alves de Lima et al., 2020; Bartholomaeus et al., 2009; Goldmann et al., 2016; Iliff et al., 2012; Papadopoulos et al., 2020).

It is still unclear whether autoantigens can be exported from the CNS in a cell-bound manner (e.g. by DCs) in order to contribute to the initiation or maintenance of CNS autoimmunity. Over two million people worldwide had MS in 2016, resulting in a prevalence of 30.1 cases per 100 000 people world-wide. In North America and western Europe, the prevalence of MS are 164.6 and 127.0, respectively (Collaborators, 2019). Underlying risk factors of MS include genetic factors, like the HLA DRB1*1501 allele (DR15) (Sawcer et al., 2005), but also infections with Epstein-Barr virus (Serafini et al., 2007), vitamin D deficiency (Summerday et al., 2012), and smoking (O’Gorman et al., 2014), suggesting that alterations in life style might be, in part, responsible for the increasing incidence of MS. MS occurs more often in women and is diagnosed on average at 30 years of age (Reich et al., 2018). Its most common form is characterized by events of neurological relapses and subsequent remission, termed relapsing-

remitting MS (RRMS) and is often followed one or two decades after disease initiation by a progressive disease form, called secondary progressive MS (SPMS) (Tremlett et al., 2008). A minority of patients suffers from a progressive disease course from the start.

Many of the therapeutic approaches used in MS were first discovered in animal models that are able to replicate certain aspects of MS and play a pivotal role in studying the disease.

4.1.2 Experimental autoimmune encephalomyelitis

Experimental autoimmune encephalomyelitis (EAE) in C57BL/6 mice is the most common preclinical model for MS. It is induced by subcutaneous injection with CNS-specific antigens (e.g. myelin oligodendrocyte glycoprotein (MOG) peptide 35-55) in complete Freund's adjuvants (CFA) and pertussis toxin intravenously. Disease onset occurs between day 11 and 13 with the peak of disease typically being between day 15 and 20 and a recovery phase roughly after 30 days post immunization.

The EAE model provides an important tool to study the inflammatory cascade of CNS-infiltrating autoreactive CD4⁺ T cells. Importantly, the breach of tolerance of autoreactive CD4⁺ T cells to autoantigens has been studied extensively in EAE, as well as the infiltration into the CNS through the BBB, the re-activation in the CNS with successive immunopathology, and subsequent tissue repair (Petermann and Korn, 2011). Moreover, EAE is also an important tool to study T cell development during inflammation *in vivo* and has been pivotal in the discovery of Th17 cell biology (Hiltensperger and Korn, 2018; Korn et al., 2009; Petermann and Korn, 2011).

However, EAE as a model for MS also has its limitations. First and foremost, MOG(35-55)-induced EAE mainly reflects the CD4⁺ T cell-driven inflammatory aspects of MS and neglects B cell-dependent processes of CNS autoimmunity as well as more chronic compartmentalized inflammatory events in the CNS. Moreover, the potent adjuvants that are used to induce EAE cause certain biases in the differentiation of autoreactive T cells (e.g. strong Th17 responses) (Ronchi et al., 2016). Some of these biases can be averted in a spontaneous EAE model that is based on a double transgenic T cell receptor (TCR)^{MOG} (2D2) and B cell receptor (BCR)^{MOG} (TH) background (Bettelli et al., 2006). 2D2 x TH mice develop EAE spontaneously around 5 weeks of age without injection of antigen or adjuvants and in a B cell-dependent manner.

A series of therapies that are used in MS, like glatiramer acetate and natalizumab, were first tested and developed in EAE before they went into clinical trials (Robinson et al., 2014). While not all MS drugs were initially discovered in EAE, all current FDA-approved disease-modifying therapies for MS are effective in EAE to some degree, thus, underscoring its relevance for the development of new treatment options in MS (Robinson et al., 2014).

4.2 T helper cell subsets

T cells are classified based on surface markers, transcription factors, and their effector function upon antigen encounter. Cytotoxic CD8⁺ T cells recognize and kill infected cells, CD4⁺Foxp3⁻ T helper (Th) cells provide cytokines to other immune cells to shape the immune response, and CD4⁺Foxp3⁺ Treg cells suppress other immune cells and dampen immune responses. Th cells have been classified into distinct lineages based on their cytokine profile and master transcription factor expression into Th1 (interferon γ (IFN- γ); T-bet) and Th2 (interleukin 4 (IL-4); GATA3) (Liew, 2002), as well as the later discovered Th17 (interleukin 17 (IL-17); ROR- γ t) lineage (Hiltensperger and Korn, 2018; Korn et al., 2009; Petermann and Korn, 2011) (Figure 1).

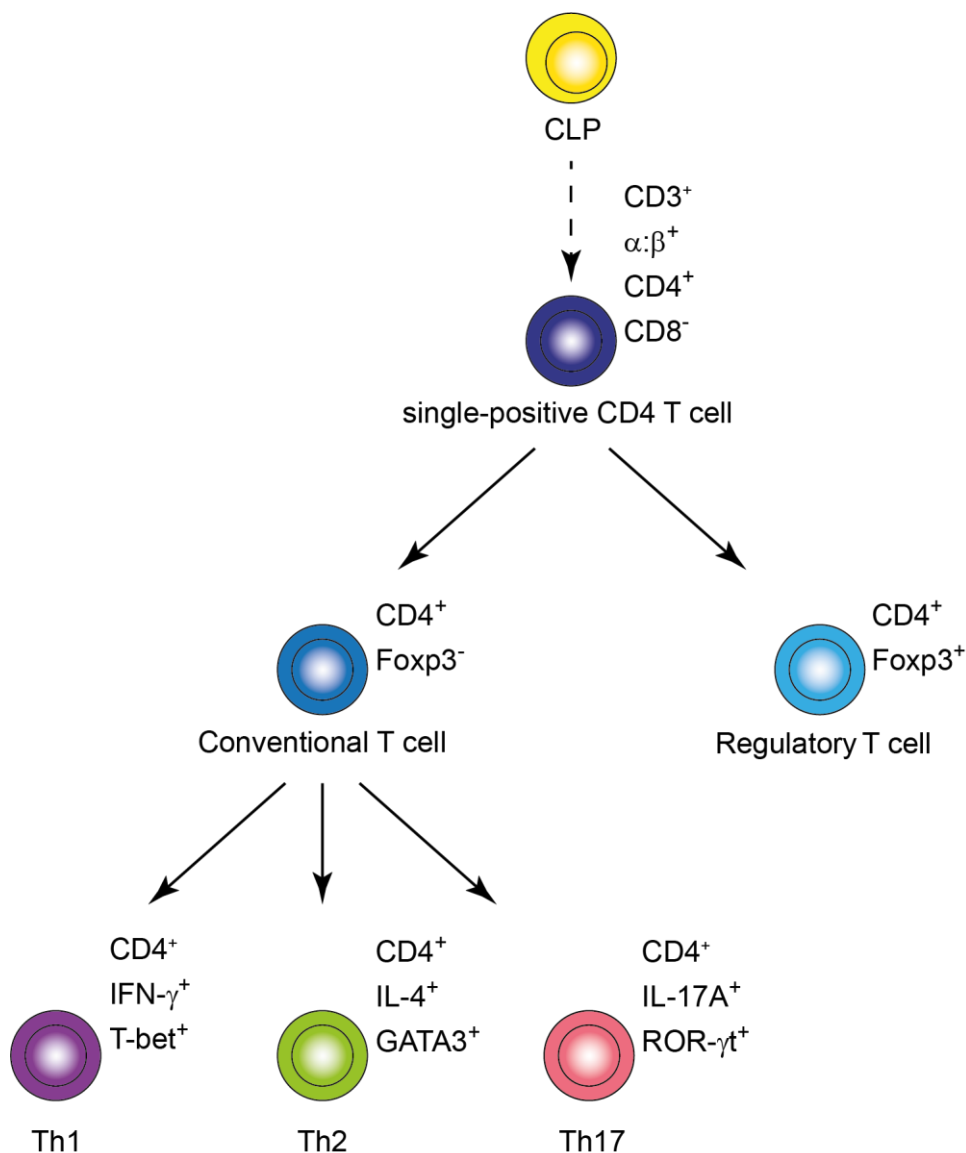


Figure 1: T helper cell and T regulatory cell differentiation.

Schematic overview of CD4⁺ T cell differentiation. Stages between the common lymphoid progenitor (CLP) and the single-positive CD4 T cell stage are omitted here. Single-positive CD4 T cells differentiate in the thymus into conventional or regulatory T cells based on the expression of the transcription factor Foxp3. Conventional T cells can be further differentiated into T helper (Th) cell subsets (Th1, Th2, and Th17) based on cytokine profile and transcription factor expression as indicated.

4.2.1 T cell development in the thymus

T cell precursors are generated in the bone marrow but their maturation takes place in the organ that gives them their name, the thymus (Donskoy and Goldschneider, 1992). Common lymphoid progenitors (CLPs) enter the thymus between the medulla and cortex and migrate outwards in the cortex where they populate the subcapsular zone (Lind et al., 2001). Those CD3⁻CD4⁻CD8⁻ “double-negative” (DN) thymocytes develop in the subcapsular zone into a minority of $\gamma\delta$ DN T cells (CD3⁺CD4⁻CD8⁻) and a majority of $\alpha\beta$ “double-positive” (DP) T cells (CD3⁺CD4⁺CD8⁺) (Lind et al., 2001). $\gamma\delta$ T cells already leave the thymus through efferent lymphatic vessels, while $\alpha\beta$ T cells undergo additional stages of development where they go from large to small and resting DP thymocytes (Shortman and Wu, 1996).

$\alpha\beta$ T cells go through two stages of selection, termed positive and negative selection. Small DP thymocytes interact in the cortex with cortical thymic epithelial cells (cTECs) that present self-antigens through major histocompatibility complexes (MHC) I and II. Thymocytes that do not bind to self-antigen/MHC complexes do not receive a survival signal and will die from programmed cell death, called apoptosis (Spits, 2002). The majority of DP thymocytes die during positive selection and the remaining cells migrate further to the border between thymic cortex and medulla where they develop either into “single-positive” (SP) CD4 or CD8 T cells (Zerrahn et al., 1997). The fate between CD4 and CD8 T cells is based on the interaction with MHC-I (CD8) or MHC-II (CD4) (Borgulya et al., 1991). Negative selection takes place in the medulla, where medullary thymic epithelial cells (mTECs) present self-antigens to SP T cells (Takaba and Takayanagi, 2017). In order to remove autoreactive T cells that could induce autoimmune responses, SP T cells that bind self-antigens with high affinity are eliminated by apoptosis (Takaba and Takayanagi, 2017). It is hypothesized that Treg cells are either generated by a subset of CD4⁺ T cells that starts expressing Foxp3 upon intermediate TCR self-reactivity (instructive model) or by TCR-independent signals at the DN stage that induce Foxp3 and render the cell resistant to negative selection upon high TCR self-reactivity (stochastic or selective model) (Hsieh et al., 2012; Klein et al., 2019). The elimination of autoreactive T cells and the development of Treg cells is an important control mechanism to prevent autoimmunity and is also known as central tolerance.

4.2.2 T cell priming

Naïve CD4⁺ T cells that have left the thymus circulate through the bloodstream and lymphatics in search for their cognate antigen. In the context of this search, naïve CD4⁺ T cells enter lymph nodes (LNs) through an interaction between L-selectin (CD62L) molecules on their surface and addressins that are present on high endothelial venules (HEVs) in the LNs (Bradley et al., 1994). LNs are part of the peripheral immune compartment and the place where blood and lymph comes into contact. Naïve CD4⁺ T cells remain in LNs for approximately 24 hours, a period of time that is increased to 3 to 4 days if the T cell encounters its cognate antigen

(Bouso, 2008). Antigen-presenting cells (APCs), e.g. DCs, as well as soluble antigens enter the LNs through afferent lymphatic vessels where they travel to the T cell zone and interact with naïve T cells (Liao and von der Weid, 2015). CD4⁺ T cells recognize their cognate antigen through binding of their TCR to a complex of MHC-II and a peptide that is presented on the surface of APCs.

In addition to TCR/MHC-II-peptide interaction with an APC, a naïve T cell must bind with its co-stimulatory receptors to the co-stimulatory molecules on the same APC in order to get activated (Bretscher, 1999). The best described co-stimulatory receptor that is present on all naïve T cells is CD28, and its ligands B7.1 (CD80) and B7.2 (CD86) are present on APCs (Acuto and Michel, 2003; Sharpe and Freeman, 2002). Moreover, the cytokine milieu during TCR/MHC-II-peptide interaction is essential for T cell activation and plays a major role in Th cell differentiation (Zhu and Paul, 2010). Th1 cells only fully differentiate in the presence of IL-12, while IL-4 is essential for the induction of Th2 cells, and IL-6 plays a major role in the differentiation of Th17 and T follicular helper (Tfh) cells (Agnello et al., 2003; Hiltensperger and Korn, 2018; Korn and Hiltensperger, 2021).

Priming of naïve T cells in LNs results in the upregulation of the early activation marker CD69 on the cell membrane within 2-3 hours (Cibrian and Sanchez-Madrid, 2017). CD69 is a marker for tissue retention and is also expressed on tissue-resident T cells, like resident memory T (TRM) cells and $\gamma\delta$ T cells (Cibrian and Sanchez-Madrid, 2017). In LNs, it has been shown that CD69 can form a complex with sphingosine-1-phosphate receptor-1 (S1P1) downstream of IFN- α/β to inhibit its functions and in turn the egress of lymphocytes from LNs (Shiow et al., 2006). Other activation markers include CD25, which is detected after upregulation of CD69, and the late activation marker CD44 that is commonly used as a marker to distinguish memory and effector T cells from naïve T cells (Baaten et al., 2010). In addition, the T cell LN homing marker CD62L is shed from the cell membrane upon T cell activation, which is used to distinguish central memory T cells (T_{cm}, CD62L^{high}CD44^{high}) from effector memory T cells (T_{em}, CD62L^{int}CD44^{high}) and is associated with T cell effector functions (Yang et al., 2011).

4.2.3 T cell plasticity

After commitment to a certain Th cell lineage, Th cells are not necessarily keeping their gene signature. Indeed, with the exception of natural Treg cells that were generated in the thymus, there are many reports that suggest that all Th subsets show a certain level of plasticity after initial differentiation.

While Th1 and Th2 cells are considered quite stable, Th17 cells are known for their extensive plasticity (Lee et al., 2009). Nonetheless, even Th1 and Th2 cells can switch their transcriptional profile if stimulated in alternative conditions (Murphy et al., 1996). This gives Th cells the ability and flexibility to respond and adjust to changes during inflammation.

Plasticity is dependent on the cytokine milieu that a T cell is exposed to. For example, IL-6 is not only essential for the differentiation of Th17 cells but is also considered important for their maintenance. IL-6 signaling is required to maintain the expression of the master transcription factor of Th17 cells, ROR- γ t, and to retain their Th17 cell transcriptome and identity (Harbour et al., 2020). On the other hand, the cytokine IL-23 (which is known to be a stabilizing factor for a pathogenic Th17 cell phenotype) as well as IL-12 promote the loss of ROR- γ t expression and induce the master transcription factor and signature cytokine of Th1 cells, T-bet and IFN- γ , in Th17 cells (Korn and Hiltensperger, 2021). This shows that factors that promote a pathogenic phenotype in Th17 cells, like IL-12 and IL-23, can still cause the loss of Th17 cell identity, however.

4.2.4 Impact of environmental cues on the T cell phenotype

Host-microbiota interactions are crucial for the development of the immune system and might be at least in part responsible for the reported increase in immune-mediated diseases in modern societies due to environmental and lifestyle changes. To avoid exacerbated immune responses against the microbiota, epithelial barriers are essential, and a large array of microbial signals promote gut barrier homeostasis and immune maturation through innate and adaptive immune signaling (Ruff et al., 2020).

Interactions with commensals and intestinal epithelial cells have been implicated in T cell development. For example, colonization of the small intestine with a single microbe, segmented filamentous bacterium (SFB), induces the production of serum amyloid A (SAA), which acts on lamina propria DCs to create a Th17 cell-inducing environment (Ivanov et al., 2009). In addition, microbiota-derived short-chain fatty acids (SCFAs) are inducing peripheral Treg cells in the intestine of mice and thereby create an anti-inflammatory environment (Arpaia et al., 2013; Smith et al., 2013). Loss of the integrity of intestinal epithelial barriers on the other hand can lead to inflammation and even autoimmunity. For example, the pathobiont *E. gallinarum* has been shown to induce autoimmune responses by translocating to the liver in genetically predisposed hosts (Manfredo Vieira et al., 2018). This in turn can cause the induction of Th17 and Tfh cells in secondary lymphoid organs through direct interactions with APCs or metabolites, like aryl hydrocarbon receptor (AhR) ligands, to promote autoimmunity (Ruff et al., 2020).

In addition, the skin microbiota is also implicated in T cell development and plays an important role in atopic diseases like asthma and atopic dermatitis (Kemter and Nagler, 2019). At birth, the skin is home to highly activated Treg cells that are essential to promote tolerance against skin commensals (Scharschmidt et al., 2015). Dysbiosis of skin microbes in neonates is associated with increased risk for allergic events later on in life as has been shown in newborns that were delivered by caesarian section compared to vaginal delivery (Black et al., 2015). The

lack of protective commensals like *S. epidermidis* can lead to the outgrowth of *S. aureus*, which in turn induces inflammation during atopic dermatitis in the form of epidermal thickening and Th2 and Th17 cell expansion in the skin (Byrd et al., 2017). Interestingly, commensals containing autoantigen orthologs of the lupus autoantigen Ro60 have been shown to activate Ro60 antigen-specific CD4 memory T cells isolated from lupus patients (Greiling et al., 2018). This could present a general mechanism how commensals could promote autoimmunity through T cell cross-reactivity in predisposed hosts.

Despite tremendous advances in our current understanding how environmental factors are shaping T cell biology and are therefore closely linked to health and disease, more mechanistic insights are needed to understand this complex interplay better and in particular how T cell responses to microbial antigens or metabolites impact T cell-mediated immunopathology in remote target tissues.

4.2.5 T cell trafficking to the CNS

In order for a T cell to infiltrate the CNS it has to pass the blood cerebrospinal fluid (CSF) barrier or the BBB, which separate the CNS compartment from the systemic compartment. Thus, guidance molecules on their cell membrane are required for T cells to enter the CNS, and the routes of entry are most likely dependent on the specific guidance molecules a T cell has (Figure 2).

One of the best known CNS homing markers for T cells is VLA-4, which is a heterodimeric $\alpha 4\beta 1$ -integrin complex. VLA-4 has been shown to be essential for the CNS infiltration of Th1 cells (likely through subarachnoid vessels as visualized in (2) of Figure 2), while Th17 cells are able to infiltrate in a VLA-4-independent manner that is dependent on the heterodimeric $\alpha L\beta 2$ -integrin complex (LFA-1) (Rothhammer et al., 2011; Schneider-Hohendorf et al., 2014). In addition, Treg cells – similar to Th17 cells – also have been reported to infiltrate the CNS in a LFA-1-dependent fashion in the absence of $\alpha 4$ -integrin (Glatigny et al., 2015). Another route of T cell entry into the brain parenchyma is through postcapillary venules via the perivascular space (as shown in (3) of Figure 2), which has been viewed previously as the most important route of entry for lymphocytes in the context of CNS autoimmunity (Hiltensperger and Korn, 2018).

Moreover, chemokine receptors are implicated in the CNS infiltration of T cells during EAE and MS. CCR6 is expressed in certain CD4⁺ T cells and its ligand, CCL20, is constitutively expressed in choroid plexus epithelial cells in mice and humans, suggesting that this route of entry is CCR6-dependent and favors Th17 cells that are known to express CCR6 (as visualized in (1) of Figure 2) (Reboldi et al., 2009). CCR5 and CXCR3 were found in T cells in active MS lesions and both were enriched in the CSF T cell population compared to circulating T cells (Sorensen et al., 1999).

Despite these advances, there are still many open questions about the connection of specific guidance molecules and their impact on the routes of T cell entry into the CNS, which could lead to the development of targeted therapies with less adverse drug effects. Therefore, further investigation of T cell trafficking to the CNS is vital for our understanding and development of new treatments in MS and other diseases that are connected to aberrant CNS T cell infiltration.

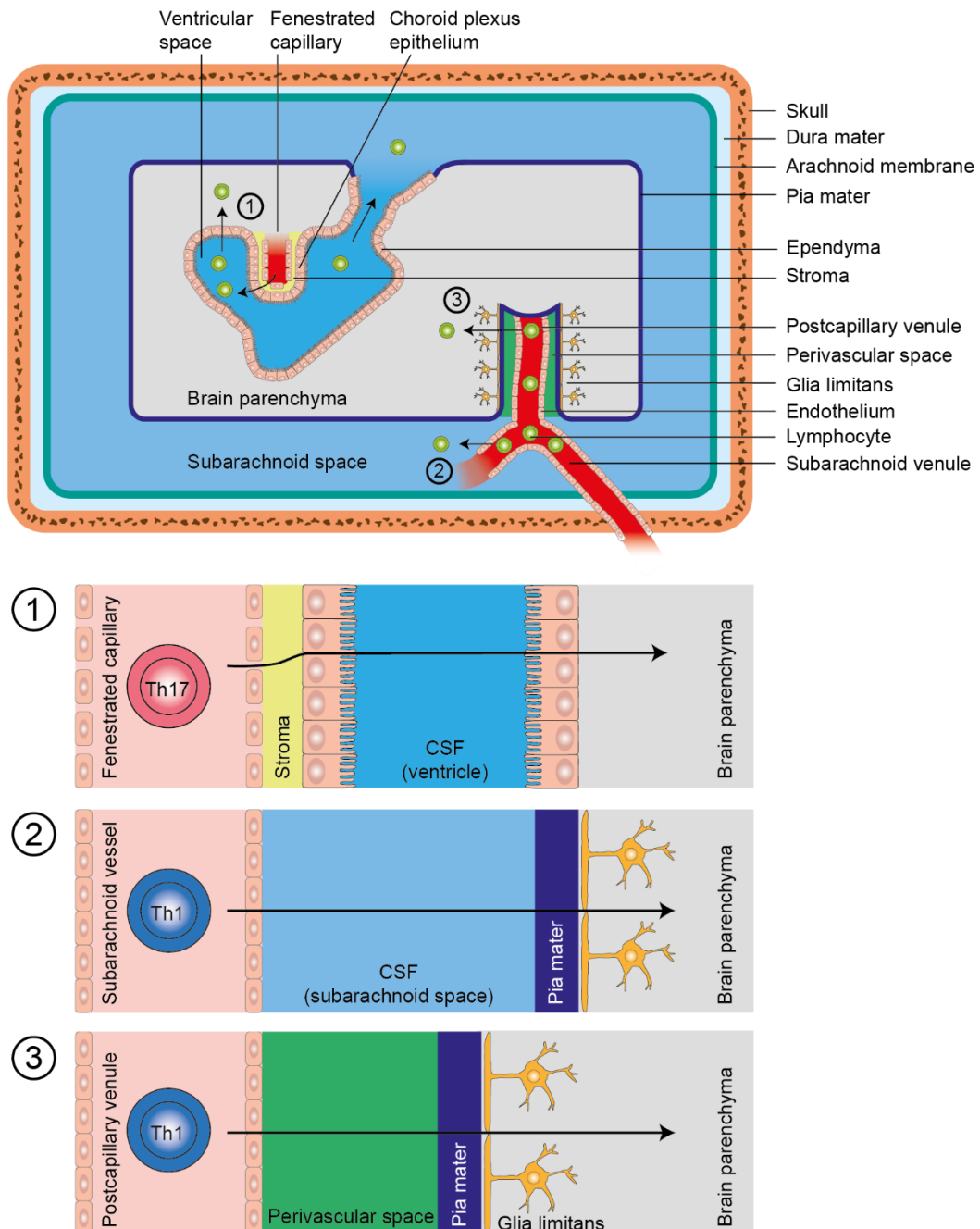


Figure 2: Potential routes of T cell entry into the CNS.

Schematic of T cell trafficking into the central nervous system (CNS). T cells need to pass blood cerebrospinal fluid (CSF) and blood brain barriers (BBB) in order to infiltrate into the CNS. Potential routes of T cell entry into the brain parenchyma are through the choroid plexus by crossing the choroid plexus epithelium (1), through subarachnoid vessels into the subarachnoid space and crossing of the glia limitans (2), and through postcapillary venules via the perivascular space (3). Original work, published in (Hiltensperger and Korn, 2018), copyright to Cold Spring Harbor (CSH) Laboratory Press. Permission for usage was kindly granted by CSH.

4.3 Spatiotemporal labeling of CD4⁺ T cells

Studies of T cell migration which used labeling approaches have been performed in the past solely in a temporal fashion. The time point of T cell labeling was controlled but not the location. The most commonly used inducible genetic system for this is the tamoxifen-inducible Cre-ER (Metzger et al., 1995), which utilizes an injection of tamoxifen to facilitate Cre activity in a time-specific manner. However, this approach has a clear limitation because it does not allow manipulation in a precise spatially controlled manner, as even injection into sequestered compartments is challenging due to leakiness of the injected tamoxifen.

The introduction of photoconvertible fluorescent proteins (PFPs) overcame this limitation by using a beam of light of a specific wavelength to photoconvert these PFPs at a defined irradiation site (Adam et al., 2014). A well established format are green-to-red PFPs, like Kaede and Dendra2 (Adam et al., 2011; Gurskaya et al., 2006). Not only are PFPs useful in microscopic studies of cellular processes *in vitro*, they can also be applied to study intercompartmental trafficking of cells *in vivo*. For this purpose, a laser is used to photoconvert cells at specific body sites, allowing for spatiotemporal labeling of these cells.

Spatiotemporal labeling can serve as a provenance reporter (site of labeling) of photoconverted cells. Characterizing photoconverted cells found anywhere in the body via flow cytometry or immunohistochemistry constitutes a powerful tool to study T cell migration and effector functions of T cells in distal tissues based on their site of origin, as will be addressed in this thesis.

4.3.1 Photoconvertible fluorescent proteins (PFPs)

A breakthrough discovery for the application of photoactivatable proteins was the report of a photoactivatable variant of the green fluorescent protein (GFP) from the jellyfish *Aequorea victoria*, termed PA-GFP (Patterson and Lippincott-Schwartz, 2002). PA-GFP can be photoactivated by irradiation with light of 413 nm wavelength to increase its green fluorescence by 100 times upon excitation with 488 nm light and can be used to study intracellular protein dynamics (Patterson and Lippincott-Schwartz, 2002). Another important tool for cell labeling is the green-to-red PFP Kaede that was discovered in the stony coral *Trachyphyllia geoffroyi* (Ando et al., 2002). Irradiation with ultraviolet or violet light effectively switches the fluorescence of Kaede from green to red, while having excellent photostability and brightness of the red fluorescent state (Ando et al., 2002).

After that, a multitude of proteins were developed with different fluorescent properties. One of them is an engineered monomeric green-to-red PFP that is based on the green fluorescent protein dendGFP from octocoral *Dendronephthya sp.*, termed Dendra (from *Dendronephthya sp.* red activatable) (Gurskaya et al., 2006). Dendra has a range of advantageous properties

for a PFP, including its monomeric state, high contrast between green and red fluorescent state, photoconversion with 405 nm or 490 nm light, efficient maturation at 37°C in bacterial and mammalian cells, and high photostability of the red fluorescent state (Gurskaya et al., 2006). These characteristics make Dendra a powerful tool for protein and cell labeling applications.

Moreover, a single amino acid substitution in Dendra at position 224 from alanine to valine results in an improved version, termed Dendra2, with accelerated maturation at 37°C and brighter fluorescence of both the green and red fluorescent state (Chudakov et al., 2007). Dendra2 exists in equilibrium in a neutral/nonfluorescent and an anionic/green fluorescent state. While irradiation with 405 nm light efficiently photoconverts the nonfluorescent state into the red state, irradiation with 490 nm light photoconverts the green fluorescent state less efficiently into the red state (Figure 3). These characteristics make Dendra2 an excellent tool to study immune cell trafficking *in vivo*.

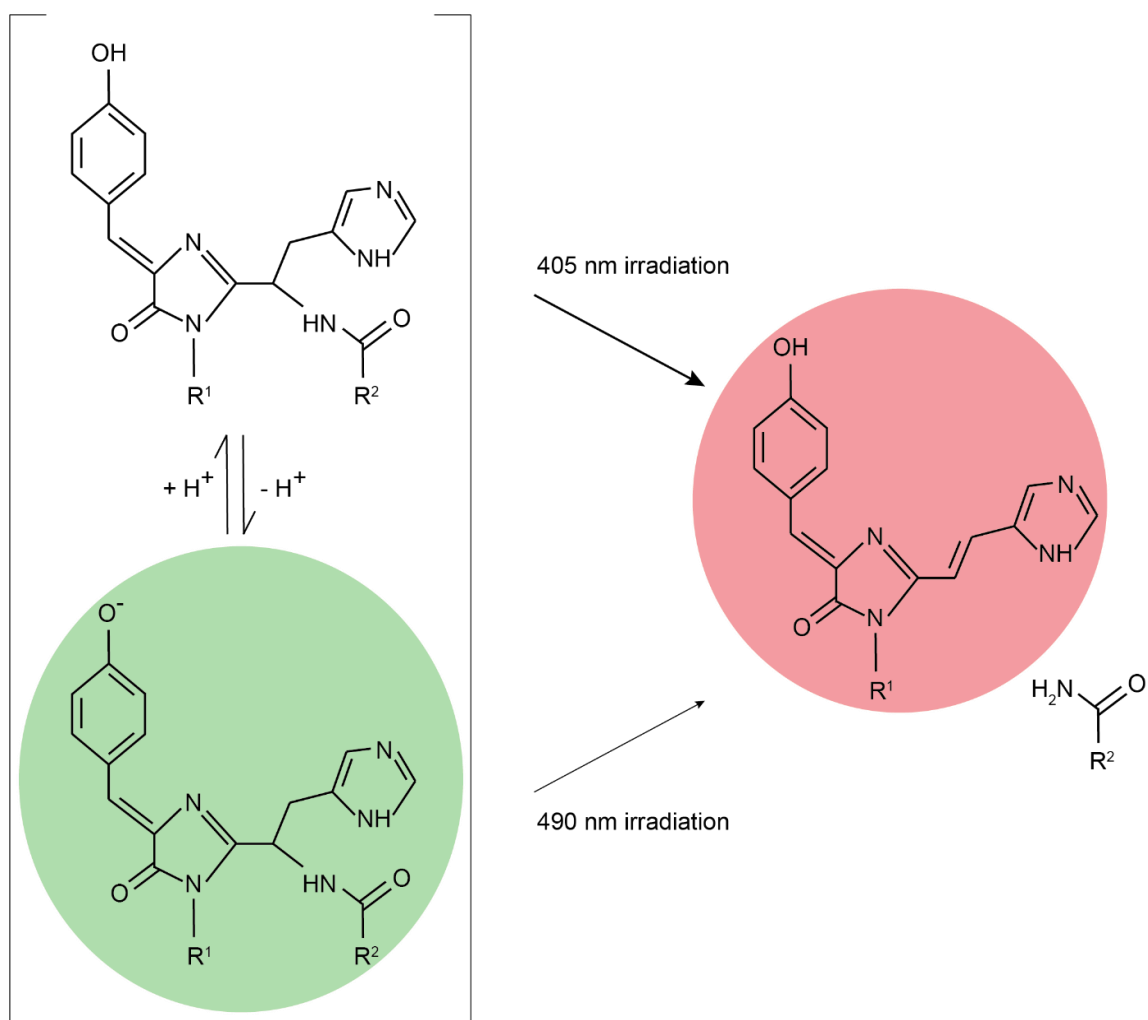


Figure 3: Photoconversion dynamics of Dendra2.

Neutral/nonfluorescent and anionic/green fluorescent state (highlighted in green) of Dendra2 exists in equilibrium (visualized by brackets). Photoconversion of the nonfluorescent state occurs by irradiation with 405 nm light or of the green fluorescent state by 490 nm light irradiation. The red fluorescent state (highlighted in red) is characterized by the carbon double bond and the cleavage of the protein backbone. Adapted from (Chudakov et al., 2007).

4.3.2 Photoactivatable mitochondria mouse line

To study immune cell trafficking in the context of EAE over a few days, the photoactivatable mitochondria (PhAM)^{floxed} transgenic mouse line (Pham et al., 2012) was used in this thesis. These mice express the PFP Dendra2 tagged to the mitochondrial targeting sequence of subunit VIII of cytochrome c oxidase in mitochondria (mito-Dendra2; mD2) of Cre-expressing cells (Pham et al., 2012). Tagging of Dendra2 to the mitochondria results in a higher half-life compared to cytosolic localization. Moreover, Dendra2 requires less energy for photoactivation at a wavelength of 405 nm compared to Kaede (Kremers et al., 2009), which is another commonly used green-to-red PFP.

In order to generate a system that can be used to label and track the migration of CD4⁺ T cells, the PhAM^{floxed} strain was crossed with a CD4-Cre driver strain to generate PhAM^T mice. Note that not only CD4⁺ cells express mD2 in PhAM^T mice but also CD8⁺ since T cells are DP for CD4 and CD8 at one stage during their maturation in the thymus. Irradiation with violet light (405 nm) irreversibly photoconverts the mD2 molecules in the cell from mD2^{GREEN} to mD2^{RED}. However, mD2^{RED} molecules are evenly distributed with their mitochondria during cell division, resulting in a reduction of mD2^{RED} mean fluorescent intensity in proliferating cells.

4.4 Aim of the study

In MS, autoreactive T cells are activated in the systemic immune compartment before migrating to the CNS. Deciphering how sensing of molecular cues at the gut and skin epithelium is shaping autoreactive T cell responses that then translate into distinct immunopathological patterns in the CNS could deepen our understanding of the initiation and progression of MS. Moreover, my study could help to assess efficient therapeutic interventions that target the infiltration of pathogenic T cells into the CNS but do not jeopardize immune surveillance of the CNS at the same time. Therefore, I addressed the role of the site of T cell priming (gut- or skin-draining LNs) for potential routes of entry into the CNS and their effector functions *in situ* in this thesis.

The first aim of the study was to examine potential routes of CD4⁺ T cell infiltration into the CNS that are activated in gut- or skin-draining LNs in a setting of CNS autoimmunity. In most experiments the inducible model of EAE was used to trigger CNS autoimmunity by immunization with MOG(35-55) peptide in C57BL/6 mice. I used the PhAM^T mouse line to photoconvert either T cells in the inguinal lymph node (iLN; through the skin) or in the mesenteric lymph node (mLN; surgically exposed) (see schematic in Figure 5a). Photoconverted T cells were then tracked (based on their fluorescent reporter signal mD2^{RED}) from their priming LN to the spleen and to their target organ, the CNS.

The second aim was to elucidate if the activation of CD4⁺ T cells in gut- or skin-draining LNs imprinted different gene signatures and, importantly, whether skin-imprinted (i-T cells) versus gut-imprinted T cells (m-T cells) exhibited distinct phenotypes in the CNS. To address this question, single cell RNA sequencing (scRNA-seq) of i-T cells (photoconverted in the iLN) and m-T cells (photoconverted in the mLN) was performed. Identified targets from the scRNA-seq were followed up with additional experiments to probe them for their functional relevance in the context of CNS autoimmunity.

The majority of the presented data in this thesis was published in (Hiltensperger et al., 2021) and permission for usage was kindly granted by Springer Nature.

5 Material and methods

5.1 Materials

5.1.1 Instruments

Name of instrument	Manufacturer
Agarose gel electrophoresis systems	Bio-Rad (Hercules, USA)
Bioanalyzer 2100	Agilent Technologies (Santa Clara, USA)
Cell harvester-MicroBeta FilterMate-96	PerkinElmer (Waltham, USA)
Cell sorter, FACSAria III	BD Biosciences (Heidelberg, Germany)
Centrifuge 5424	Eppendorf (Hamburg, Germany)
Combined refrigerator-freezer	Bosch (Gerlingen, Germany)
Counting chamber, Neubauer-improved	Sigma-Aldrich (St. Louis, USA)
CytoFLEX	Beckman Coulter (Brea, USA)
Eclipse Ti2 microscope	Nikon (Tokyo, Japan)
Fridge (+4 °C)	Siemens (Munich, Germany)
Gel documentation-Felix 1010	Biotec-Fischer (Reiskirchen, Germany)
HERA Cell 240i CO ₂ Incubator	Thermo Fisher (Schwerte, Germany)
HiSeq 1500	Illumina (San Diego, USA)
HiSeq 2500	Illumina (San Diego, USA)
Laminar flow cabinet	Kojair Tech Oy (Vilppula, Finland)
LuxX 405-60 laser	Soliton (Gilching, Germany)
Microscope-VistaVision	VWR (Radnor, USA)
Microwave-R-2V14	Sharp (Munich, Germany)
Mini centrifuge-Spectrafuge	Labnet international (Edison, USA)
Nanodrop-NP-1000	PEQLAB (Erlangen, Germany)
NextSeq 500	Illumina (San Diego, USA)
Pipet Controllers -Accu-jet pro	Sigma-Aldrich (St. Louis, USA)
Pipettes (P2.5, P10, P200, P1000)	Eppendorf (Hamburg, Germany)
Real-Time PCR Systems-StepOne	Life Technologies (Carlsbad, USA)
Scintillation counter-MicroBeta TriLux	PerkinElmer (Waltham, USA)
SP8 confocal microscope	Leica Microsystems (Wetzlar, Germany)
Thermal cycler-2720	Life Technologies (Carlsbad, USA)
Thermomixer-comfort	Eppendorf (Hamburg, Germany)
Vortex mixer	VWR (Radnor, USA)
Waterbath	Memmert (Schwabach, Germany)

5.1.2 Consumables

Name of consumable	Manufacturer
Cell culture plates (96-, 24-well flat bottom, 96-well round bottom)	Megro (Wesel, Germany)
Cell strainer (30 μm)	Sysmex (Kobe, Japan)
Cell strainer (70 μm and 100 μm)	BD Biosciences (Heidelberg, Germany)
Conical centrifuge tubes (15 ml and 50 ml)	Greiner Bio-One (Frickenhausen, Germany)
Filtermat A, printed (for cell harvester)	PerkinElmer (Waltham, USA)
Pipette tips	Eppendorf (Hamburg, Germany)
Reaction tubes, 0.2, 0.5, 1.5, and 2.0 ml	Sarstedt (Nümbrecht, Germany)
Real-Time PCR reaction plates	Thermo Fisher (Schwerte, Germany)
Syringes and needles of different sizes	B. Braun (Melsungen, Germany)

5.1.3 Chemicals and reagents

Name of chemical or reagent	Manufacturer
β -Mercaptoethanol	Merck (Darmstadt, Germany)
100 bp DNA Ladder	Thermo Fisher (Schwerte, Germany)
Agarose	Sigma-Aldrich (St. Louis, USA)
Agencourt AMPure XP beads	Beckman Coulter (Brea, USA)
Aqua dest.	B. Braun (Melsungen, Germany)
BD Pharm Lyse	BD Bioscience (Heidelberg, Germany)
Collagenase D	Roche Diagnostics (Penzberg, Germany)
Digitonin	Promega (Madison, USA)
DMEM	Thermo Fisher (Schwerte, Germany)
DNase I	Roche Diagnostics (Penzberg, Germany)
Dulbecco's PBS (10x)	Thermo Fisher (Schwerte, Germany)
Dulbecco's PBS (1x)	Thermo Fisher (Schwerte, Germany)
EDTA	Merck (Darmstadt, Germany)
EDTA.Na ₂ *2H ₂ O	Merck (Darmstadt, Germany)
FCS	Sigma-Aldrich (St. Louis, USA)
Fetal calf serum	Sigma-Aldrich (St. Louis, USA)
FluoroMyelin Red	Invitrogen (Waltham, USA)
Folic acid	Sigma-Aldrich (St. Louis, USA)
FTY720 (Fingolimod)	Novartis (Basel, Switzerland)
Gentamycin	Life Technologies (Carlsbad, USA)

Name of chemical or reagent	Manufacturer
Glacial acetic acid	Sigma-Aldrich (St. Louis, USA)
HCl	Merck (Darmstadt, Germany)
Isoflurane	Albrecht GmbH (Aulendorf, Germany)
KHCO ₃	Merck (Darmstadt, Germany)
L-Arginine	Sigma-Aldrich (St. Louis, USA)
L-Asparagine	Sigma-Aldrich (St. Louis, USA)
L-Glutamine	Sigma-Aldrich (St. Louis, USA)
Mannide Monooleate	GERBU (Heidelberg, Germany)
MEM non-essential amino acids sol. (100X)	Thermo Fisher (Schwerte, Germany)
MEM vitamin solution (100X)	Thermo Fisher (Schwerte, Germany)
MgCl ₂	Merck (Darmstadt, Germany)
MOG(35-55) peptide	Auspep (Tullamarine, Australia)
Mycobacterium tuberculosis H37Ra	BD Biosciences (Heidelberg, Germany)
NaCl	Merck (Darmstadt, Germany)
NaOH	Merck (Darmstadt, Germany)
NH ₄ Cl	Merck (Darmstadt, Germany)
OVA(323-339) peptide	peptides & elephants (Hennigsdorf, Ger.)
Paraffin oil	Sigma-Aldrich (St. Louis, USA)
Penicillin/Streptomycin	Sigma-Aldrich (St. Louis, USA)
Percoll	GE Healthcare (Solingen, Germany)
Pertussis toxin	Sigma-Aldrich (St. Louis, USA)
PFA	Sigma-Aldrich (St. Louis, USA)
ProLong Gold antifade mount media	Life Technologies (Carlsbad, USA)
RPMI 1640	Thermo Fisher (Schwerte, Germany)
Sodium pyruvate	Sigma-Aldrich (St. Louis, USA)
Tagment DNA Buffer (2x)	Illumina (San Diego, USA)
TCL Buffer	Qiagen (Hilden, Germany)
Thymidine [Methyl-3H]	PerkinElmer (Waltham, USA)
Tn5 transposase	Illumina (San Diego, USA)
Tris Base	Sigma-Aldrich (St. Louis, USA)
Tris-HCl	Merck (Darmstadt, Germany)
Trizma Base	Calbiochem (Darmstadt, Germany)
Tween-20	Sigma-Aldrich (St. Louis, USA)

5.1.4 Buffers and solutions

Name of buffer	Composition
ACK lysing buffer	Distilled water supplemented with: 8,024 mg/l NH ₄ Cl 1,001 mg/l KHCO ₃ 3.722 mg/l EDTA.Na ₂ *2H ₂ O
ATAC Lysis Plus Transposition mixture	5 µl Tagment DNA Buffer (2x) 0.5 µl Tn5 transposase 0.95 µl water 3.3 µl PBS 0.05 µl 2 % digitonin 0.1 µl 10% Tween-20 0.1 µl 10% NP-40
ATAC Resuspension buffer	Distilled water supplemented with: 3 mM MgCl ₂ 10 mM NaCl 10 mM Tris-HCl pH 7.4
Clone medium	DMEM supplemented with: 10 % (v/v) heat-inactivated FCS 1 % (v/v) Pen-Strep non-essential amino acids (final conc. 1x) vitamins solution (final conc. 1x) 0.66 mM L-Arginine 0.27 mM L-Asparagine 13.6 mM Folic acid 0.2 mM β-Mercaptoethanol 0.1 mg/ml Gentamycin
CNS digestion medium	RPMI1640 supplemented with: 10 % (v/v) heat-inactivated FCS 1 mg/ml collagenase D 40 µg/ml DNase I

Name of buffer	Composition
Complete DMEM	DMEM supplemented with: 10 % (v/v) heat-inactivated FCS 1 % (v/v) Pen-Strep non-essential amino acids (final conc. 1x) 36 mg/l L-Asparagine 2 mM L-Glutamine 4 µl/l β-Mercaptoethanol 1 mM sodium pyruvate
Complete Freund's adjuvant	17 ml paraffin oil 3 ml Mannide Monooleate 100 µg Mycobacterium tuberculosis
FACS buffer	PBS supplemented with: 2 % (v/v) heat-inactivated FCS
MACS buffer	PBS supplemented with: 0.5 % (w/v) BSA 2 mM EDTA (pH 8)
Neutralization buffer	Aqua dest. supplemented with: 40 mM Trizma Base
Paraformaldehyde (PFA) (4 %)	PBS supplemented with: 4 % (w/v) PFA
PBS Tween	PBS supplemented with: 0.05% (v/v) Tween-20
Percoll 37 %	Percoll mix solution supplemented with: 37 % (v/v) Percoll
Percoll 70 %	Percoll mix solution supplemented with: 70 % (v/v) Percoll
Percoll mix solution	90 ml PBS (10x) 264 ml Aqua dest. pH adjusted to 7.2 with HCl
RPMI medium (10 %)	RPMI1640 supplemented with: 10 % (v/v) heat-inactivated FCS
TAE buffer (50x)	Aqua dest. supplemented with: 242 g/l Tris 57.1 ml/l Glacial acetic acid 0.5 mM EDTA (pH 8)

Name of buffer	Composition
Tail lysis buffer	Aqua dest. supplemented with: 25 mM NaOH 2 mM EDTA
Tail neutralization buffer	Aqua dest. supplemented with: 40 mM Trizma Base
Tris elution buffer	Aqua dest. supplemented with: 10 mM Tris pH 8.0

5.1.5 Kits

Name of kit	Manufacturer
Chromium Next GEM Chip G Single Cell Kit	10x Genomics (Pleasanton, USA)
Chromium Single Cell 3' Library & Gel Bead Kit	10x Genomics (Pleasanton, USA)
Chromium Single Cell 5' Feature Barcode Library Kit	10x Genomics (Pleasanton, USA)
Chromium Single Cell 5' Library & Gel Bead Kit	10x Genomics (Pleasanton, USA)
DYNAL Dynabeads Maus Pan B (B220) Kit	Thermo Fisher (Schwerte, Germany)
Foxp3 Staining Kit	eBioscience (San Diego, USA)
LIVE/DEAD fixable Near-IR stain Kit	Invitrogen (Waltham, USA)
PCR Clean-up MinElute Kit	Qiagen (Hilden, Germany)
Qubit dsDNA hs Kit	Life Technologies (Carlsbad, USA)
RNeasy Plus Micro Kit	Qiagen (Hilden, Germany)
Ultra II FS Kit	NEB (Ipswich, USA)

5.1.6 Antibodies

Specificity	Clone	Conjugate	Manufacturer
CD3e (anti-mouse)	500A2	-	eBioscience (San Diego, USA)
CD3e (anti-mouse)	145-2C11	APC	BD Bioscience (Heidelberg)
CD4 (anti-mouse)	EPR19514	-	Abcam (Cambridge, USA)
CD4 (anti-mouse)	RM4-5	PerCP-eF710	eBioscience (San Diego, USA)
CD4 (anti-mouse)	RM4-5	APC	BD Bioscience (Heidelberg)
CD4 (anti-mouse)	RM4-5	BV786	BD Bioscience (Heidelberg)

Specificity	Clone	Conjugate	Manufacturer
CD4 (anti-mouse)	RM4-5	Pacific Blue	BD Bioscience (Heidelberg)
CD8 α (anti-mouse)	53-6.7	APC-Cy7	Biolegend (San Diego, USA)
CD28 (anti-mouse)	37.51	-	eBioscience (San Diego, USA)
CD29 (anti-mouse)	HM β 1-1	BV786	BD Bioscience (Heidelberg)
CD44 (anti-mouse)	IM7	APC-R700	BD Bioscience (Heidelberg)
CD44 (anti-mouse)	IM7	BV421	BD Bioscience (Heidelberg)
CD49d (anti-mouse)	R1-2	APC	Biolegend (San Diego, USA)
CD62L (anti-mouse)	MEL-14	APC	BD Bioscience (Heidelberg)
CD62L (anti-mouse)	MEL-14	BV786	Biolegend (San Diego, USA)
CD186 (anti-mouse)	SA051D1	AF647	Biolegend (San Diego, USA)
CD186 (anti-mouse)	SA051D1	BV421	Biolegend (San Diego, USA)
CD16/CD32 (anti-mouse)	2.4G2	-	BD Bioscience (Heidelberg)
IgG H&L (anti-rabbit)	Polyclonal	AF647	Abcam (Cambridge, USA)
TCR γ/σ (anti-mouse)	GL3	BV421	Biolegend (San Diego, USA)
P2RX7 (anti-mouse)	1F11	APC	Biolegend (San Diego, USA)
Foxp3 (anti-mouse)	FKJ-16s	eF450	eBioscience (San Diego, USA)
TotalSeq-A0301 (anti-mouse)	M1/42; 39-F11	DNA barcode	Biolegend (San Diego, USA)
TotalSeq-A0302 (anti-mouse)	M1/42; 39-F11	DNA barcode	Biolegend (San Diego, USA)
TotalSeq-A0303 (anti-mouse)	M1/42; 39-F11	DNA barcode	Biolegend (San Diego, USA)
TotalSeq-A0304 (anti-mouse)	M1/42; 39-F11	DNA barcode	Biolegend (San Diego, USA)
TotalSeq-A0305 (anti-mouse)	M1/42; 39-F11	DNA barcode	Biolegend (San Diego, USA)
TotalSeq-A0306 (anti-mouse)	M1/42; 39-F11	DNA barcode	Biolegend (San Diego, USA)
TotalSeq-A0307 (anti-mouse)	M1/42; 39-F11	DNA barcode	Biolegend (San Diego, USA)
TotalSeq-A0308 (anti-mouse)	M1/42; 39-F11	DNA barcode	Biolegend (San Diego, USA)
TotalSeq-A0309 (anti-mouse)	M1/42; 39-F11	DNA barcode	Biolegend (San Diego, USA)

Specificity	Clone	Conjugate	Manufacturer
TotalSeq-A0310 (anti-mouse)	M1/42; 39-F11	DNA barcode	Biolegend (San Diego, USA)
TotalSeq-A0311 (anti-mouse)	M1/42; 39-F11	DNA barcode	Biolegend (San Diego, USA)
TotalSeq-A0312 (anti-mouse)	M1/42; 39-F11	DNA barcode	Biolegend (San Diego, USA)
TotalSeq-C0301 (anti-mouse)	M1/42; 39-F11	DNA barcode	Biolegend (San Diego, USA)
TotalSeq-C0302 (anti-mouse)	M1/42; 39-F11	DNA barcode	Biolegend (San Diego, USA)
TotalSeq-C0303 (anti-mouse)	M1/42; 39-F11	DNA barcode	Biolegend (San Diego, USA)
TotalSeq-C0304 (anti-mouse)	M1/42; 39-F11	DNA barcode	Biolegend (San Diego, USA)
TotalSeq-C0305 (anti-mouse)	M1/42; 39-F11	DNA barcode	Biolegend (San Diego, USA)
TotalSeq-C0306 (anti-mouse)	M1/42; 39-F11	DNA barcode	Biolegend (San Diego, USA)
TotalSeq-C0307 (anti-mouse)	M1/42; 39-F11	DNA barcode	Biolegend (San Diego, USA)
TotalSeq-C0308 (anti-mouse)	M1/42; 39-F11	DNA barcode	Biolegend (San Diego, USA)
TotalSeq-C0309 (anti-mouse)	M1/42; 39-F11	DNA barcode	Biolegend (San Diego, USA)

5.1.7 Oligonucleotides

Oligonucleotides for PCR-based mouse genotyping were ordered from Eurofins Genomics Germany GmbH (Ebersberg, Germany).

ID	Name of oligonucleotide	Sequence (5' to 3')	Product (bp)
1	MitoDendra2 Common fwd	CCAAAGTCGCTCTGAGTTGTTATC	
2	MitoDendra2 Mutant rev	TCAATGGGCGGGGGTCGTT	376 (ID1+2)
3	MitoDendra2 Wild Type rev	GAGCGGGAGAAATGGATATG	604 (ID1+3)
4	CD4-Cre Transgene fwd	GTCATGCACTGCTGCTATTGC	500 (ID4+5)

ID	Name of oligonucleotide	Sequence (5' to 3')	Product (bp)
5	CD4-Cre Transgene rev	GCGAACATCTTCAGGTTCTG	
6	IL17A-Cre Common fwd	CAAGTGCACCCAGCACCAGCTGATC	
7	IL17A-Cre Mutant rev	AGTCCCTCACATCCTCAGGTT	300 (ID6+7)
8	IL17A-Cre Wild Type rev	CTTAGTGGGTTAGTTTCATCACAGC	304 (ID6+8)
9	2D2 Transgene fwd	CCCGGGCAAGGCTCAGCCATGCTCCTG	675
10	2D2 Transgene rev	GCGGCCGCAATTCCCAGAGACATCCCTCC	(ID9+10)
11	TH Knock in fwd	GCCTCAGTGGAGATATCCTGCAAG	305
12	TH Knock in rev	GGAGACTGTGAGAGTGGTGCCT	(ID11+12)
13	IgH Wild type fwd	TCTCTTCTATGCTTTCTTTGTCCC	500
14	IgH Wild type rev	GTCATTGTTCCACATTCTGTTCC	(ID13+14)
15	TCRD Internal Standard fwd	CAAATGTTGCTTGTCTGGTG	200
16	TCRD Internal Standard rev	GTCAGTCGAGTGCACAGTTT	(ID15+16)
17	IL2R Internal Standard fwd	CTAGGCCACAGAATTGAAAGATCT	324
18	IL2R Internal Standard rev	GTAGGTGGAAATTCTAGCATCATCC	(ID17+18)

5.1.8 Software

Name of software	Manufacturer
Bowtie (v.1.1.2)	Open source
Cell Ranger (v.3.1.0)	10x Genomics (Pleasanton, USA)
CITE-seq-Count (Python package) (v.1.4.3)	Open source
CytExpert (v.2.3.1.22)	Beckman Coulter (Krefeld, Germany)
Endnote (v.X9.3.3)	Thomson Reuters (New York, USA)
FACS Diva (v.8.0.1)	BD Biosciences (Heidelberg, Germany)
Flowjo (v.10.5.1)	Tree Star (Ashland, USA)
GSEA (v.4.0.3)	Broad Institute (Cambridge, USA)
HOMER (v.4.9)	Open source

Name of software	Manufacturer
Illustrator 2020 (v.24.3)	Adobe Systems Inc. (San Jose, USA)
ImageJ (v.1.49k)	NIH (Bethesda, USA)
Leica Applications Suite X (v.3.5.6.21594)	Leica Microsystems (Wetzlar, Germany)
Leica LCS (v.2.6.1.5173)	Leica Microsystems (Wetzlar, Germany)
NIS Elements AR (v.5.20.00)	Nikon (Tokyo, Japan)
Office 2016	Microsoft (Redmond, USA)
Photoshop CS6 (v.13.0)	Adobe Systems Inc. (San Jose, USA)
Prism (v.7.05)	GraphPad Software (San Diego, USA)
Python (v.3.6)	Python Software Foundation (Beaverton, USA)
R (v.3.6.1)	R Core Team (Vienna, Austria)
Seurat (R package) (v.3.1.0)	Satija Lab and Collaborators (New York, USA)

5.2 Methods

5.2.1 Animals and animal-related procedures

5.2.1.1 Animals

The following mice were obtained from The Jackson Laboratory: C57BL/6J wild-type (WT) mice (stock number 000664), PhAM^{flox^{ed}} reporter mice (stock number 018385) (Pham et al., 2012), CD4-Cre mice (stock number 022071) (Lee et al., 2001), IL-17A-Cre mice (stock number 016879) (Hirota et al., 2011), TCR^{MOG} mice (also known as 2D2 mice; stock number 006912) (Bettelli et al., 2003), and *Rag1*^{-/-} mice (stock number 002216) (Mombaerts et al., 1992). *Cxcr6*^{gfp/gfp} mice (The Jackson Laboratory stock number 005693) (Unutmaz et al., 2000) were kindly provided by P. Knolle (Klinikum rechts der Isar, Technical University of Munich, Germany) and BCR^{MOG} mice (also known as TH mice) (Litzenburger et al., 1998) were kindly provided by H. Wekerle (May-Planck-Institut für Neurobiologie, Martinsried, Germany).

PhAM^T mice were generated by crossing of the PhAM^{flox^{ed}} line with the CD4-Cre line to create mice that express Dendra2 in the mitochondria (mitoDendra2, mD2) of cells that expressed CD4. PhAM^{IL-17} mice were generated by crossing of the PhAM^{flox^{ed}} line with the IL17A-Cre line to create mice that express mD2 in cells that expressed IL-17A. 2D2 x TH PhAM^T mice were generated by crossing of the PhAM^T line with 2D2 mice and TH mice, to give rise to a mouse line that develops spontaneous EAE (Bettelli et al., 2006; Krishnamoorthy et al., 2006).

All mouse strains were on C57BL/6J background and were kept in a specific pathogen-free facility with a dark/light cycle of 12 hours, a temperature of 20 to 24°C, and a humidity of 45 to 60% at the Technical University of Munich or at the Ludwig Maximilian University of Munich. All experimental protocols were approved by the standing committee for experimentation with laboratory animals of the Bavarian state authorities and were carried out in accordance with the corresponding guidelines (TVA AZ: ROB-55.2-2532.Vet_02-13-29, ROB-55.2-2532.Vet_02-17-69, ROB-55.2-2532.Vet_02-17-234, ROB-55.2-2532.Vet_02-14-95, ROB-55.2-2532.Vet_03-18-53). 8 to 14-week-old age and sex-matched mice were used for all experiments, except for spontaneous EAE experiments, where 5 to 8-week-old mice were used.

5.2.1.2 Earmarking and tail biopsy collection

Mice were anaesthetized with Isoflurane and the tip of the tail (approximately 1-2 mm) was removed with a scalpel and stored at -20°C until DNA extraction. Ear notches were punched with an ear punch device in order to identify each mouse.

5.2.1.3 FTY720 treatment

Mice were treated with 2 µg ml⁻¹ FTY720 (Fingolimod) orally over the drinking water ad libitum. In experiments with naive animals, treatment was started 5 days before lymph node (LN) irradiation and in experiments with EAE animals, treatment started 1 day before LN irradiation. Treatment was continued until the end of the experiment. To make sure that EAE animals received sufficient levels of FTY720, mice received one injection of 1 µg FTY720 per gram bodyweight i.p. at the start of treatment.

5.2.1.4 EAE induction

Induction of EAE in mice was achieved by subcutaneous immunization with 200 µg of myelin oligodendrocyte glycoprotein (MOG) peptide 35-55 (MEVGWYRSPFSRVVHLYRNGK) in complete Freund's adjuvant (CFA), containing 500 µg *Mycobacterium tuberculosis* H37Ra (BD Biosciences), at the base of tail or in one experiment as indicated between the shoulder blades at the neck. In addition, mice received 200 ng of pertussis toxin (Sigma-Aldrich) by intravenous (i.v.) or intraperitoneal (i.p.) injection on day 0 and day 2 after immunization. Disease progression was assessed as described in Table 1 (adapted from (Korn et al., 2007)) and weight was measured once or twice (if an animal reaches a score of 3) per day. Disease onset occurs between day 11 and 13 with the peak of disease typically being between day 15 and 20 and a recovery phase roughly after 30 days post immunization.

Table 1: EAE scoring criteria (adapted from (Korn et al., 2007))

Score	Description
0	No disease signs
0.5	Initial/incomplete tail paralysis
1	Complete tail paralysis
1.5	Impaired righting reflex
2	Weakness of hind limbs
2.5	Paralysis of one hind limb
3	Paralysis of both hind limbs
3.5	Weakness/paralysis of front limbs
4	Front and hind limb paralysis (tetraplegia)
5	Moribund

Mice that lost 20% of the initial body weight or more, had a score of 3.5 or a score of 3 for more than three consecutive days, or showed overall bad general well-being were euthanized immediately.

5.2.1.5 OVA immunization

Mice were immunized by subcutaneous injection with 200 µg of ovalbumin (OVA) peptide 323-339 (ISQAVHAAHAEINEAGR) in CFA, containing 500 µg *Mycobacterium tuberculosis* H37Ra (BD Biosciences), at the base of tail. In addition, mice received 200 ng of pertussis toxin (Sigma-Aldrich) by i.v. or i.p. injection on day 0 and day 2 after immunization.

5.2.1.6 Surgical lymph node preparation for photoconversion and two-photon imaging

Animals were anesthetized with a cocktail of medetomidine (0.5 mg kg⁻¹), midazolam (5 mg kg⁻¹) and fentanyl (0.05 mg kg⁻¹) (MMF) by i.p. injection, and the fur was removed with the use of a depilatory cream (Veet). Body temperature was regulated by a custom made heat mat and their eyes were covered with cream (Bayer) to prevent them from drying out.

In photoconversion experiments, the inguinal LN (iLN) on the anatomical left side of the animal was irradiated with a 405 nm wavelength diode laser (LuxX 405-60, Soliton) through the skin for 20 min and the mesenteric LN (mLN) was irradiated after surgical exposure for 10 min. For surgical exposure of the mLNs, a small incision was made in the skin and abdominal wall of the mouse. The caecum then was pulled from the abdominal cavity and placed on a wet compress to expose the mLNs for irradiation. During the irradiation of the largest mLN (in close proximity to the caecum), the caecum was moisturized with 0.9% sodium chloride solution (Fresenius Kabi). After irradiation of the largest mLN, all organs were placed back into the abdominal cavity and the abdominal wall and skin were sutured. Buprenorphin (0.5 mg kg⁻¹) was used after suturing for pain management of mLN-irradiated mice by subcutaneous injection. Antagonization of the anesthesia was achieved with a cocktail of atipamezole (1.2 mg kg⁻¹), flumazenil (0.5 mg kg⁻¹) and naloxone (2.5 mg kg⁻¹) (AFN) by i.p. injection. The mice were monitored during the wake-up phase and for at least one hour after it was awake to rule out any surgery- or anesthesia-related complications. PhAM^T and PhAM^{L-17} mice were sacrificed for analysis 2 days after LN irradiation and 2D2 x TH x PhAM^T mice were sacrificed for analysis 3 days after LN irradiation.

For two-photon LN imaging experiments, the mice were anaesthetized before tracheotomization, and ventilated with 1.5 % isoflurane during the entire procedure. Electrocardiograms and physiological parameters were monitored throughout the surgery and imaging procedure. Visualization of blood vessels was achieved by i.v. infusion of Texas Red-conjugated dextran (50 µg, 70 kDa) and the largest mLN was exposed as described above. After exposure, the mLN was fixed between a wet compress and a glass cover slip with tissue adhesive on a heated custom-made stage. For exposure of the anatomical left iLN, an incision of the skin was made and the skin was retracted until the iLN was exposed. The iLN was then

cleared from connective and adipose tissue, and fixed between a wet compress and a glass cover slip with tissue adhesive on a heated custom-made stage.

5.2.1.7 Adoptive transfer of T cells

T cells were sorted on a FACS Aria III machine (BD Biosciences) based on CD4 presentation into Clone medium. Cells were washed twice with PBS (400 g, 4 °C, 10 min) and resuspended in PBS for adoptive transfer. 200 µl T cell suspension was transferred i.v. per mouse.

5.2.2 Extraction of genomic DNA and PCR-based genotyping

Crude genomic DNA from frozen tail biopsies was isolated by boiling them in 200 µl tail lysis buffer (500 rpm, 99°C, 30 min). Afterwards the samples were cooled down at room temperature for 15 min and mixed with 200 µl tail neutralization buffer to stop the reaction.

Polymerase chain reaction (PCR) was used to amplify target DNA sequences with sequence-specific primers (chapter 5.1.7) and extracted genomic DNA samples to genotype PhAM^{flxed} reporter mice, CD4-Cre mice, IL-17A-Cre mice, TCR^{MOG} mice (also known as 2D2 mice), and BCR^{MOG} mice (also known as TH mice). The composition of a singleplex and a multiplex PCR reaction sample is shown in Table 2. The cyclor program for PhAM^{flxed} reporter mice (primer ID 1 + 2 for Dendra2 floxed allele and primer ID 1 + 3 for wild type allele, together with primer ID 15 + 16 for an internal standard) and CD4-Cre mice (primer ID 4 + 5 for CD4-Cre allele and primer ID 15 + 16 for an internal standard) is shown in Table 3, for IL-17A-Cre mice (primer ID 6 + 7 for IL17A-Cre allele and primer ID 6 + 8 for wild type allele, together with primer ID 15 + 16 for an internal standard) is shown in Table 4, for TCR^{MOG} mice (primer ID 9 + 10 for TCR^{MOG} allele and primer ID 15 + 16 for an internal standard) is shown in Table 5, and for BCR^{MOG} mice (primer ID 11 + 12 for BCR^{MOG} allele and primer ID 13 + 14 for an internal standard) the program shown in Table 3 with the exception of the annealing temperature which was set to 55°C.

Table 2: PCR reaction mix

Component	Singleplex PCR reaction	Multiplex PCR reaction
	Volume (µl)	
DreamTaq Green PCR Master Mix (2x)	10	10
Pr1 fwd (10 mM)	1	1
Pr1 rev (10 mM)	1	1
Pr2 fwd (10 mM)	-	1
Pr2 rev (10 mM)	-	1
Nuclease-free H ₂ O	6	4
DNA	2	2
Total per reaction	20	20

Table 3: PCR thermal cycler program for PhAM^{flxed} and CD4-Cre mouse genotyping

Step	Temperature (°C)	Duration	Cycles
Initial denaturation	95	2 min	1x
Denaturation	95	30 s	35x
Annealing	57	30 s	
Elongation	72	30 s	
Final elongation	72	5 min	1x
Hold	4	∞	

Table 4: PCR thermal cycler program for IL-17A-Cre mouse genotyping

Step	Temperature (°C)	Duration	Cycles
Initial denaturation	95	2 min	1x
Denaturation	95	20 s	10x (-0.5 °C annealing temperature per cycle)
Annealing	65	15 s	
Elongation	68	10 s	
Denaturation	95	15 s	28x
Annealing	60	15 s	
Elongation	72	10 s	
Final elongation	72	2 min	1x
Hold	4	∞	

Table 5: PCR thermal cycler program for TCR^{MOG}/2D2 mouse genotyping

Step	Temperature (°C)	Duration	Cycles
Initial denaturation	95	5 min	1x
Denaturation	95	20 s	10x (-0.5 °C annealing temperature per cycle)
Annealing	65	15 s	
Elongation	68	1 min	
Denaturation	95	15 s	28x
Annealing	60	15 s	
Elongation	72	1 min	
Final elongation	72	5 min	1x
Hold	4	∞	

Horizontal agarose gel electrophoresis was used to analyze the size of PCR products by separation on a 1.5% agarose gel containing 0.5 µg/ml ethidium bromide in TAE buffer. A 100 bp DNA ladder (Thermo Fisher) was used to estimate the size of the amplified PCR products and samples were run on the gel at 120 V for 30 to 60 minutes.

5.2.3 Cell isolation and cell cultures

5.2.3.1 Preparation of single cell suspension and isolation of mononuclear cells from the CNS

LNs were passed through a 30 μm strainer and spleens were passed through a 70 μm strainer with the plunger of a syringe and washed with DMEM, followed by gravity centrifugation (400 g , 4 $^{\circ}\text{C}$, 10 min). The supernatant was removed after gravity centrifugation and either resuspended in an appropriate volume of DMEM for downstream processing (for LN samples) or underwent erythrocyte lysis with BD Pharm Lyse or ACK lysing buffer for 3 min (for spleen samples). Erythrocyte lysis was stopped by adding DMEM, followed by gravity centrifugation (400 g , 4 $^{\circ}\text{C}$, 10 min), removal of the supernatant, and resuspension in an appropriate volume of DMEM for downstream processing.

For the preparation of mononuclear cells from the central nervous system (CNS), the mice were sacrificed and immediately perfused through the left cardiac ventricle with ice-cold PBS. The brain was removed by dissection and the spinal cord was flushed out with ice-cold PBS by hydrostatic pressure with a 5 ml syringe and a 19 gauge needle. CNS samples were digested with 40 $\mu\text{g ml}^{-1}$ DNase I (Roche Diagnostics) and 1 mg ml^{-1} collagenase D (Roche Diagnostics) at 37 $^{\circ}\text{C}$ and 200 rpm for 30 min. Digested CNS samples were filled up with DMEM, passed through a 100 μm strainer with the plunger of a syringe and washed with DMEM, followed by gravity centrifugation (400 g , 4 $^{\circ}\text{C}$, 10 min). The supernatant was removed after gravity centrifugation. Cells were resuspended in 5 ml 70% percoll and a layer of 5 ml 37% percoll was added carefully on top, followed by percoll gradient centrifugation (640 g , 20 $^{\circ}\text{C}$, 22 min). The mononuclear cells were removed from the interphase, washed, and resuspended in an appropriate volume of DMEM for downstream processing.

5.2.3.2 Cultures for retrovirus production

HEK293A were cultured with complete DMEM and transfected, using the polyethylenimine (PEI) (Polysciences) method, with 6 μg of pMSCV- Δneo -Twitch-2B and 3.5 μg of pCL-Eco plasmid. Culture medium was replaced with new medium 24 h after transfection and the supernatant, containing virus particles, was harvested after 48 and 72 h. Amicon Ultra Filters (100 kDa cut-off, Merck) were used for concentrating viral particles.

5.2.3.3 Retroviral T cell transduction

Single cell suspensions from spleen samples were prepared as described above. B cells were depleted with the Dynabeads B220 depletion kit (Thermo Fisher) and the remaining T cells were cultured in complete DMEM with 0.5 $\mu\text{g ml}^{-1}$ anti-CD3 (500A2, Invitrogen) and anti-CD28 (37.51, Invitrogen) for 48 h. 4×10^6 stimulated T cells per milliliter complete DMEM were mixed with the supernatant of the concentrated viral particles at a dilution of 1:10 and supplemented

with 8 $\mu\text{g ml}^{-1}$ polybrene (Sigma-Aldrich) and 10 ng ml^{-1} IL-2 (PeproTech). T cells were transduced by spinoculation in 12-well plates with 0.5 ml per well (2000 g, room temperature, 90 min).

5.2.3.4 ^3H thymidine incorporation assay

Cells were isolated from iLNs and mLNs of mice at day 8 or day 12 after EAE induction. 300,000 cells per well were cultured in clone medium with 1, 10, or 100 $\mu\text{g/ml}$ MOG(35-55) peptide or anti-CD3 for 72 h and pulsed with 1 μCi of ^3H thymidine for the last 16 h. Cells were harvested and analyzed for thymidine incorporation by scintillation counting (PerkinElmer) in technical triplicates.

5.2.4 Immunohistochemistry

Mice were sacrificed and immediately perfused through the left cardiac ventricle with 30 ml ice-cold PBS and 15 ml 4% PFA. The brain was removed by dissection and the spinal cord was flushed out with ice-cold PBS by hydrostatic pressure with a 5 ml syringe and a 19 gauge needle. Dissected CNS tissue samples were cut into 10 μm -thick cryosections and incubated with 10 mM citrate buffer (pH 6.0) for 20 minutes at 70°C. Samples were treated with blocking solution (antibody diluent, Agilent Technologies), incubated with a primary antibody against CD4 (EPR6855, Abcam) 1:100 for 18 h at 4°C, washed with PBS Tween, and incubated with a secondary antibody against rabbit conjugated with AF647 (Abcam) 1:500 for 1 h at 37°C. Staining of myelin was achieved by the use of FluoroMyelin Red (Invitrogen) 1:50 and sections were washed with PBS Tween and mounted with ProLong Gold antifade mount media (Life technologies).

Images for immunohistochemical analysis were either acquired at 20x magnification with a Nikon Eclipse Ti2 microscope and NIS Elements AR software or at 20x and 60x magnifications with a Leica SP8 confocal microscope and the Leica Applications Suite X software.

5.2.5 Two-photon imaging of Ca^{2+} signaling in transduced T cells

$20\text{-}30 \times 10^6$ Twitch-2B-transduced 2D2 T cells were adoptively transferred 24 h after transduction into C57BL/6J WT EAE mice, 10 days after immunization. The iLN or mLN was prepared for LN imaging as described above 3-4 days after adoptive transfer (day 13-14 after immunization) and analyzed using a time-lapse two-photon laser-scanning microscope with a 10 W Millennia/Tsunami laser. Excitation wavelength was set to 835 nm, routed through a water immersion objective (25x magnification, NA 0.95, Leica) and with a zoom of 2x, areas of 240 x 240 μm were scanned, and 30-50 μm z-stacks were acquired with 3-4 μm z-step. The acquisition rate was in 25.219 s intervals with images line-averaged twice and fluorescent signals were detected using non-descanned photomultiplier tube detectors with 475/50 nm, 537/26 nm, and 630/69 nm band-pass filters.

A Gaussian blur filter was used for image processing before Z-projecting the stacks with maximum intensity to create two-dimensional movies. To generate ratiometric pseudocolor images, the cpVenusCD (FRET) channel was divided by the mCerulean3 (CFP) channel and changed to a fire lookup table. For the tracking of each cell, the cell shape was defined manually in the 2D maximum projection to generate a region of interest (ROI) that was used to follow any cell. The FRET signal was corrected to account for the detected CFP bleed-through of 44% into the FRET channel, as follows: $cFRET = FRET - 0.44 \times CFP$. Ca^{2+} rations were calculated based on the signal intensities of all pixels in each ROI at every given time point.

The threshold to define Ca^{2+} signals was set to a FRET ration of 0.69, which was the cutoff that only 2% of transferred Twitch-2B-transduced 2D2 T cells reached in the mLN of the control immunization mouse group with PBS in CFA. ImageJ v.1.49k was used to calculate the motility parameters based on the ROI coordinates over time.

5.2.6 Flow cytometry analysis and cell sorting

5.2.6.1 Surface antigen staining

Single cell suspensions were transferred into 96-well V bottom plates with 200 μ l per well in DMEM, followed by gravity centrifugation (490 g, 4 $^{\circ}$ C, 5 min), removal of the supernatant and washing with PBS. For dead cell exclusion, LIVE/DEAD fixable Near-IR stain kit (Invitrogen) was used at a dilution of 1:500 in PBS, together with mouse Fc Block (BD Biosciences) at a dilution of 1:200 to avoid Fc-receptor binding. Cells were incubated in 100 μ l of LIVE/DEAD Near-IR/Fc Block mix for 30 min on ice and washed with FACS buffer, followed by staining with fluorochrome-conjugated antibodies in 100 μ l FACS buffer per well for 30 min on ice, which were purchased from either Biolegend, eBioscience, Thermo Fisher or BD Biosciences (see chapter 0 for a full list of antibodies). Afterwards cells were washed twice with FACS buffer and resuspended in 200 μ l FACS buffer for flow cytometry analysis on a CytoFLEX flow cytometer (Beckman Coulter) or a FACS Aria III cell sorter (BD Biosciences). Flow cytometry data were analyzed with FlowJo software.

5.2.6.2 Intracellular antigen staining

The mD2^{RED} reporter signal was conserved with a two-step fixation protocol directly after surface antigen staining, as described above. First, cells were fixed with 200 μ l 1% paraformaldehyde (PFA) in PBS for 15 min on ice and washed twice with PBS. Second, cells were fixed with Fix/Perm buffer from the Foxp3 staining kit (eBioscience) for 30 min on ice, washed twice with Perm buffer (eBioscience), and stained with fluorochrome-conjugated antibodies against intracellular targets in 100 μ l Perm buffer per well. Afterwards cells were washed twice with Perm buffer and resuspended in 200 μ l FACS buffer for flow cytometry

analysis on a CytoFLEX flow cytometer (Beckman Coulter) or a FACS Aria III cell sorter (BD Biosciences). Flow cytometry data were analyzed with FlowJo software.

5.2.6.3 Tetramer staining

Single cell suspensions were transferred into 96-well V bottom plates with 100 μ l per well in DMEM and neuraminidase (Sigma-Aldrich) was added to a final concentration of 0.7 U ml⁻¹ for 30 min at 37 °C and 5% CO₂, followed by gravity centrifugation (490 g, 4 °C, 5 min), removal of the supernatant and washing with PBS. Cells were treated with 10 nM dasatinib (Selleckchem) for 30 min at 37 °C and 5% CO₂, washed twice with PBS, and subsequent tetramer staining with 10 μ l I-Ab OVA 323-339 (MBL) or I-Ab MOG 35-55 (MBL) tetramer and 40 μ l FACS buffer for 2 h at room temperature. Afterwards cells were washed twice with PBS and followed by surface antigen staining as described above.

5.2.6.4 Cell hashing for scRNA-seq

For cell hashing, surface antigen staining was performed as described above, with the addition of adding TotalSeq Hashtag antibodies for surface antigen staining. TotalSeq-A anti-mouse Hashtag 1 to 12 (M1/42; 39-F11; Biolegend) antibodies were used in combination with the 10x Chromium Single Cell 3' Solution Kit and TotalSeq-C anti-mouse Hashtag 1 to 9 (M1/42; 39-F11; Biolegend) antibodies were used in combination with the 10x Chromium Single Cell 5' Solution Kit. TotalSeq Hashtag antibodies were added to the anti-surface antigen antibody mix and centrifugated on a table top centrifuge (21,000 g, 4 °C, 10 min) prior to cell staining. Cells were stained with 100 μ l antibody mix, containing a different TotalSeq antibody per sample to demultiplex samples based on the hashtag barcode sequence during sequencing analysis.

5.2.6.5 Fluorescence-activated cell sorting

Single cell suspensions of iLNs, mLNs, spleen, and CNS from mice were prepared and surface antigens were stained as described above. For single-cell RNA sequencing (scRNA-seq) and bulk RNA sequencing (RNA-seq) experiments, cells were stained with LIVE/DEAD Near-IR, which was omitted for adoptive transfer experiments due to cytotoxicity. Stained cells were resuspended in FACS buffer and sorted on a FACS Aria III machine (BD Biosciences) into the appropriate buffer for downstream processing.

5.2.7 Sequencing

5.2.7.1 scRNA-seq

Two different mouse scRNA-seq experiments were performed in this thesis. For both experiments, single cell suspensions of LNs, spleen, and CNS samples from irradiated PhAM^T EAE mice were prepared 2 days after photoconversion of T cells at disease onset as described above. Cells were incubated in 100 μ l of LIVE/DEAD Near-IR/Fc Block mix for 30 min on ice and washed with FACS buffer, followed by staining with fluorochrome-conjugated and cell

hashing antibodies in 100 μ l FACS buffer per well for 30 min on ice. Afterwards cells were washed twice with FACS buffer and resuspended in 300 μ l FACS buffer for cell sorting on a FACS Aria III machine (BD Biosciences). Photoconverted T cells were sorted on live $mD2^{red}CD4^{+}CD44^{high}CD8\alpha^{-}$ into 100 μ l PBS with 2% BSA for scRNA-seq.

In the first experiment (described in chapter 6.6), scRNA-seq, single-cell T cell receptor sequencing (scTCR-seq), and cell hashing libraries were prepared using the Chromium Single Cell 5' Solution (Chromium Next GEM Single Cell VDJ v1.1 with feature barcoding technology for cell surface protein, 10x Genomics). For the other experiment (described in chapter 6.7 and 6.8), the Chromium Single Cell 3' Solution (Chromium Single Cell 3' v3, 10x Genomics, combined with cell hashing according to a published protocol (Stoeckius et al., 2018)) was used to detect more genes per cell compared to the Chromium Single Cell 5' Solution (10x Genomics). The sorted photoconverted T cells were centrifugated, the supernatant was removed, and resuspended in the Chromium mastermix plus 37.8 μ l water. 70 μ l of the cell mix were loaded to a Chromium chip and the pellet of the loaded cells was checked by microscopy to ensure that all cells were loaded onto the chip. Every further step was performed according to the manufacturer's protocol (10x Genomics). Libraries were quality controlled with a Bioanalyzer 2100 (Agilent Technologies) as recommended in the manufacturer's protocol, quantified with the Qubit dsDNA hs kit (Life Technologies), and sequenced on a HiSeq 2500 (Illumina) using read lengths of 28 base pairs (bp) read 1, 8 bp i7 index, 91 bp read 2.

5.2.7.2 scRNA-seq data processing

Samples were demultiplexed, raw data was processed, reads were aligned to the mouse mm10 reference genome, and molecular identifier (UMI) counts were summarized with the Cell Ranger software (10x Genomics, v.3.1.0).

Hashing-barcode matrices and filtered gene-barcode matrices were subjected to a pre-screening process and only matrices that contained barcodes with UMI counts that passed the cell detection threshold were used for further analysis. The CITE-seq-Count software version 1.4.3 (Zenodo) was used for cell hashing analysis of Chromium Single Cell 3' v3 libraries and the filtered UMI count matrices were processed with the R package Seurat version 3.1 (Butler et al., 2018; Stuart et al., 2019). Centered log ratio (CLR) transformation was used to normalize cell hashing raw counts by dividing the raw counts by the geometric mean of a hashtag oligonucleotide (HTO) across cells and subsequent log-transformation. Doublets, where one single barcoded cell contained two different HTOs, and cells that did not contain any HTO were removed from further analysis. Additionally, cells that contained less than 200 or more than 5000 genes were excluded as well as cells where 10% or more of the counts were mitochondrial genes. After performing these quality control steps, the raw gene counts from the remaining high-quality single cells were subjected to log-normalization, identification of

high variable genes via the *MeanVarPlot* method, scaling, and regression against the number of UMIs and mitochondrial RNA content per cell.

For the combined scRNA-seq and scTCR-seq analyses in chapter 6.6, the Chromium Single Cell 3' and 5' datasets were combined, batch effects were removed by integration, and the data was subjected to principal component analysis and unsupervised clustering. Marker identification was performed for each cluster and TCR annotation and repertoire analysis was performed using the Cell Ranger VDJ pipeline (10x Genomics) on cells where a TCR clonotype could be detected. The CDR3 information and frequency of each detected clonotype was added to the Seurat meta.data file and the combined the Chromium Single Cell 3' and 5' dataset was used for the generation of input files for the VDJtools software in order to run comparative post analysis of the CDR3 repertoires.

For the scRNA-seq analyses in chapter 6.7 and 6.8, only the Chromium Single Cell 3' dataset was used for the principal component analysis, unsupervised clustering, and identification of differentially expressed genes in each cluster and tissue per irradiation group.

5.2.7.3 RNA-seq

One bulk RNA-seq experiment was performed in this thesis in chapter 6.10. Single cell suspensions of spleen samples from irradiated 2D2 x TH PhAM^T EAE mice were prepared 3 days after photoconversion of T cells at disease onset as described above. Cells were incubated in 100 µl of LIVE/DEAD Near-IR/Fc Block mix for 30 min on ice and washed with FACS buffer, followed by staining with fluorochrome-conjugated antibodies in 100 µl FACS buffer per well for 30 min on ice. Afterwards cells were washed twice with FACS buffer and resuspended in 300 µl FACS buffer for cell sorting on a FACS Aria III machine (BD Biosciences). 300 photoconverted T cells were sorted on live mD2^{red}CD4⁺CD44^{high}CD8α⁻ into 10 µl TCL buffer (Qiagen) and total RNA was isolated with the RNeasy Plus Micro kit (Qiagen). RNA integrity and quality was confirmed via a Bioanalyzer 2100 (Agilent Technologies) and library preparation for bulk RNA-seq of poly(A)-RNA was done as described previously (Parekh et al., 2016). In short, a Maxima RT polymerase (Thermo Fisher) was used together with oligo-dT primers that contain barcodes, UMIs, and an adaptor, in order to generate barcoded cDNA. A template switch oligo (TSO) was used to extend cDNA ends and full-length cDNA was amplified with TSO-site- and adaptor-binding primers. cDNA was fragmented with the Ultra II FS kit (NEB), subjected to end repair and A-tailing, and ligation of a TruSeq adaptor. Finally, 3'-end-fragments were amplified using primers with Illumina P5 and P7 overhangs. To achieve better cluster recognition, the previously described protocol that was used here (Parekh et al., 2016) was modified in regards to an exchange of the P5 and P7 sites, to allow cDNA sequencing in read1 and barcodes and UMIs in read2. Libraries were sequenced on a NextSeq 500 (Illumina) with 67 cycles for cDNA in read1 and 16 cycles for barcodes and UMIs in read2

and data was processed with the Drop-seq pipeline (v1.0) (Macosko et al., 2015) for the generation of sample- and gene-wise UMI tables. The reference genome (GRCm38) was used for alignment and GENCODE version M25 was used for the definitions of transcripts and genes.

5.2.7.4 ATAC-seq

One assay for transposase-accessible chromatin with sequencing (ATAC-seq) experiment was performed in this thesis in chapter 6.9 as previously described (Corces et al., 2017) with minor modifications for low cell numbers. Single cell suspensions spleen samples from irradiated PhAM^T EAE mice were prepared 2 days after photoconversion of T cells at disease onset as described above. Cells were incubated in 100 μ l of LIVE/DEAD Near-IR/Fc Block mix for 30 min on ice and washed with FACS buffer, followed by staining with fluorochrome-conjugated in 100 μ l FACS buffer per well for 30 min on ice. Afterwards cells were washed twice with FACS buffer and resuspended in 300 μ l FACS buffer for cell sorting on a FACS Aria III machine (BD Biosciences). Photoconverted T cells were sorted on live mD2^{red}CD4⁺CD44^{high}CD8 α ⁻ into 100 μ l FACS buffer for ATAC-seq.

Cells were washed with ice-cold ATAC Resuspension buffer, pelleted (500 g, 4°C, 10 min), and resuspended in at least 10 μ l of ATAC Lysis Plus Transposition mixture. Samples were then incubated in a thermomixer (1000 rpm, 37°C, 30 min) for combined lysis and transposition in order to avoid cell loss. The PCR Clean-up MinElute kit (Qiagen) was used to purify and elute the DNA in 10 μ l of Tris Elution buffer. A published protocol (Buenrostro et al., 2013) was used to amplify transposed DNA in 50 μ l reaction volumes with custom primers. In short, libraries were amplified for 4 cycles and monitored via qPCR for the delta normalized reporter value (Δ RN) with the same primers. To estimate the number of additional cycles needed for the PCR reactions, a 0.25 Δ RN cycle number was used. The PCR Clean-up MinElute kit (Qiagen) was used to purify the amplified libraries, which were then size-selected for fragments with less than 600 bp using Agencourt AMPure XP beads (Beckman Coulter), and their quality was assessed by Qubit and Bioanalyzer analysis. Libraries were sequenced according to the standard Illumina protocol for 50 bp single-end reads on a HiSeq 1500 (Illumina).

5.2.8 Quantification and statistical analysis

Unpaired Student's t test was used to compare two groups of cell frequency measurements, cell numbers, mRNA amounts, and protein levels. Two-tailed p values of less than 0.05 were considered significant. One-way-ANOVA was used to compare EAE scores of two groups per day and post hoc testing was performed as indicated. Kaplan-Meier analysis was performed to generate EAE survival curves and p values were calculated with log-rank testing (Mantel-Cox). p values of less than 0.05 were considered significant. Graph Pad Prism v7.05 was used for the calculation of p values and the generation of graphs.

For ATAC-seq, Bowtie v.1.1.2 was used to align ATAC-seq reads to the mouse genome mm10 using the options "-q -n 2 --best --chunkmbs 2000 -p 32 -m 1 -S." (Langmead, 2010) and picard MarkDuplicates was used to remove duplicate reads. HOMER v.4.9 was used to identify ATAC peaks over input background with the findPeaks.pl function and the option "-style factor" (Heinz et al., 2010). Differentially open chromatin peaks were identified by at least a 2-fold difference between open chromatin peaks of two different irradiation groups. The HOMER (v.4.9) annotatePeaks.pl function was used for genomic feature annotation of differentially open chromatin peaks.

Gene Set Enrichment Analysis (GSEA) v.4.0.3 was used to test the i- and m-core gene signatures (from Figure 14b) in RNA-seq data of i- and m-T cells from the LNs and spleens of iLN- or mLN-labeled 2D2 × TH PhAM^T mice. GSEA was performed with default options, with the exception of the permutation type, which was set to "gene_set". Normalized Enrichment Scores (NES) and False Discovery Rates (FDR) were calculated as described in (Subramanian et al., 2005).

Transcription factor activity scores in figure Figure 14d were assessed with the Python tool Regulatory Genomics Toolbox for the i- and m-core gene signatures (from Figure 14b) and ranked by activity score.

5.2.9 Data availability

NGS raw data and processed gene expression data have been deposited into the GEO repository under the accession number GSE156718 (scRNAseq mouse), GSE172513 (ATACseq mouse), and GSE171122 (bulk RNAseq mouse).

6 Results

The current concept of organ-specific autoimmunity is that autoreactive T cells are primed in secondary lymphoid organs and then home to their target organ where they induce an autoimmune response. In order to investigate how the priming site shapes the T cell response in experimental autoimmune encephalomyelitis (EAE), a preclinical disease model for human multiple sclerosis (MS), I generated an *in vivo* provenance system for T cells to follow them from their priming site to their target organ, the central nervous system (CNS).

The majority of the presented data in this thesis was published in (Hiltensperger et al., 2021) and permission for usage was kindly granted by Springer Nature.

6.1 Characterization of light-mediated CD4⁺ T cell labeling

Due to the limitation of other labeling systems that are restricted when it comes to targeting of cells in a site-specific manner (e.g. tamoxifen-inducible Cre-ER (Metzger et al., 1995)), I used a transgenic mouse strain with the photoconvertible fluorescent reporter Dendra2 (switchable from green to red fluorescence), called PhAM^{floxed} (Pham et al., 2012), which is localized in the mitochondria (mito-Dendra2 or short mD2). In this model, mD2 expression is Cre-dependent to allow for tissue-specific labeling of cells. In order to generate a system that can be used to label and track the migration of CD4⁺ T cells, the PhAM^{floxed} strain was crossed with a CD4-Cre driver strain (Lee et al., 2001) to generate PhAM^T mice.

All CD4⁺ T cells (but also CD8⁺ T cells) in PhAM^T mice express the green fluorescent reporter mD2^{GREEN} (see gating strategy in Figure 4a). Irradiation of *in vitro*-activated CD4⁺ T cells for 1, 3, and 5 min with a 405 nm diode laser photoconverted all cells from mD2^{GREEN} to mD2^{RED} and the red signal could be followed for up to 3 days via flow cytometry (Figure 4b). Of note, photoconverted T cells do not lose their mD2^{GREEN} signal, but are mD2^{GREEN}mD2^{RED} double positive. Additionally, experiments where CD4⁺ T cells were stained with a cell proliferation dilution dye showed that photoconverted T cells retained their mD2^{RED} signal for up to 5 cell divisions (Figure 4c). To assess the labeling *in vivo*, PhAM^T mice were anesthetized and the inguinal LN (iLN) was surgically exposed and irradiated for 5, 10, and 15 min. To achieve complete lymph node (LN) laser light penetration, the irradiation times were increased compared to experiments with cell suspensions. The mD2^{RED} signal and the fraction of live cells, which stained negative for a cell viability dye, in the CD4⁺ T cell compartment were analyzed directly after irradiation via flow cytometry (Figure 4d). All three irradiation durations were sufficient to photoconvert all CD4⁺ T cells in the surgically exposed iLN and none caused any immediate cell death. However, the mean fluorescent intensity (MFI) of mD2^{RED} was positively correlated with the irradiation duration. Moreover, direct irradiation of the iLN through the skin was also sufficient to photoconvert all T cells (Figure 4e), thus providing a non-invasive labeling method.

These findings indicated that the PhAM^T strain could be used to label all T cells in a LN and follow them for a few cell divisions.

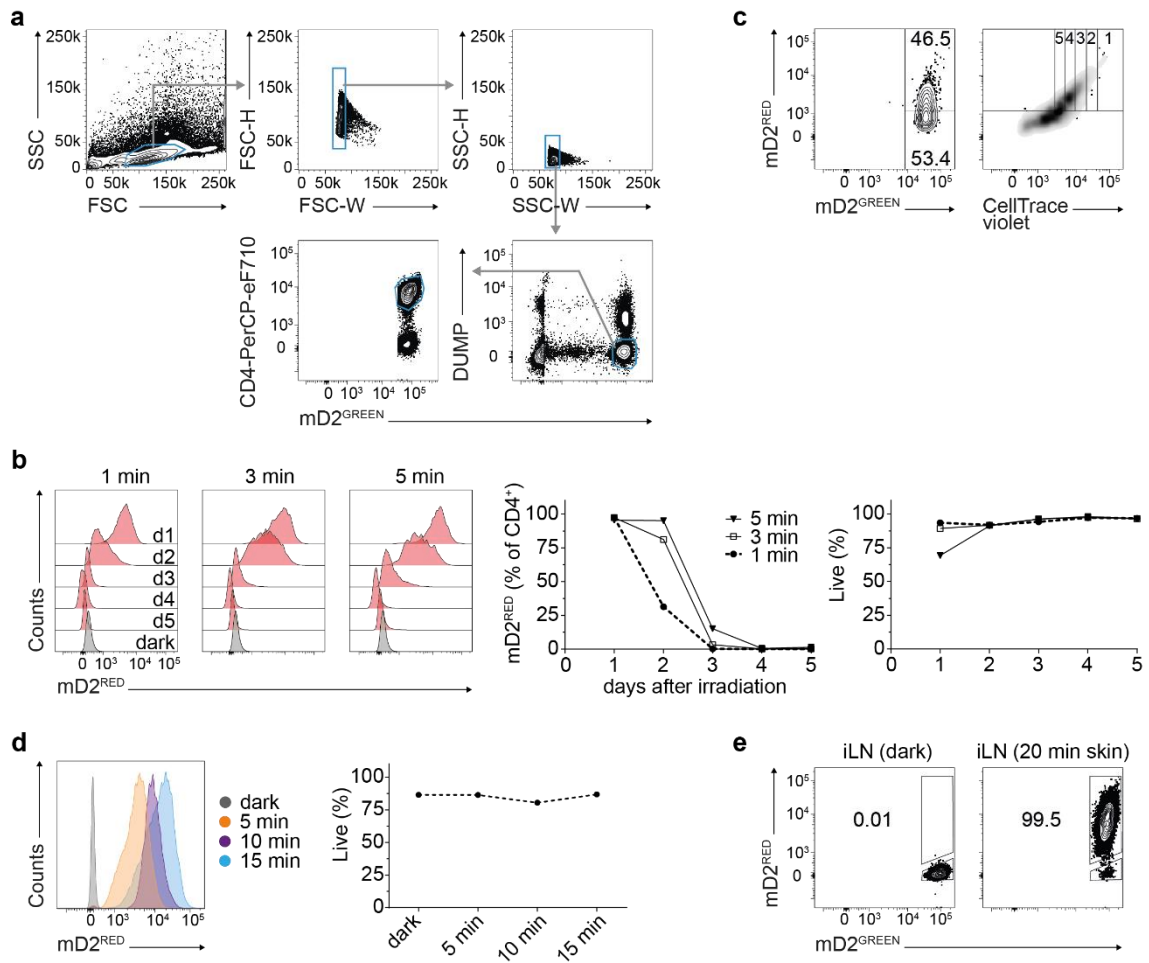


Figure 4: Characterization of the PhAM^T reporter line.

a, Flow cytometry gating strategy for mD2^{GREEN} or mD2^{RED} CD4⁺ T cells. The DUMP channel is comprised of LIVE/DEADTM-Near-IR and CD8α-APC-Cy7 positive cells. **b**, **c**, Flow cytometry analysis of mD2^{RED} reporter signal in MACS-purified CD4⁺ T cells from spleens of PhAM^T mice, which were *in vitro*-activated (4 μg ml⁻¹ anti-CD3; 2 μg ml⁻¹ anti-CD28), further cultured in the presence of IL-2 (10ng/ml), and irradiated with 405nm light at the indicated time points in the absence of a cell proliferation dye (b) or 4 days before analysis in the presence of a cell proliferation dye (c). The histograms and contour plots were pre-gated on CD4⁺mD2^{GREEN} cells and excluded cell debris, doublets, dead cells, and CD8α⁺ cells. Representative plots of one PhAM^T mouse from 2 independent experiments. **d**, **e**, Flow cytometry analysis of mD2^{RED} reporter signal in CD4⁺ T cells from inguinal LNs (iLNs) of PhAM^T mice. iLNs were irradiated *in vivo* with 405 nm light for the indicated durations either surgically exposed (d) or through the shaved skin (e). The histograms and contour plots were pre-gated on CD4⁺mD2^{GREEN} cells and excluded cell debris, doublets, dead cells, and CD8α⁺ cells. Representative plots of one PhAM^T mouse per time point from 2 independent experiments.

6.2 Lymph node dynamics of CD4⁺ T cells in naïve and immunized mice

iLNs are the draining LNs in our EAE model, which is induced by subcutaneous immunization of myelin oligodendrocyte glycoprotein (MOG) peptide 35-55 in complete Freund's adjuvant (CFA). Due to mounting evidence from preclinical models and MS patients that the gut microbiome might play a role in shaping the response of T cells in the CNS (Kirby and Ochoa-Reparaz, 2018), I studied the population dynamics of photoconverted (mD2^{RED}) CD4⁺ T cells

in the iLN and in the mesenteric LN (mLN) in naïve and MOG₃₅₋₅₅/CFA immunized PhAM^T mice by photoconverting all T cells in these two LN stations (Figure 5a).

The fraction of photoconverted CD4⁺ T cells overall (Figure 5b) and naïve T cells (CD4⁺CD44^{int}CD62L^{high}) in particular (Figure 5c) decreased rapidly over 2 days in iLN-irradiated PhAM^T mice during steady state and this process was entirely blocked by FTY720, which inhibits the egress of T cells out of secondary lymphoid organs. This suggested that the rapid reduction of photoconverted naïve T cells was due to egress of these cells out of the LN and not due to a loss of signal or phototoxicity. In comparison, the fraction of photoconverted antigen-experienced T cells (CD4⁺CD44^{high}Foxp3⁻) increased over time (Figure 5c), indicating that these cells remain longer in the LN as compared to naïve T cells. FTY720-treated animals showed no difference in the fraction of antigen-experienced T cells over time (Figure 5c). Next, the iLN of immunized EAE mice was irradiated on day 4 after immunization and analyzed on day 6. The fraction of photoconverted naïve T cells decreased rapidly in iLN-labelled EAE mice and FTY720 again blocked the dynamics of naïve T cells, whereas the fraction of photoconverted antigen-experienced T cells increased (Figure 5d).

Interestingly, in iLN, the fraction of photoconverted Foxp3⁺ regulatory T (Treg) cells was larger compared to conventional T (Tcon) cells after 2 days of iLN-labeling in steady state (Figure 5e). In contrast, in mLN, the fraction of photoconverted Treg cells did not surpass the fraction of labeled Tcon cells in steady state, suggesting that in mLN, constant antigen-specific priming (potentially directed to microbial antigens) that favors Tcon responses over Treg responses might be occurring (Figure 5e). After active immunization with subcutaneous antigen deposit, the fraction of photoconverted Tcon cells surpassed the number of Treg cells also in iLN (Figure 5f) likely as a result of antigen-specific priming to MOG(35-55) peptide in the iLN as the draining LN of the site of immunization.

In summary, T cells of PhAM^T mice can be photoconverted in the iLN and mLN and followed for at least 2 days during steady state and after antigen-specific activation in the EAE paradigm.

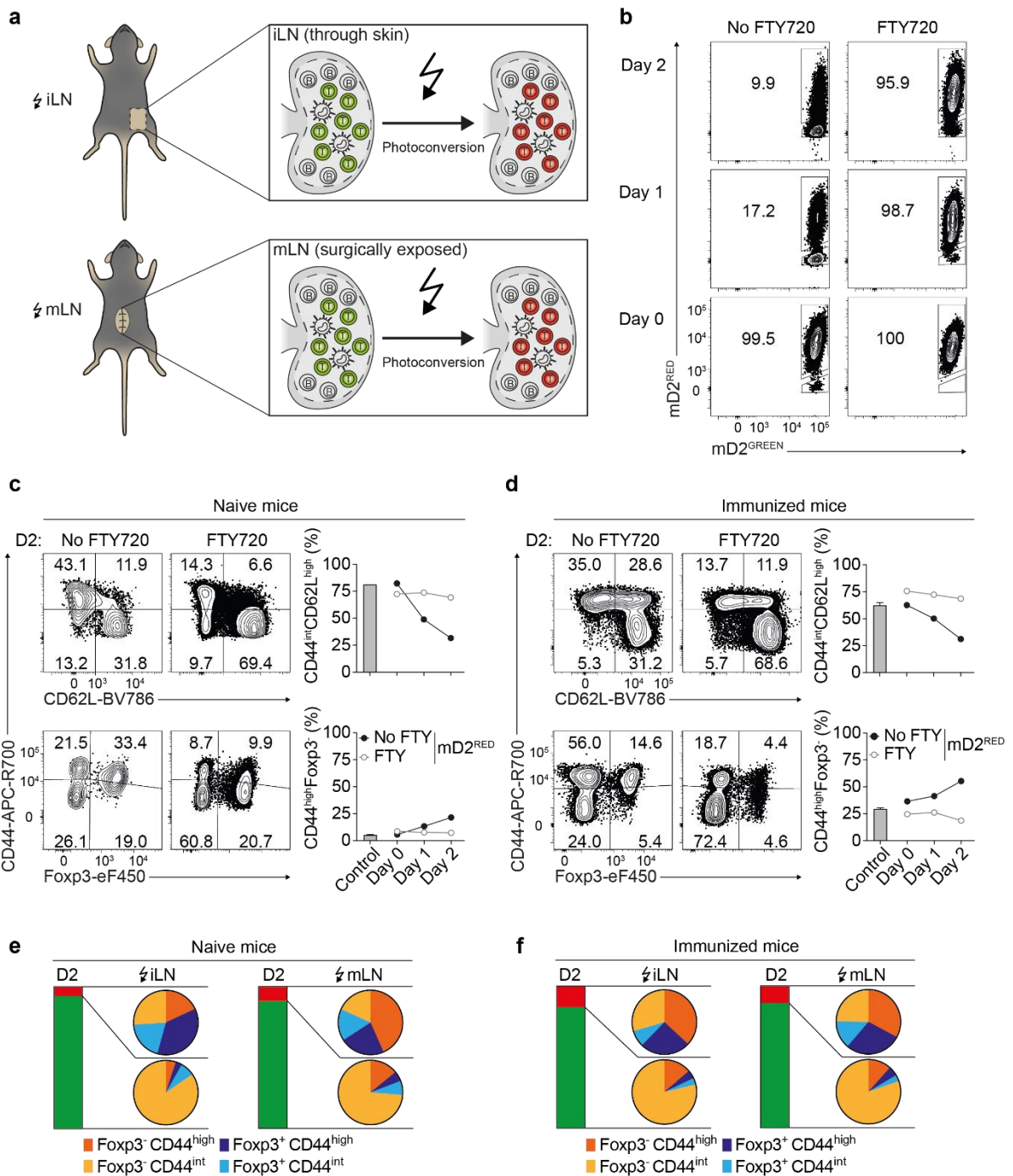


Figure 5: Lymph node dynamics of CD4⁺ cells.

a, Schematic of inguinal lymph node (iLN) and mesenteric lymph node (mLN) irradiation with 405 nm light. Irradiation is depicted as lightning symbol. **b**, Flow cytometry analysis of the irradiated iLN in PhAM^T mice during steady state 0, 1, and 2 days after iLN irradiation. Mice received either normal drinking water (left column) or drinking water with FTY720 (2 µg/ml) 5 days before irradiation and until the end of the experiment (right column). The contour plots were pre-gated on CD4⁺mD2^{GREEN} cells and excluded cell debris, doublets, dead cells, and CD8α⁺ cells. Representative plots of one PhAM^T mouse per time point from 2 independent experiments. **c**, **d**, Flow cytometry analysis of the iLN in PhAM^T mice during steady state (**c**) or on day 4 after experimental autoimmune encephalomyelitis (EAE) induction (**d**). The contour plots show day 2 after irradiation and were pre-gated on mD2^{RED}CD4⁺ cells and excluded cell debris, doublets, dead cells, and CD8α⁺ cells. Representative plots of one PhAM^T mouse per time point and one non-photoconverted dark control (pre-gated on mD2^{GREEN}CD4⁺, bar to the left) from 2 independent experiments. **e**, **f**, Population dynamics of conventional T cells (Foxp3⁻) and regulatory T cells (Foxp3⁺), assessed according to their CD44 status, 2 days after photoconversion in steady state (**e**) and on day 6 after immunization (**f**) depicted as pie charts. Bar diagrams represent the frequencies of mD2^{RED}CD4⁺ cells 2 days after photoconversion in the iLN (left) and mLN (right). Representative plots from 2 independent experiments.

6.3 Migration pattern of i- and m-T cells during CNS autoimmunity

T cell translocation from the peripheral immune compartment into the CNS drives autoimmune inflammation in early disease stages of MS (Korn and Kallies, 2017). Therapies with Natalizumab, a monoclonal antibody against $\alpha 4$ -integrin, which is part of the VLA-4 complex that has been linked to T cell infiltration into the CNS, show great efficacy in controlling inflammation in the CNS in MS (Butzkueven et al., 2014). In an effort to use our model of spatiotemporal T cell labeling to study T cell infiltration patterns from different peripheral LN stations in the context of CNS autoimmunity, I induced EAE in PhAM^T mice and irradiated either the iLN or the largest mLN (Figure 5a) at disease onset (score of 1; between day 11 and 13 after immunization) to photoconvert the T cells in these LN stations. Two days later, irradiated LNs (iLN or mLN), distant LNs (mLN or iLN), spleen, spinal cord, and brain were analyzed (Figure 6a).

Photoconverted T cells (mD2^{RED}CD4⁺) could be found not only in all analyzed peripheral immune compartments but also in the spinal cord and the brain (Figure 6b). Of note, the variance in the frequencies of photoconverted T cells within the group of iLN- or mLN-irradiated mice and between groups was very low, most likely because T cell migration is a highly robust physiological process. Moreover, the highest frequencies could always be found in the irradiated LNs, indicating that a substantial portion (approximately 30%) of photoconverted T cells remained in the irradiated LNs for 2 days. When characterizing the activation status of the photoconverted T cells compared to non-photoconverted T cells (mD2^{GREEN}CD4⁺), antigen-experienced T cells (mD2^{RED}CD4⁺CD44^{high}CD62L^{int}) were found in the irradiated LN, spleen and CNS but were mostly absent in the distant LN (Figure 6c). The lack of photoconverted antigen-experienced T cells in the distant LN suggested that no significant cross-trafficking of antigen-experienced T cells occurred between iLN and mLN in our EAE model and that iLN-derived T cells (i-T cells) and mLN-derived T cells (m-T cells) migrate through the spleen into the CNS. Consistent with these findings, no significant cross-trafficking of antigen-experienced T cells between iLN and mLN was observed at earlier time points, when the iLN of EAE mice was irradiated at day 6, 7, 8, and 9 and analyzed two days later (Figure 7). Furthermore, the frequencies of photoconverted antigen-experienced T cells were significantly increased compared to non-photoconverted T cells in the irradiated LN, which is most likely due to a combined effect of egress of naïve T cells, retention of Treg and Tcon cells, and the priming of Tcon cells as shown above (Figure 6c).

Taken together, both i- and m-T cells were able to infiltrate into the CNS and did so likely by a route through the spleen but not through the mLN or iLN, respectively.

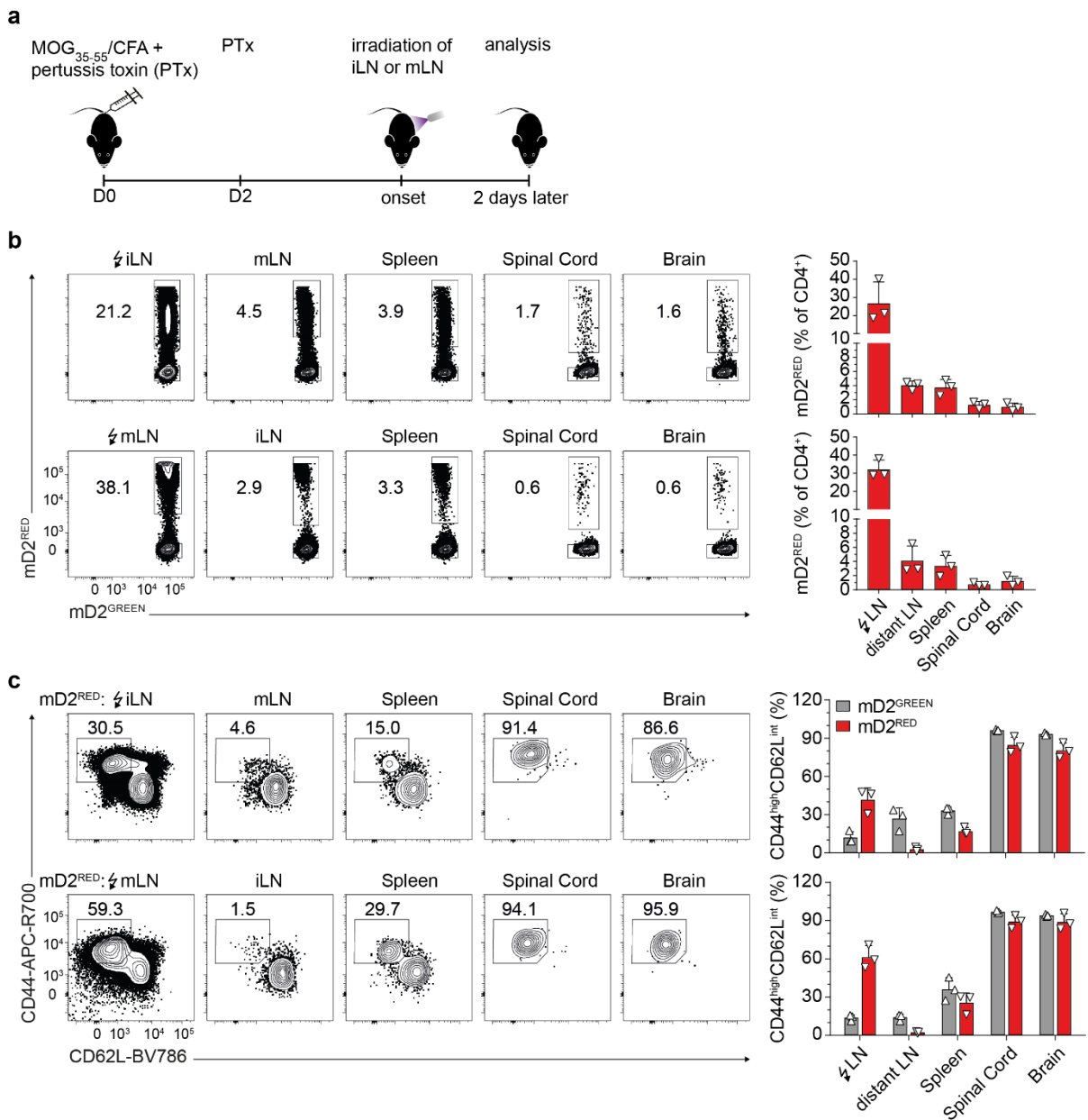


Figure 6: Migration patterns of i- and m-T cells during EAE.

a, Schematic of experimental autoimmune encephalomyelitis (EAE) induction and photoconversion of T cells in the inguinal lymph node (iLN) or mesenteric lymph node (mLN) in PhAM^T mice. Complete Freund's adjuvants (CFA); pertussis toxin (PTx). **b**, **c**, Flow cytometry analysis of different tissues in PhAM^T EAE mice regarding the mD2^{RED} frequencies in the CD4⁺ compartment (**b**) or the frequencies of antigen-experienced T cells (CD44^{high}CD62L^{int}) in the mD2^{GREEN} and mD2^{RED} compartment (**c**). The contour plots show day 2 after irradiation at disease onset and were pre-gated on CD4⁺ (**b**) or mD2^{RED}CD4⁺ cells (**c**) and excluded cell debris, doublets, dead cells, and CD8 α ⁺ cells. Summary of one experiment with 3 mice per group (iLN irradiation upper row, mLN irradiation lower row) is shown by the bar graphs. Representative plots of 3 PhAM^T mice per group and 3 independent experiments; irradiation is depicted as lightning symbol; bars represent mean + s.d.

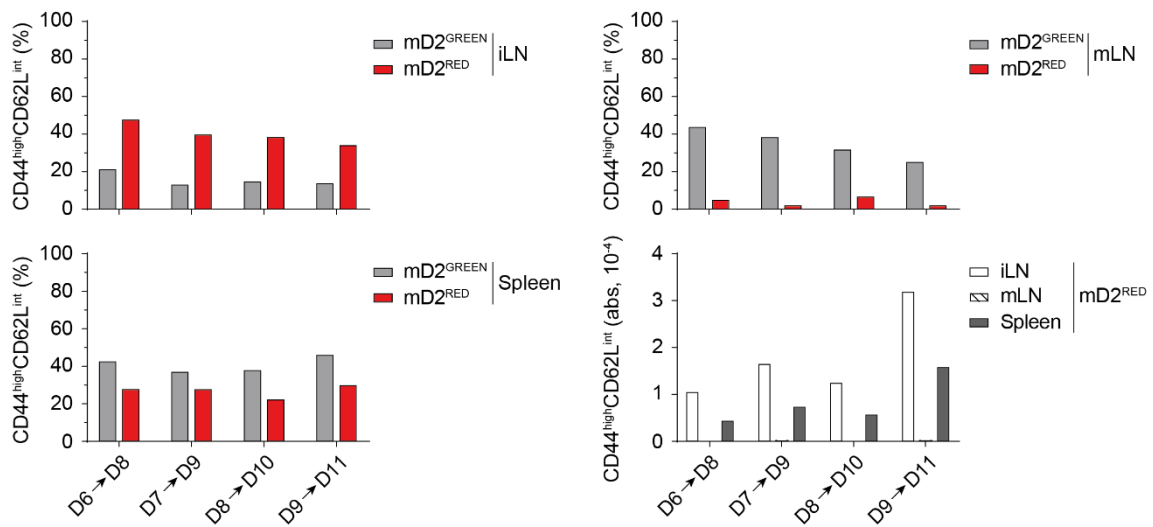


Figure 7: Migration patterns of i-T cells at different time points during EAE.

Flow cytometry analysis of photoconverted (mD2^{RED}) and non-photoconverted (mD2^{GREEN}) T cells in different tissues in PhAM^T experimental autoimmune encephalomyelitis (EAE) mice regarding their CD44^{high}CD62L^{int} status. The left inguinal lymph node (iLN) was irradiated at indicated time points after EAE induction and analyzed 2 days later. Bar graphs show fractions or absolute numbers of CD44^{high}CD62L^{int} cells in the mD2^{RED} or mD2^{GREEN} compartment. Cells were pre-gated on CD4⁺ cells and excluded cell debris, doublets, dead cells, and CD8α⁺ cells. Representative plot of one PhAM^T mouse per time point from 2 independent experiments.

6.4 i- and m-T cells in the CNS are distinct

iLN and mLN likely provide a distinct priming environment in our EAE model. Importantly, iLNs are draining LNs due to the induction method of EAE via tail-based subcutaneous immunization. However, due to the massive deposition of antigen at the site of immunization, antigen spillover is likely to occur (Kijanka et al., 2014) so that MOG(35-55) peptide will also be presented to T cells in mLN. Here, I hypothesized that the priming milieu in this LN station will differ from the priming milieu in iLN, either due to differences in the amount of available antigen or due to a different adjuvanticity in mLN as compared to iLN. In order to test these hypotheses, i-T cells and m-T cells were phenotypically analyzed by flow cytometry in the LN station of origin, in the spleen, and in the CNS.

First, the fraction of Foxp3⁺ Treg cells was higher within m-T cells than in i-T cells in the CNS (Figure 8a). On the other hand, the fraction of CD69-expressing cells was higher in i-T cells than in m-T cells (Figure 8b). Of note, more photoconverted Tcon cells expressed CD69 in the irradiated LN (after 2 days) as compared to their non-photoconverted counter parts, which is expected as CD69 is responsible for tissue retention (Cibrian and Sanchez-Madrid, 2017).

To summarize, CNS-infiltrating i- and m-T cells were distinct in the expression of a series of markers, including Foxp3 and CD69, suggesting that their phenotypes and overall transcriptional signatures might also be different.

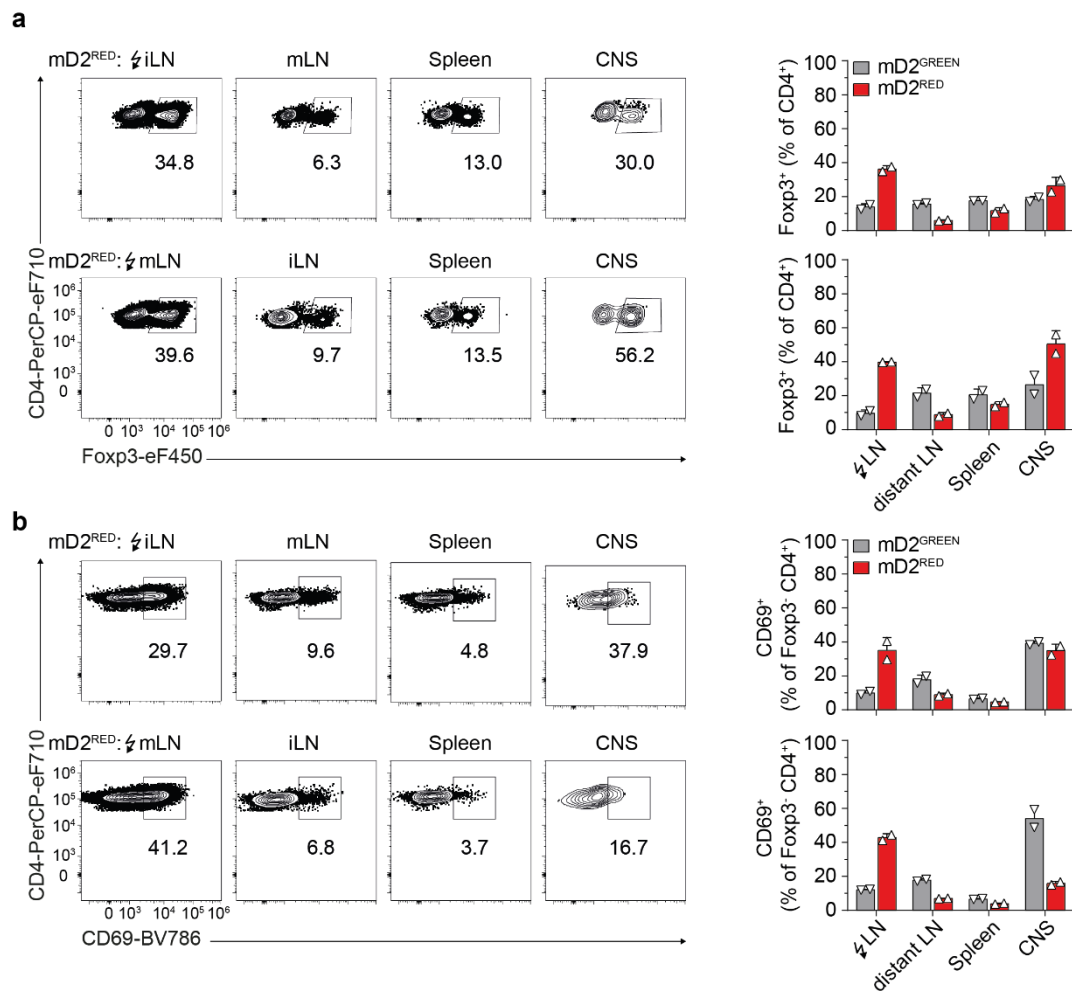


Figure 8: Phenotyping of i- and m-T cells during EAE.

a, b, Flow cytometry analysis of photoconverted (mD2^{RED}) and non-photoconverted (mD2^{GREEN}) T cells in different tissues in PhAM^T experimental autoimmune encephalomyelitis (EAE) mice regarding the Foxp3 frequencies in the CD4⁺ compartment (**a**) or the fractions of CD69 cells in the Foxp3⁺CD4⁺ compartment (**b**). The contour plots show day 2 after irradiation at disease onset and were pre-gated on mD2^{RED}CD4⁺ cells and excluded cell debris, doublets, dead cells, and CD8 α ⁺ cells. Summary of one experiment with 2 mice per group (iLN irradiation upper row, mLN irradiation lower row) is shown by the bar graphs. Representative plots of 3 PhAM^T mice per group and 3 independent experiments; irradiation is depicted as lightning symbol; bars represent mean + s.d.

6.5 Antigen-specific priming of CD4⁺ T cells occurs in iLN and mLN

Antigen-specific priming has been shown to occur in the draining iLNs in our EAE model. However, it has not been clear whether antigen-specific priming also takes place in mLNs. In order to test this, antigen-specific proliferation was assessed with a ³H thymidine incorporation assay.

LN cells were isolated at day 8 and day 12 after immunization and stimulated with either MOG(35-55) peptide in varying concentrations or anti-CD3 ϵ antibodies (Figure 9a). Cells from iLN proliferated in a dose-dependent manner in response to MOG(35-55) peptide at both time points. In contrast, mLN-derived T cells failed to show a clear MOG-specific response at day 8. However, on day 12, mLN-derived T cells responded to MOG(35-55) peptide in a dose-dependent manner even though the detected signal in counts per minutes (c.p.m.) was lower

in mLN samples compared to iLN samples. Altogether, these data suggested that MOG(35-55)-specific priming of T cells occurred in both LN stations at later time points after immunization.

To follow up on this *in vitro* experiment, another approach was used to confirm that there is indeed antigen-specific priming in both LN stations occurring *in vivo*. Therefore, transgenic T cell receptor (TCR)^{MOG} (2D2) T cells were transduced with a Ca²⁺ sensor expression cassette (Kyratsous et al., 2017), transferred in host mice at day 10 post immunization with MOG(35-55) or PBS in CFA, and 3 to 4 days post transfer the iLN or mLN was imaged by two-photon microscopy. TCR-specific activation in response to MOG(35-55) antigen was detected in both iLN and mLN (Figure 9b,c; experiments and analyses were performed by Isabel J. Bauer and Naoto Kawakami), again suggesting that at this time point after immunization MOG-specific priming took place in both LN stations. Moreover, i-T cells and m-T cells isolated from the CNS both bound to IAb-MOG tetramers (Figure 9d), indicating that MOG-specific i- and m-T cells infiltrated into the CNS.

These data supported the notion that T cells were primed in a MOG-specific manner at disease onset not only in draining iLNs but also in mLNs and that MOG-specific i- and m-T cells reached the CNS within 2 days after T cell labelling in the irradiated LN.

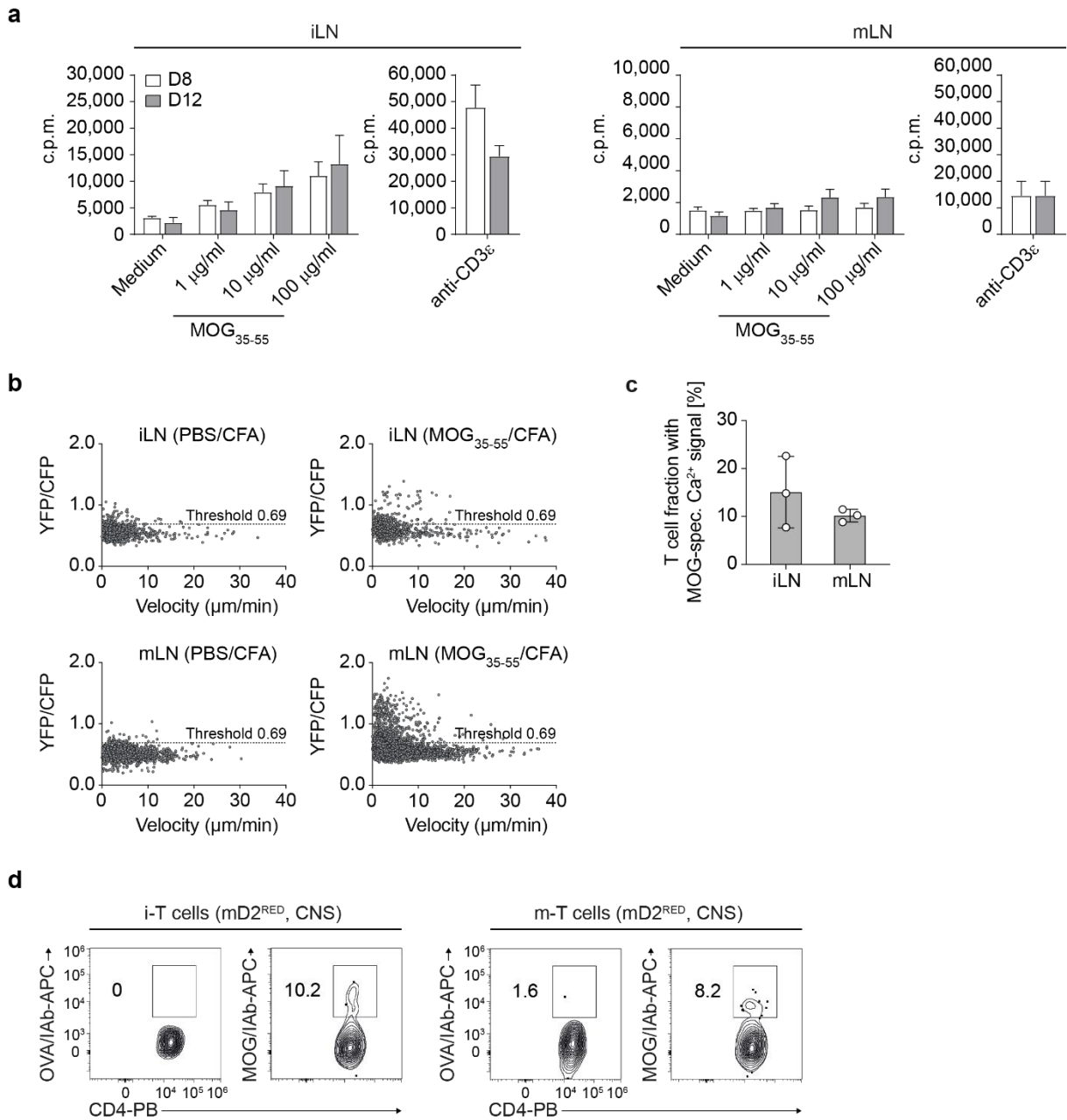


Figure 9: Antigen-specificity of i- and m-T cells during EAE.

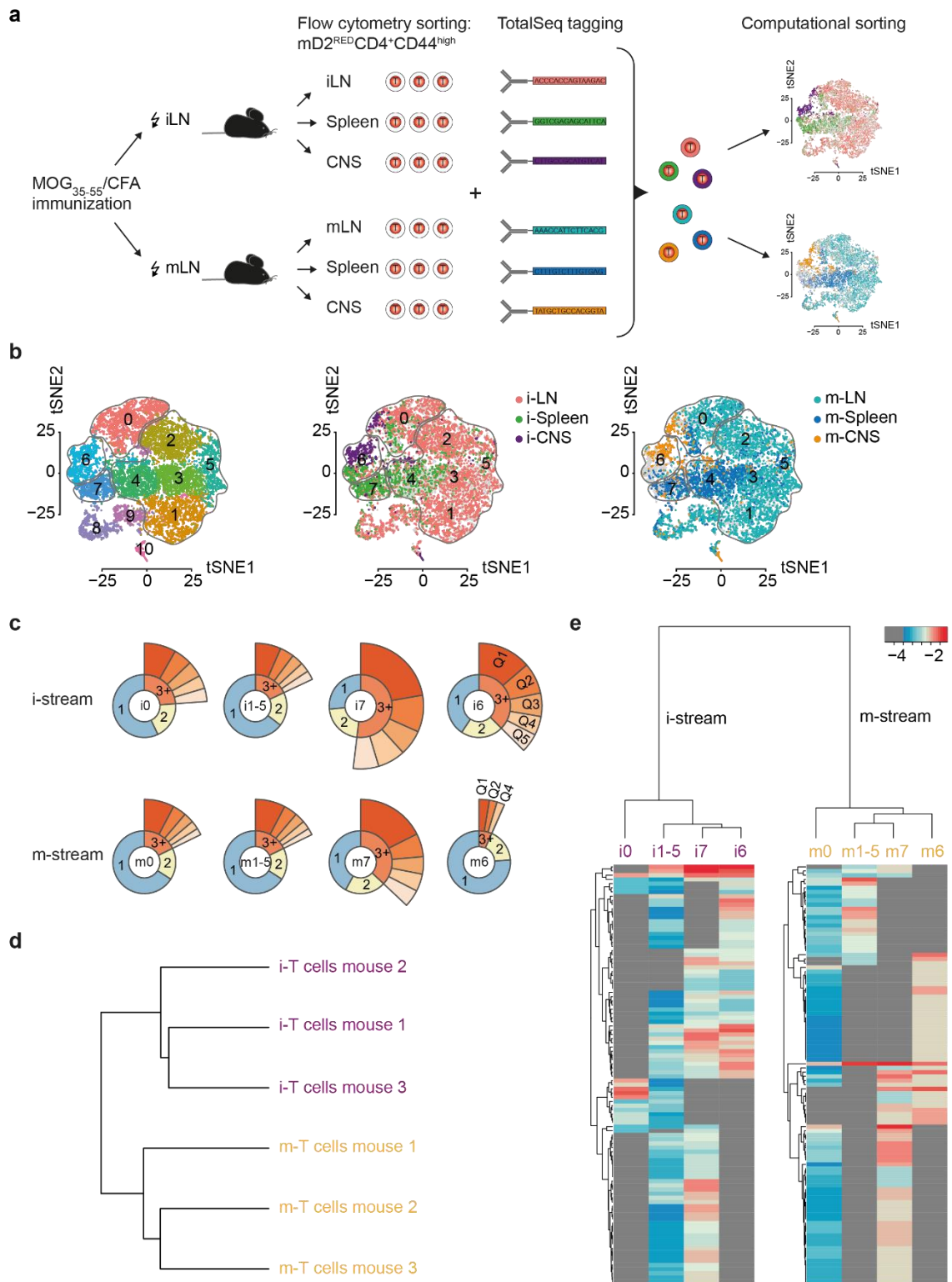
a, ^3H thymidine incorporation assay of inguinal lymph node (iLN; left) or mesenteric lymph node (mLN; right) cells. LNs were isolated at day 8 or day 12 after experimental autoimmune encephalomyelitis (EAE) induction and exposed to MOG(35-55) peptide in the indicated concentrations or anti-CD3 ($0.5 \mu\text{g ml}^{-1}$) for 72 h and pulsed with $1 \mu\text{Ci}$ of ^3H thymidine for the last 16 h. Triplicates of 300,000 cells per mouse from 3 mice. Bars represent mean \pm s.e.m; count per minute (c.p.m) **b**, **c**, Two-photon imaging of TCR^{MOG} Twitch-2B T cells in iLN and mLN analyzed on days 3 or 4 post transfer. Recipient mice were immunized with PBS/CFA or MOG(35-55)/CFA 10 days prior to transfer. Velocity versus Ca^{2+} -indicator ratio (YFP/CFP) is shown (**b**). Mean T cell fractions of MOG-specific Ca^{2+} cells in iLN and mLN (MOG/CFA - PBS/CFA) \pm s.d. (**c**). 3 mice per group. **d**, Flow cytometry analysis of photoconverted (mD2^{RED}) T cells in the central nervous system (CNS) in PhAM^T EAE mice regarding their IAb-MOG or IAb-OVA tetramer binding. The contour plots show day 2 after irradiation at disease onset and were pre-gated on $\text{mD2}^{\text{RED}}\text{CD4}^+$ cells and excluded cell debris, doublets, dead cells, and $\text{CD8}\alpha^+$ cells. Representative plots of 3 pooled PhAM^T mice per group and 2 independent experiments.

6.6 Clonal expansion of i- and m-T cells

To characterize i- and m-T cells further, we used single cell sequencing to analyze their transcriptome (scRNA-seq) and their TCR repertoire (scTCR-seq). For this purpose, mD2^{RED}CD4⁺CD44^{high} T cells were sorted from the irradiated LN, the spleen, and the CNS of immunized PhAM^T mice. The cells were tagged with DNA-conjugated antibodies to multiplex samples (called cell hashing) to avoid batch effects (Figure 10a). Library preparations for scRNA-seq in Figure 10, Figure 11, Figure 12, and Figure 13 were performed by Sebastian Jarosch and scRNA-seq data was analyzed by Eduardo Beltrán.

Unsupervised clustering of the combined scRNA-seq dataset (i- and m-T cells) identified 11 clusters (Figure 10b). Single T cells were grouped according to *FindMarkers* function in the Seurat R package. Clusters 1-5 were combined into a single cluster because none of the “cluster markers” had a log fold change (FC) value higher than 1. At least 8 of the highest expressed markers had a log FC higher than 1 for all other clusters. In addition, T cells in cluster 8 and 9 were removed from the analysis due to high levels of cell cycle genes and cluster 10 T cells were excluded due to low TCR gene expression. Cluster 1, 2, 3, and 5 were mainly comprised of T cells from the LNs, Cluster 4 and 7 of cells from the spleen, and cluster 6 of T cells from the CNS. In comparison, cluster 0 was comprised of T cells from all three organs and resembled the transcriptional profile of Treg cells.

Clonal expansion based on the detection of the same TCR in multiple cells could be observed in all clusters (Figure 10c). However, more highly expanded T cell clones (same TCR found 3 times or more) in cluster 6 (dominantly CNS cells) could be detected in the i-stream (iLN-irradiation group) as compared to the m-stream (mLN-irradiation group). Looking at the clonal relationship between all mice, hierarchical clustering of CDR3 sequences was performed, which showed closest relations between mice of the same stream with no clear overlap between mice of different streams (Figure 10d). In the i-stream, clonotypes from cluster 6 and 7 showed the closest relation, whereas in the m-stream there was a closer relation between cluster 1-5 and cluster 7 (Figure 10e). However, cluster 0, which contained cells of all tissues, contained more related m-T cell clones than i-T cell clones.



Looking at the T cell receptor β -chain variable (TRBV) families, *Trbv5*, *Trbv12*, *Trbv19*, and *Trbv20* were enriched in cluster 6 and 7 (Figure 11a, red dots), which were mainly comprised of CNS and spleen cells, respectively. In addition, *Trbv3* was most abundant in cluster 0 (Figure 11a, green dot). Interestingly, the top differentially expressed genes in cluster 0 compared to cluster 6 and 7 were immune regulatory genes (e.g. *Foxp3*, *Ikzf2*, *Ctla4*, and *Gitr* (*Tnfrsf18*)) (Figure 11b), suggesting that certain TRBV families could be linked to specific immunological functions of T cells, like regulation or effector function.

In summary, expanded T cell clones could be identified in both i- and m-stream across different organs without relevant crossover between streams.

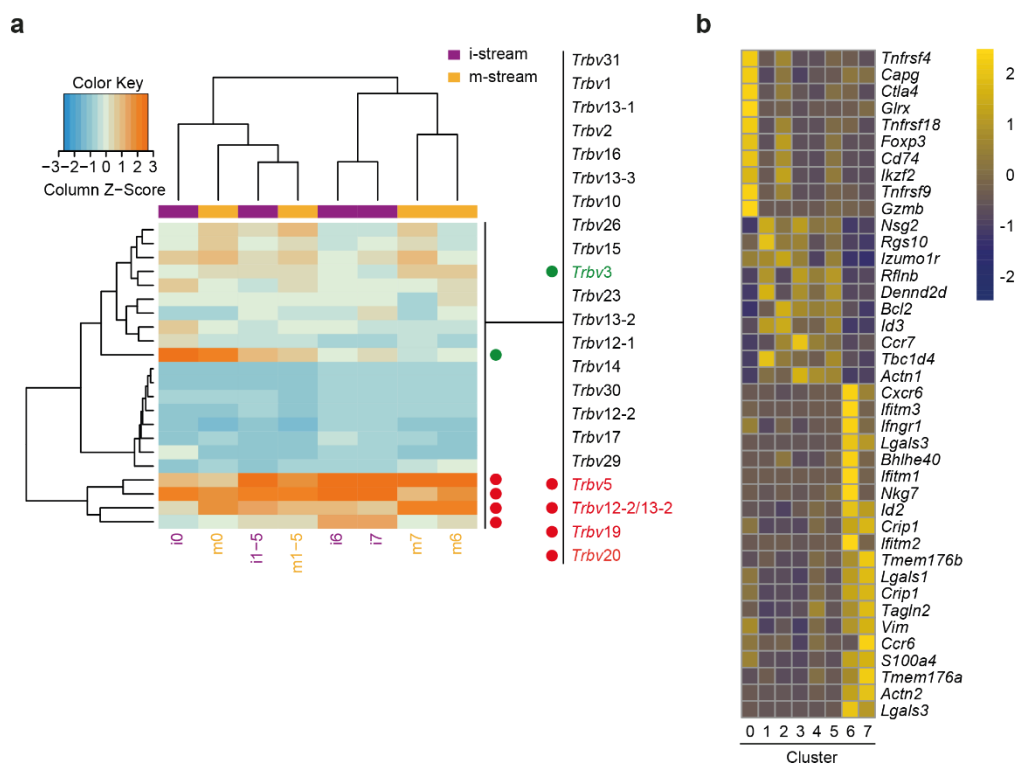


Figure 11: Clonotype analysis of i- and m-T cells during EAE.

a, Heat map of *Trbv* gene families per cluster of both streams was generated with VDJtools. Variable segment usage was used for clustering and hierarchical clustering was performed using Euclidean distance based on weighted variable usage profiles. 3 PhAM^T mice per group. **b**, Average gene expression of the TOP10 differentially expressed genes for all single mD2^{RED}CD4⁺CD44^{high} T cells per cluster. 5 PhAM^T mice per group.

6.7 i- and m-T cells show a distinct phenotype

Both Th1 and Th17 cells have been implicated in CNS autoimmunity (Fletcher et al., 2010; Hiltensperger and Korn, 2018; Korn et al., 2009; Korn and Kallies, 2017). There is a multitude of studies about these subsets in the context of MS and EAE that elucidated different functions and characteristics in mice and humans. For example, Th1 cells have been shown to preferentially infiltrate into the spinal cord during EAE, whereas Th17 cells infiltrate into the

brain (Rothhammer et al., 2011). To compare the phenotype of i- and m- T cells, we performed another scRNA-seq experiment, that was based on the 10x Genomics 3' technology which detects more genes per cell compared to the 5' approach (see experimental setup in Figure 10a).

Unsupervised clustering t-distributed stochastic neighbour embedding (tSNE) of all sorted T cells identified 10 clusters (Figure 12a). i-CNS and m-CNS T cells clustered apart from the peripheral T cells, forming cluster 5 and 9. Despite the separation of the CNS T cells from the peripheral cells, i-CNS T cells were part of cluster 5 and 9, while the majority of m-CNS T cells belonged to cluster 5 (Figure 12b). Overlaying classical Th and Treg gene signatures onto the t-SNE plot did not reveal a clear overlap of these gene signatures with the clustering (Figure 12c). Yet, a heat map representation of Th and Treg signature genes in i- and m- T cells from spleen and CNS showed an overexpression of Th1 signature genes in i-T cells (Figure 12d). However, overexpression of Th17 signature genes were mixed in both i- and m-T cells. To address this in more detail, the PhAM^{flxed} strain was crossed with an IL-17A-Cre driver strain to create a fate map reporter mouse for Th17 cells, termed PhAM^{IL-17}. IL-17A-producers, either present or historic, are labeled by mD2 that can be photoconverted to track these cells. In line with the mixed Th17 signature gene expression in both i- and m-T cells in PhAM^T mice, Th17 cells in PhAM^{IL-17} mice were primed both in their respective irradiated LN (iLN or mLN) and trafficked through the spleen into the CNS (Figure 12e).

These findings suggested that i- and m-T cells in the CNS are phenotypically distinct and that their priming site was a determinant of this difference. Moreover, both i-CNS and m-CNS T cells had mixed phenotypes that did not match with a specific Th cell subset.

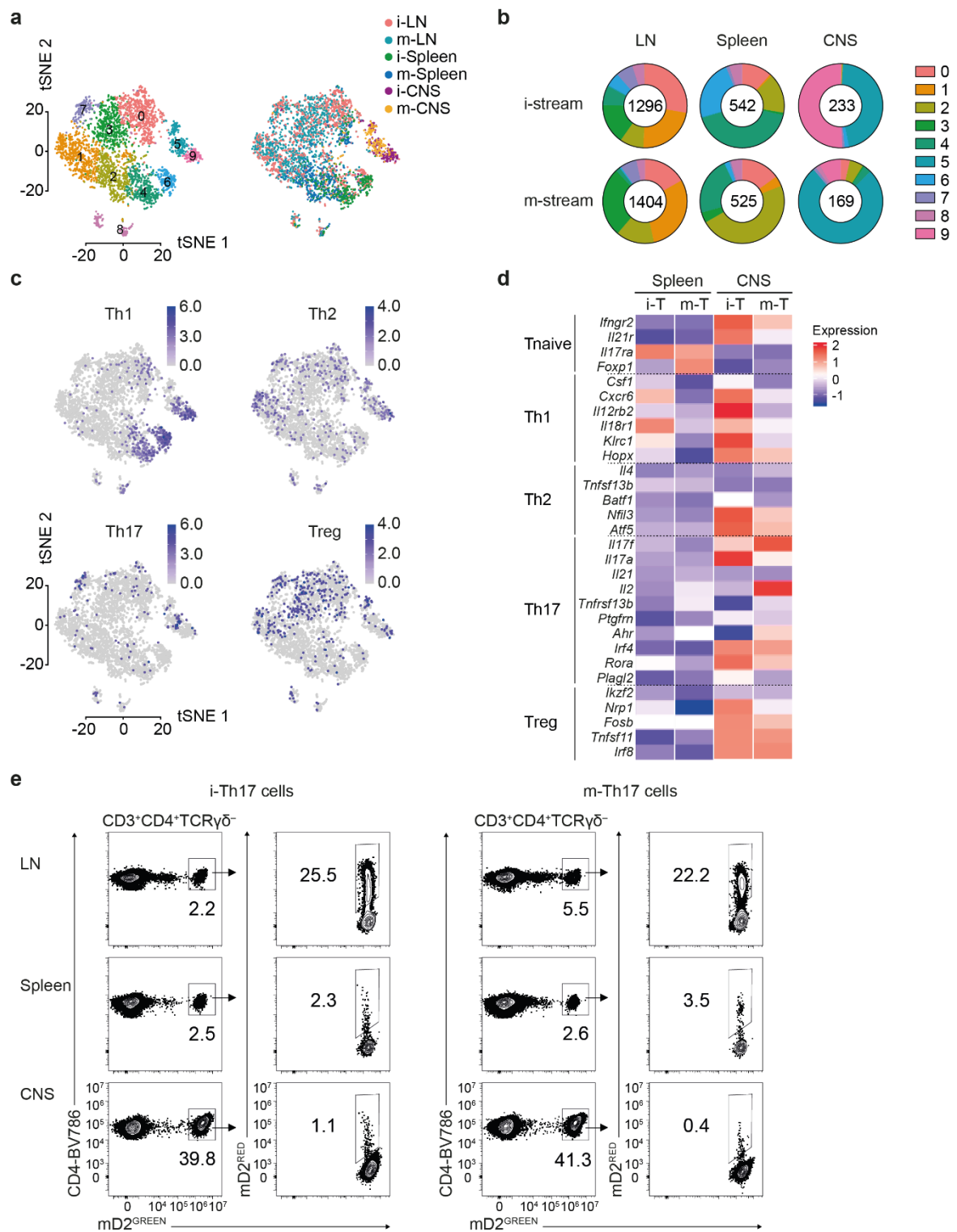


Figure 12: Phenotyping of i- and m-T cells during EAE.

a, Unsupervised clustering t-distributed stochastic neighbour embedding (t-SNE) plot of all single mD2^{RED}CD4⁺CD44^{high} T cells colored according to the cell cluster (left) or i- and m-stream (right) (see experimental setup in Figure 10a). 2 PhAM^T mice per group and a total of 4,169 cells. **b**, Distribution of clusters by tissue and stream. The total cell number per tissue is indicated. **c**, T helper (Th) signature scores based on the expression of key genes. Th1 (553 cells), at least 3 genes out of *Csf1*, *Cxcr6*, *Il12rb2*, *Il18r1*, *Klrc1*, and *Hopx*; Th2 (389 cells), at least 2 genes out of *Il4*, *Tnfrsf13b*, *Batf1*, *Nfil3*, and *Atf5*; Th17 (127 cells), at least 4 genes out of *Il17f*, *Il17a*, *Il21*, *Il2*, *Tnfrsf13b*, *Ptgfrn*, *Ahr*, *Irf4*, *Rora*, and *Plagl2*; Treg (373 cells), at least 3 genes out of *Ikzf2*, *Nrp1*, *Fosb*, *Tnfrsf11*, and *Irf8*. **d**, Average gene expression of Th and Treg signature genes in i- and m-T cells from spleen and CNS. **e**, Flow cytometry analysis of iLN-labeled (left) and mLN-labeled (right) PhAM^{L-17} EAE mice in different tissues regarding the mD2^{RED} frequencies in the mD2^{GREEN} compartment. The contour plots show day 2 after irradiation at disease onset and were pre-gated on CD3⁺CD4⁺TCR $\gamma\delta$ ⁻ cells and excluded cell debris, doublets, and dead cells. Representative plots of 3 PhAM^{L-17} mice per group.

6.8 Imprinting of a specific core signature is based on the priming site

i-T cells and m-T cells could not be defined as either Th1 or Th17 cells but were comprised of a mixed phenotype. Therefore, we tried to elucidate if both groups had their own core gene signature by identifying genes that were either upregulated in i-T cells or in m-T cells of the 3' scRNA-seq data set for all organs (Figure 13a).

Comparing each organ from the i-stream and m-stream with each other (e.g. i-CNS versus m-CNS, etc.) identified 94 genes for the i-T cell core signature and 50 genes for the m-T cell core signature, which were uniquely upregulated in the respective stream (Figure 13b; analysis was performed by Helena Domínguez Moreno). The expression of these signature genes was averaged per sample and visualized as heat maps (Figure 13c, d). Prominent examples for the i-stream were costimulatory molecules like *Icos* and *Cd2*, cytokine receptors like *Il1r1* and *Il18r1*, transcription factors like *Rora* and *Runx2*, chemokine receptors like *Cxcr6* and integrins like *Itgb1* (Figure 13c). For the m-stream, transcription factors like *Ahr*, genes that are implicated in T cell activation and differentiation like *Malt1*, genes implicated in metabolic activities like *P2rx7*, and integrins like *Itga4* were upregulated (Figure 13d). Expression of key i-stream (*Cxcr6* and *Itgb1*) and m-stream (*P2rx7* and *Itga4*) genes in the spleen (Figure 13e) and CNS (Figure 13f) were shown on the single cell level.

To summarize, i-T cells and m-T cells acquired their own core signatures based on their respective priming site in the iLN or mLN.

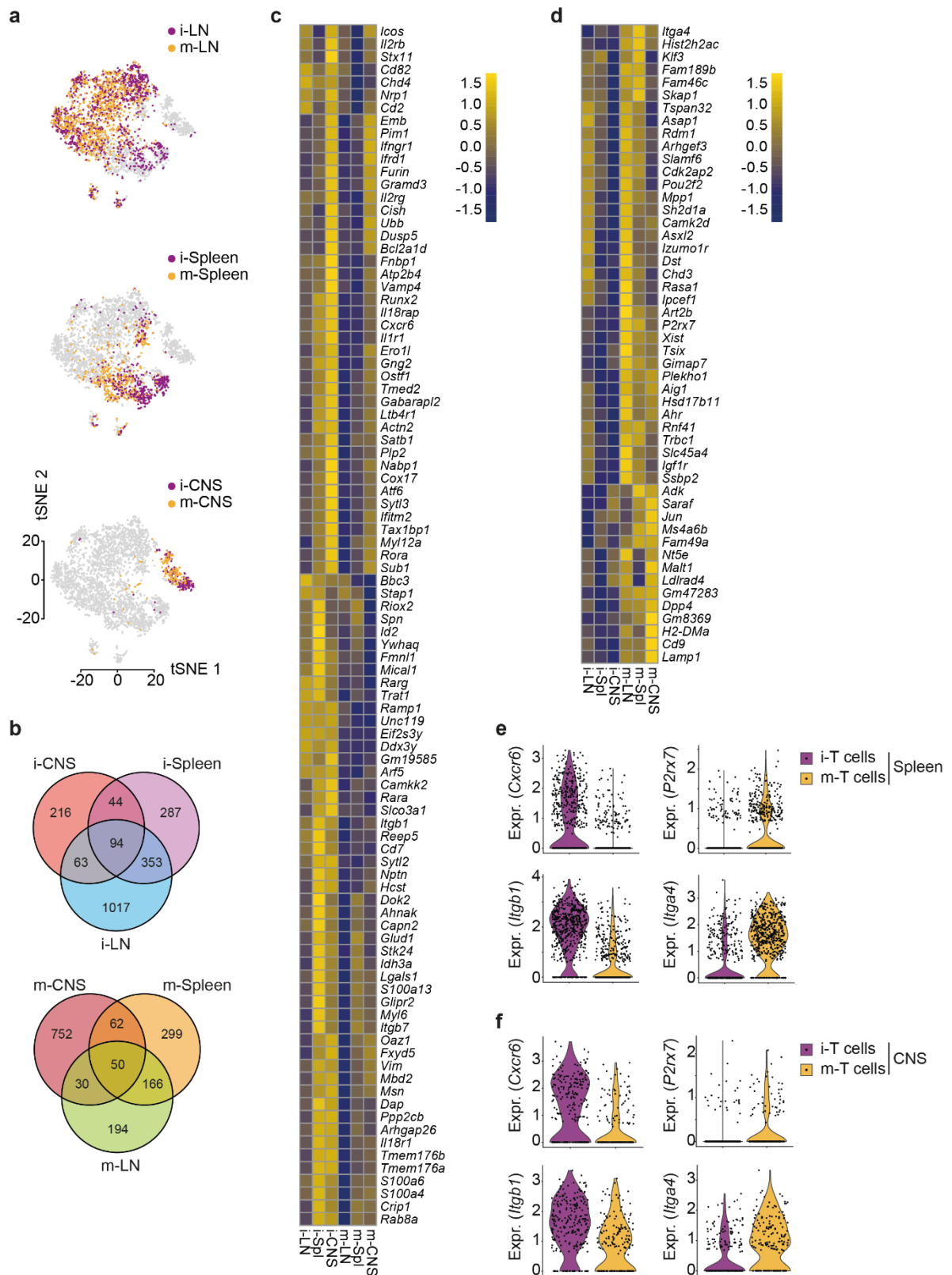


Figure 13: Core gene signatures of i- and m-T cells during EAE.

a, Unsupervised clustering t-distributed stochastic neighbour embedding (t-SNE) plot of all single mD2^{RED}CD4⁺CD44^{high} T cells from Figure 12a colored according to the irradiated lymph node (top), the spleen (middle), and the CNS (bottom) for the i- and m-stream. 2 PhAM^T mice per group and a total of 4,169 cells. **b**, Venn diagrams of the core gene sets from differentially expressed genes in all three tissues with P-value < 0.05 for the i-stream (top) versus the m-stream (bottom). Two-sided Wilcoxon rank-sum test. **c**, **d**, Average gene expression of the 94 core signature genes for the i-stream (**c**) and the 50 core signature genes for the m-stream (**d**) per tissue. **e**, **f**, Gene expression of i-T cell (left) and m-T cell (right) specific genes in the spleen (**e**) or in the CNS (**f**) on the single cell level.

6.9 i- and m-T cells show differential transcription factor activity

In order to assess the transcriptional landscape of i-T cells and m-T cells and if these differences were evident on the open chromatin level, we performed an assay for transposase-accessible chromatin with sequencing (ATAC-seq) analysis with sorted mD2^{RED}CD4⁺CD44^{high} cells from the spleen of iLN- or mLN-irradiated immunized PhAM^T mice. ATAC-seq is a technique that facilitates the activity of a hyperactive Tn5 transposase to probe for open chromatin regions by inserting sequencing adapters (Buenrostro et al., 2015). ATAC-seq library preparation and analysis in Figure 14a, c, d was performed by Helena Domínguez Moreno and analysis in Figure 14b was performed by Gildas Lepennetier.

Normalized open chromatin peaks were filtered by a 5-fold difference compared to a mouse standard, which was merged from multiple samples to achieve high coverage and was used as background to get rid of supposedly unimportant peaks, and displayed in a volcano plot (Figure 14a). Differentially open chromatin peaks were identified by a 2-fold difference between open chromatin peaks of i-Spleen versus m-Spleen samples (visualized by the dashed lines), differentially upregulated i-CNS (purple) and m-CNS (orange) genes from the scRNA-seq core gene signatures (Figure 13) were highlighted, and a few relevant genes like *Itga4* (m-stream) and *Cxcr6* (i-stream) were labeled (Figure 14a). Filtering for differentially upregulated i- and m-T cell genes that also contained differentially open chromatin reduced the number of core signature genes for i-T cells to 47 and for m-T cells to 18 (Figure 14b). Examples of genes with differentially open chromatin peaks were visualized in the genome browser view and included *Cxcr6*, *Il1r1*, and *Itgb1* for i-T cells and *Itga4*, *Ahr*, and *Nt5e* for m-T cells (Figure 14c). Transcription factors associated with open chromatin peaks in the core signatures of i- and m-T cells were analyzed and their activity scores were assessed with the python library tool Regulatory Genomics Toolbox (Li et al., 2019; Spitz and Furlong, 2012). Transcription factors that are associated with general T cell activation (Tcf7, Maf, Irf4, Prdm1, and Foxo1) had a higher activity score in m-T cells, while transcription factors that are associated with specific T cell effector functions (Crem, JunB, T-bet, and ROR γ t) were higher in i-T cells (Figure 14d).

Taken together, the ATAC-seq analysis of splenic i-T cells and m-T cells supported our scRNA-seq analysis and our hypothesis that i- and m-T cells might form distinct T cell subsets.

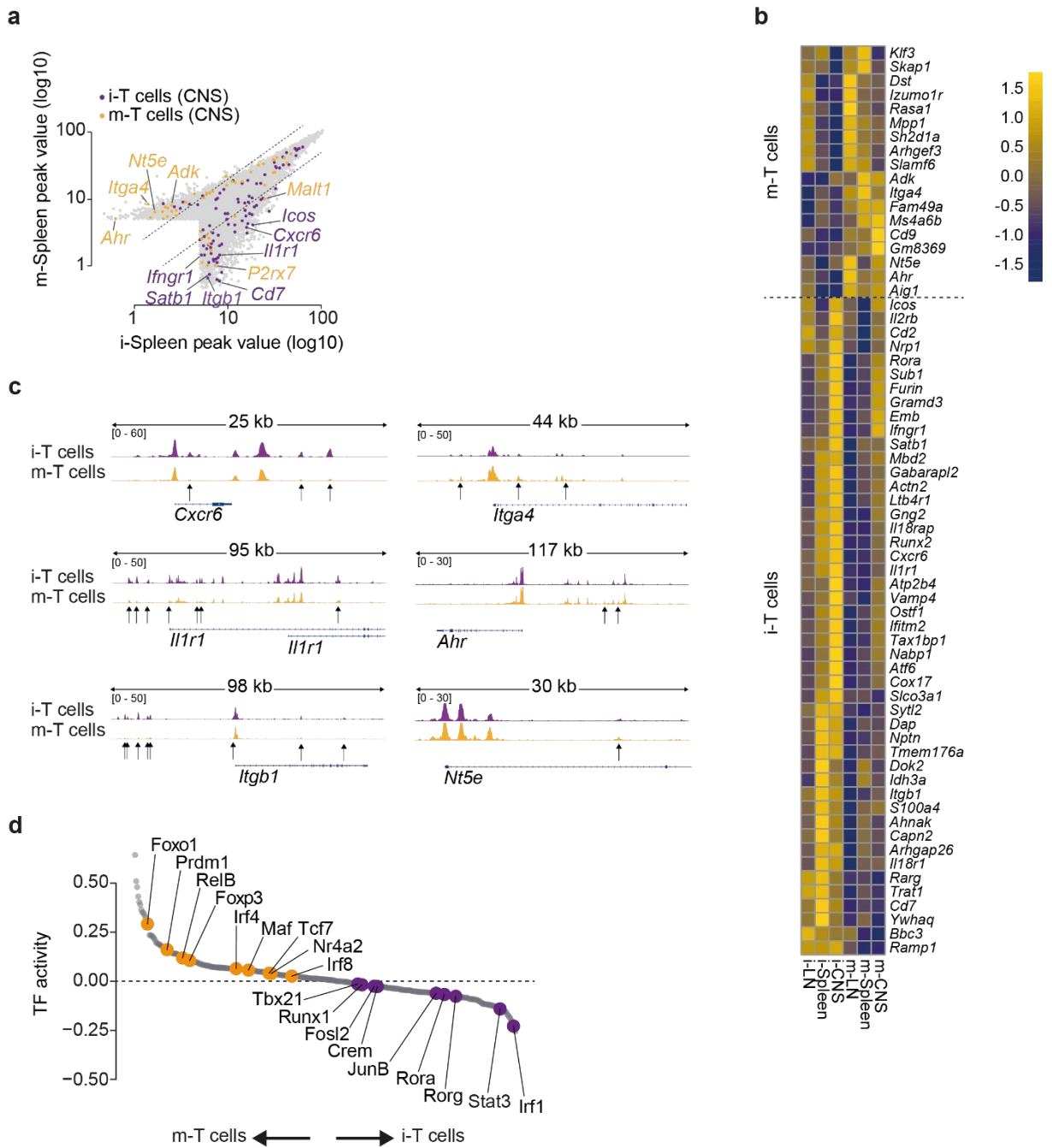


Figure 14: Differentially open chromatin of i- and m-T cells during EAE.

a, Volcano plot representation of normalized ATAC peaks of mD2^{RED}CD4⁺CD44^{high} T cells from the spleen of iLN- or mLN-irradiated mice at day 2 after irradiation at disease onset. Dashed lines represent 2-fold difference between i- and m-Spleen samples. Peaks with less than 5-fold enrichment over background signal were discarded. Some i-T cell genes (purple) and m-T cell genes (orange) from scRNA-seq data (Figure 13) of the CNS were highlighted. Pool of 2 PhAM^T mice per group. **b**, Average gene expression of the 47 core signature genes for the i-stream (bottom) and the 18 core signature genes for the m-stream (top) that contain differentially expressed genes and differentially open chromatin. **c**, Genome browser view of specific i- and m-T cell genes with differentially open chromatin shown in **a**. Tracks correspond to ATAC peaks for i-T cells (purple) and m-T cells (orange). Differential peaks are highlighted with arrows. **d**, Waterfall plot representation of transcription factor activity. Transcription factor activity scores are assessed with Regulatory Genomics Toolbox for i- and m-T cell signature genes with differentially open chromatin from **b**, ranked by activity score. Differences in the transcription factor dynamics between the two conditions are shown on the y axis and the position of the transcription factors based on the ranking are shown on the x axis.

6.10 i- and m-T cell gene signatures are robust in alternative models

One characteristic of the EAE model that was used throughout the thesis (Figure 6a), is that iLNs are primary draining LNs due to subcutaneous injection of MOG₃₅₋₅₅ peptide in CFA at the base of tail. Consequently, there was a bias in regard to the antigen dose and adjuvant exposure in iLN versus mLN in this system that could be responsible for the observed findings. To address these concerns, I used different immunization regimens, other routes of antigen delivery, and even a spontaneous mouse model for EAE.

First, the PhAM^T mouse line was used to induce EAE regularly at the base of tail subcutaneously and the chemokine surface marker Cxcr6 as an i-T cell marker, the purinergic receptor P2rx7 as an m-T cell marker, and the integrins α 4 (CD49d) and β 1 (CD29) were used as a readout by flow cytometry (Figure 15a, left column). Next, the site of immunization was changed to the neck (between the shoulder blades) to reduce the antigen and CFA load that reached the iLNs, creating a system in which iLNs and mLNs were stimulated in a more homogenous way (Figure 15a, middle column). To rule out that the differences between i- and m-T cells was dependent on MOG antigen, ovalbumin (OVA(323-339)) peptide was used as an alternative antigen (Figure 15a, right column). Cxcr6 and β 1-integrin expression was universally higher in i-T cells from the spleen of PhAM^T mice, while P2rx7 and α 4-integrin was higher in m-T cells, regardless of the site of immunization or the antigen (Figure 15a).

In an attempt to generate a system that was adjuvant-free and where the antigen dose that reaches the iLNs and mLNs was comparable, MOG(35-55) peptide was injected intravenously into TCR^{MOG} transgenic 2D2 PhAM^T mice (Figure 15b). The iLN or mLN was irradiated two days after peptide injection and i- and m-T cell signature markers were analyzed in the spleen on day four. This intravenous injection system recapitulated the differences that were apparent in the classical EAE model in regard of Cxcr6, P2rx7, and the integrins α 4 and β 1 in the spleen (Figure 15b).

Finally, I used a spontaneous EAE model that is based on a double transgenic TCR^{MOG} and B cell receptor (BCR)^{MOG} background. 2D2 x TH PhAM^T mice develop EAE around 5 weeks of age without injection of antigen or adjuvants. While Cxcr6 was not markedly different between i- and m-T cells in the spleen of 2D2 x TH PhAM^T mice, β 1-integrin was higher in i-T cells, and P2rx7 and α 4-integrin were elevated in m-T cells (Figure 15c), recapitulating the phenotype of i-T cells and m-T cells in the induced EAE model.

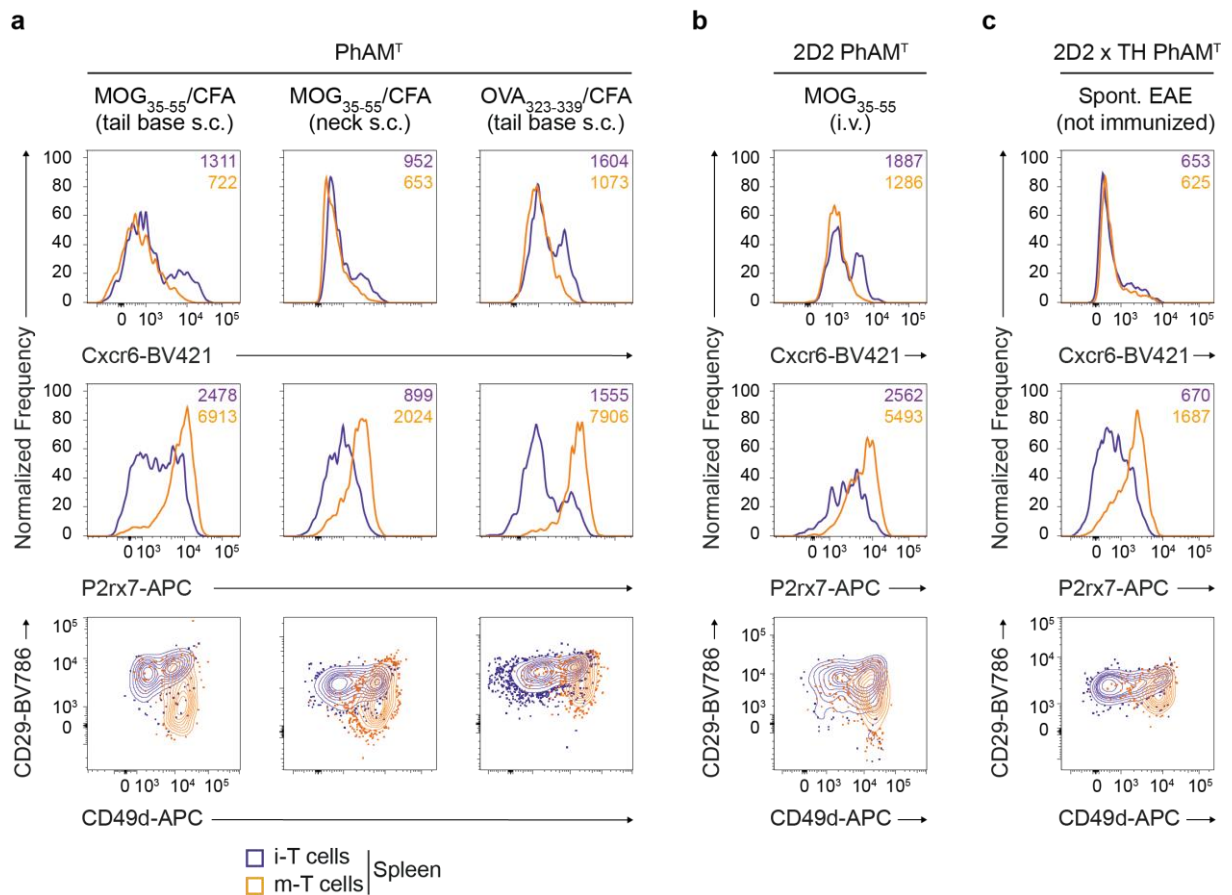


Figure 15: Robust i- and m-T cell signature gene expression in alternative models.

a – c, Flow cytometry analysis of photoconverted (mD2^{RED}) T cells in the spleen of iLN-labeled (purple) and mLN-labeled (orange) immunized PhAM^T (**a**) or 2D2 PhAM^T mice (**b**), and spontaneous 2D2 x TH PhAM^T EAE mice (**c**), regarding their Cxcr6 (top), P2rx7 (middle), and $\alpha 4$ -integrin (CD49d) versus $\beta 1$ -integrin (CD29) (bottom) expression. The histograms and contour plots show day 2 after irradiation at day 11 (**a**) or at day 2 (**b**) after immunization, or day 3 after irradiation at 5 weeks of age (**c**), and were pre-gated on mD2^{RED}CD4⁺CD44^{high} cells and excluded cell debris, doublets, dead cells, and CD8 α ⁺ cells. The 2D2 PhAM^T mice were immunized with 40 μ g of MOG₃₅₋₅₅ i.v. (**b**). Representative plots of 3 PhAM^T mice, 4 2D2 PhAM^T mice, and 4 2D2 x TH PhAM^T mice per group. Numbers indicate mean fluorescent intensities; subcutaneous (s.c.) injection; intravenous (i.v.) injection.

In order to further characterize the transcriptomes of i-T cells and m-T cells in 2D2 x TH PhAM^T mice, i- and m-T cells were sorted from irradiated LNs and spleens of 2D2 x TH PhAM^T mice and subjected to bulk RNA sequencing (RNA-seq) to probe them for i- and m-T cell gene signatures (from Figure 14b). RNA-seq library preparation in Figure 16 was performed by Rupert Öllinger and analysis was performed by Gildas Lepennetier.

Markers like *Itgb1* ($\beta 1$ -integrin) and *Itga4* ($\alpha 4$ -integrin) were highly expressed in i-T cells or m-T cells, respectively (Figure 16a, b). Moreover, gene set enrichment analysis (GSEA) confirmed that the i-T cell core signature was enriched in i-T cells of 2D2 x TH PhAM^T mice, while the m-T cell core signature was enriched in m-T cells both in the irradiated LNs and spleens (Figure 16c).

Taken together, these data supported the notion that the site of priming (iLN versus mLN) was responsible for the distinct transcriptomes in i- and m-T cells, independently of the antigen dose or adjuvants.

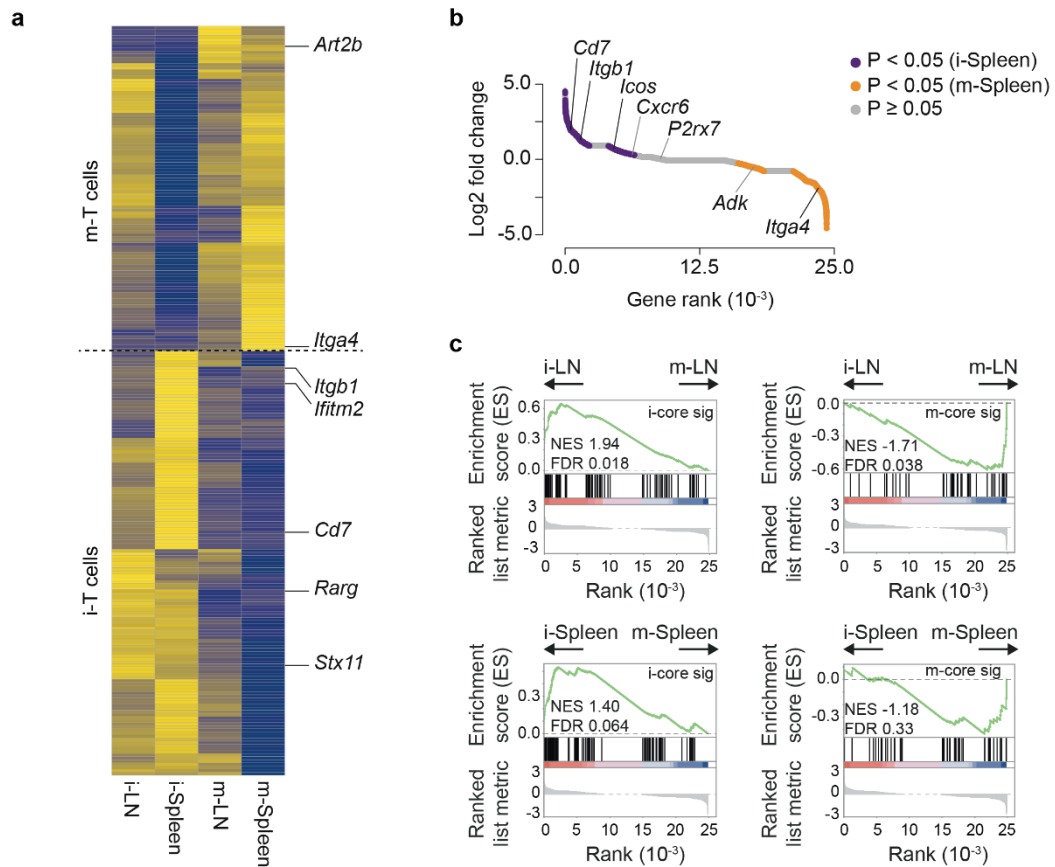


Figure 16: Enrichment of distinct core signatures in i- and m-T cells during spontaneous EAE.

a, Average gene expression of all differentially expressed genes in the RNA-seq data (up and down regulated) in i- and m-T cells isolated from the spleens of 2D2 \times TH PhAM^T mice 3 days after irradiation at 5 weeks of age. Differentially expressed genes ($P < 0.05$) were detected using the Seurat FindMarkers function based on a two-sided Wilcoxon rank-sum test and adjusted by the Bonferroni method. **b**, Waterfall plot representation of genes expressed in i-T cells (purple) versus m-T cells (orange) from the spleens of 2D2 \times TH PhAM^T mice ranked by fold change. Differences in the log2 fold changes between the two conditions are shown on the x axis. Significant genes at $P < 0.05$ are colored. A two-sided Wilcoxon rank-sum test adjusted by the Bonferroni method was used. **c**, GSEA analysis of the i- and m-core gene signatures (from Figure 14b) in RNA-seq data of i- and m-T cells from the lymph nodes (top) and spleens (bottom) of iLN- or mLN-labeled 2D2 \times TH PhAM^T mice. 4 2D2 \times TH PhAM^T mice per group.

6.11 CNS infiltration pattern is distinct in i- and m-T cells

In the scRNA-seq and ATAC-seq data set were i- and m-T cells distinct in their transcriptional and open chromatin profile. Therefore, it was of great interest to elucidate if these two T cell subsets exhibited different functions during CNS autoimmunity. Because the chemokine receptor *Cxcr6* and $\beta 1$ -integrin were part of the i-T cell core signature and $\alpha 4$ -integrin was part of the m-T cell core signature, we first studied the localization of i- and m-T cells in the CNS. Histology analyses in Figure 17a, Figure 18c, and Figure 19a, c were performed by Ravi Kant.

EAE was induced in PhAM^T mice and either the iLN or the largest mLN was irradiated at disease onset and the mice were sacrificed 2 days later as described in Figure 6a. The lumbar spinal cord and the brain stem were analyzed via histology and showed that i-T cells could be detected in the lumbar spinal cord, whereas m-T cells were absent (Figure 17a). Note that the number of i- and m-T cells per section in the brain stem was comparable (Figure 17a) and the

disease course of iLN- and mLN-irradiated animals was similar (Figure 17b). To validate the scRNA-seq data of *Itga4* and *Cxcr6* expression on the protein level in the CNS, *Cxcr6* and CD49d ($\alpha 4$ -integrin) were measured by flow cytometry. The frequencies of $Cxcr6^{+}CD44^{high}$ i-T cells were elevated compared to m-T cells (Figure 17c, left panel), which is in line with the scRNA-seq data for *Cxcr6*. In contrast, the frequencies of $CD49d^{high}CD44^{high}$ m-T cells were higher compared to i-T cells (Figure 17c, right panel), corroborating the scRNA-seq data for *Itga4*.

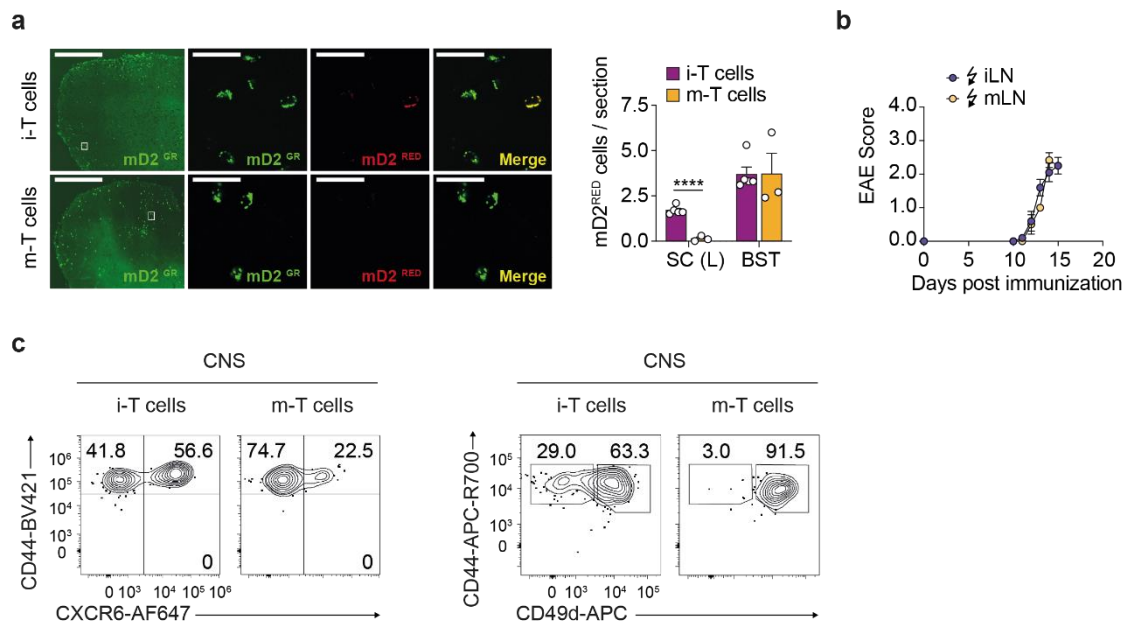


Figure 17: Distinct characteristics of i- and m-T cells in the CNS during EAE.

a, Histology of $mD2^{GREEN}$ ($mD2^{GR}$) and $mD2^{RED}$ T cells in lumbar spinal cord (SC (L)) sections from iLN- (top panel) or mLN-labeled (bottom panel) PhAM^T experimental autoimmune encephalomyelitis (EAE) mice at day 2 after irradiation at disease onset. Scale bars, 500 μm (left) and 20 μm (magnified; middle and right). Bar graphs show data points as mean values of ten sections from SC (L) and brainstem (BST) per mouse from 5 mice for i-T cells and 3 mice for m-T cells. Unpaired two-tailed *t*-test, *****P* = 0.000033. Data are shown as mean + s.e.m. **b**, EAE disease course of iLN- (purple) and mLN-labeled PhAM^T mice (orange) at day 2 after irradiation at disease onset. 5 iLN-labeled and 3 mLN-labeled mice, representative plot from five independent experiments. Data shown as mean \pm s.d. **c**, Flow cytometry analysis of photoconverted ($mD2^{RED}$) T cells in the central nervous system (CNS) in PhAM^T EAE mice regarding their *Cxcr6* (left) and CD49d ($\alpha 4$ -integrin, right) versus CD44 expression. The contour plots show day 2 after irradiation at disease onset and were pre-gated on $mD2^{RED}CD4^{+}$ cells and excluded cell debris, doublets, dead cells, and $CD8\alpha^{+}$ cells. Representative plots of 3 PhAM^T mice per group.

In order to investigate whether the distinct effector functions of i- and m-T cells translated into distinct histological or clinical phenotypes, i-T cells and m-T cells were isolated and separately transferred into secondary hosts. In fact, I adoptively transferred MOG-specific i- or m-T cells from the spleen of 2D2 x PhAM^T mice at day 8 (photoconverted 2 days prior) after immunization into immunization-matched *Rag1*^{-/-} recipients (Figure 18a). 7000 to 12000 transferred i- or m-T cells ($mD2^{RED}CD4^{+}CD44^{high}$) were able to induce EAE in about 50% of *Rag1*^{-/-} recipients (Figure 18b). Looking at the histology of i- and m-T cells in the CNS 2 days after disease onset, the infiltrates were comparable in the brain stem (Figure 18c, top panel). However, m-T cells were predominantly located in the white matter of the brain stem (Figure 18c, top panel, arrowheads) and the cerebellar white matter was exclusively infiltrated by m-T cells but not i-

T cells (Figure 18c, top panel, arrows). Conversely, in the spinal cord i-T cells preferentially infiltrated the grey matter while m-T cells were essentially restricted to the white matter (Figure 18c, middle and bottom panel, quantified in the bar diagram). Importantly, when looking at the stability of the imprinted gene signatures, a key m-T cell marker, CD49d ($\alpha 4$ -integrin), was assessed in the spleen of the recipient mice 2 days after disease onset (Figure 18d). Even after approximately 20 days post transfer, almost all m-T cells were CD44^{high}CD49d^{high} and the majority of i-T cells were CD44^{high}CD49d^{low}, suggesting that the imprinting of i- and m-T cell signatures was stable over many cell divisions (Figure 18d).

In summary, i-T cells and m-T cells were encephalitogenic and showed a different CNS localization pattern that was most evident in their differential white versus grey matter distribution.

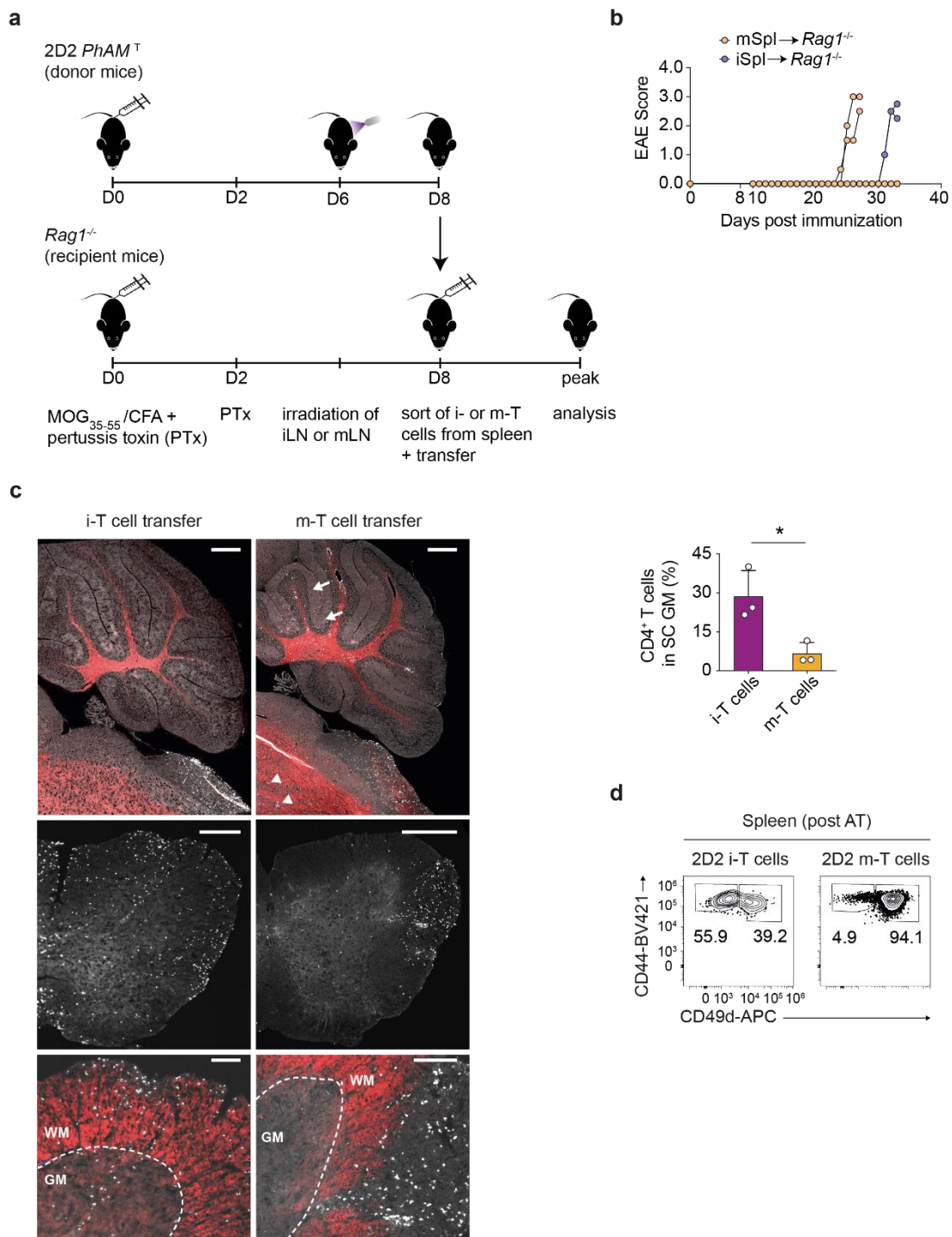


Figure 18: Distinct white versus grey matter distribution of i- and m-T cells in the CNS during EAE.

a, Schematic of adoptive transfer of mD2^{RED}CD4⁺CD44^{high} T cells from the spleen of iLN- or mLN-labeled 2D2 PhAM^T experimental autoimmune encephalomyelitis (EAE) mice 2 days after irradiation at day 6 into immunization-matched Rag1^{-/-} recipient mice. **b**, EAE disease course of adoptive transfer with i- (purple) and m-T cells (orange) from the spleen of 2D2 PhAM^T EAE mice into Rag1^{-/-} recipient mice. Representative plot with 4 mice per group from two independent experiments. Data shown as individual mice. **c**, Histology of transferred TCR^{MOG}mD2^{RED}CD4⁺CD44^{high} i- and m-T cells in the brainstem and cerebellum (top), and the lumbar spinal cord (middle and bottom) in regard to white matter (WM) and grey matter (GM) localization. Scale bars, 500 μm (top and middle) and 100 μm (bottom). Bar graphs show quantification of GM frequencies of i- and m-T cells per lumbar spinal cord (SC) section in 3 mice per group. Unpaired two-tailed *t*-test, **P* = 0.046. Data are shown as mean + s.d. **d**, Flow cytometry analysis of transferred TCR^{MOG}mD2^{RED}CD4⁺CD44^{high} i- and m-T cells in the spleen of Rag1^{-/-} recipients in regard to CD49d (α4-integrin) versus CD44 expression. The contour plots show day 2 after disease onset (approximately 20 days after transfer) and were pre-gated on mD2^{GREEN}CD4⁺ cells and excluded cell debris, doublets, dead cells, and CD8α⁺ cells. Representative plots of 3 mice per group. Adoptive transfer (AT).

6.12 CNS infiltration pattern of m-T cells resembles *Cxcr6*^{-/-} T cells

Due to the difference in white versus grey matter distribution and the reduced expression of *Cxcr6* in m-T cells, I investigated whether *Cxcr6* could be a determinant of this differential infiltration behavior of i- versus m-T cells. For this purpose, I induced EAE in *Cxcr6*^{-/-} mice and analyzed the distribution of encephalitogenic T cells in the CNS.

Immunized *Cxcr6*^{-/-} mice were sacrificed and the lumbar spinal cord was analyzed by histology. Interestingly, CD4⁺ T cells in *Cxcr6*^{-/-} mice predominantly infiltrated the white matter whereas CD4⁺ T cells in wild-type (WT) mice infiltrated white and grey matter (Figure 19a). This finding was comparable to TCR^{MOG} m-T cells in secondary *Rag1*^{-/-} hosts (Figure 18c). Consistent with the infiltration pattern in the spinal cord, CD4⁺ T cell infiltrates could be observed in the cerebellar white matter in *Cxcr6*^{-/-} mice that were absent in WT EAE mice (Figure 19c). Of note, the disease course of WT and *Cxcr6*^{-/-} mice was comparable (Figure 19b).

Since *Cxcr6*^{-/-} T cells showed a similar behavior as m-T cells in terms of white matter infiltration, these findings suggested that *Cxcr6* might contribute to the targeting of i-T cells (which were expressing *Cxcr6*) to the grey matter, and that the differential expression of guidance molecules in i-T cells versus m-T cells might be responsible for their different white and grey matter localization pattern.

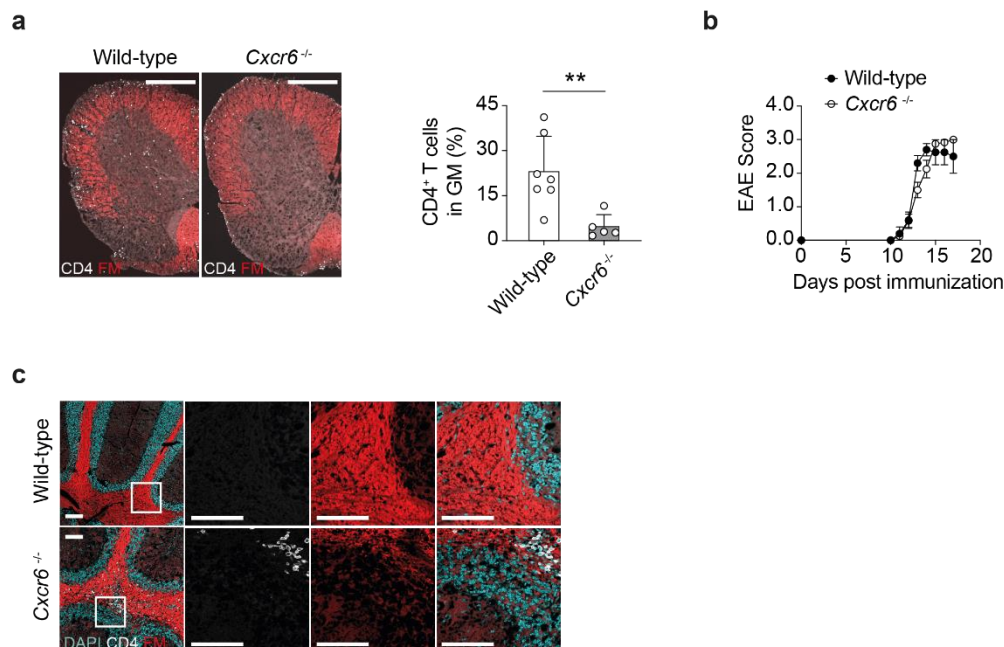


Figure 19: Recapitulation of distinct white matter localization of m-T cells in *Cxcr6*^{-/-} T cells during EAE.

a, Histology of CD4⁺ T cells in the lumbar spinal cord from wild-type (WT) and *Cxcr6*^{-/-} mice in regard to white matter (WM) and grey matter (GM) localization. Scale bars, 500 μ m. Bar graphs show quantification of GM frequencies of T cells per lumbar spinal cord section in 7 WT mice and 5 *Cxcr6*^{-/-} mice. Unpaired two-tailed *t*-test, ***P* = 0.0055. FM, FluoroMyelin Red. Data are shown as mean + s.d. **b**, Experimental autoimmune encephalomyelitis (EAE) disease course of WT and *Cxcr6*^{-/-} EAE mice. 5 WT mice and 6 *Cxcr6*^{-/-} mice, representative plot from three independent experiments. Data are shown as mean \pm s.d. **c**, Histology of CD4⁺ T cells in the cerebellum from WT and *Cxcr6*^{-/-} mice in regard to WM and GM localization. Scale bars, 100 μ m. 3 mice per group.

7 Discussion

Historically T helper (Th) cell subsets have been divided into Th1, Th2, – and later – Th17, based on their cytokine profile and transcription factor expression (Figure 1) as well as their effector function. However, this concept lacks consistency *in vivo*, especially in humans where T cells are multifunctional and have a heterogenic cytokine expression profile (Becattini et al., 2015). Here, I developed a provenance mapping system to interrogate whether the priming site of T cells could be a determinant of a stable portfolio of effector functions in remote organs to allow for a provenance-based classification of Th cells that could be linked to a specific type of immunopathology in the central nervous system (CNS).

7.1 The PhAM^T mouse line for provenance-guided study of T cells

The PhAM^T mouse line was chosen as a provenance mapping system for T cells that were either primed in the skin-draining inguinal lymph nodes (iLN) or the gut-draining mesenteric lymph nodes (mLN) (Figure 5a). Targeting of the photoconvertible protein Dendra2 to the mitochondria (mito-Dendra2, mD2) allowed for higher half-life compared to cytoplasmic localization and was mostly limited by cell divisions. In fact, photoconverted T cells in the iLN retained their mD2^{RED} signal over 2 days during steady in the presence of FTY720, that blocks lymphocyte egress out of LNs (Figure 5b). Early *in vitro* experiments showed no imminent cell toxicity in response to the irradiation with high intensity violet light (405nm, 60mW output) (Figure 4b, d). To validate this *in vivo*, I irradiated the iLN in FTY720-treated animals during steady state and experimental autoimmune encephalomyelitis (EAE) and analyzed the frequencies of naïve (CD62L^{high}CD44^{int}) and effector (CD62L^{int}CD44^{high}) T conventional (Tcon; CD4⁺Foxp3⁻) cells, and T regulatory (Treg; CD4⁺Foxp3⁺) cells over time. Since naïve Tcon cells are more sensitive to cytotoxicity from irradiation compared to Treg cells, any changes in their frequencies could be – at least in part – based on irradiation-induced cytotoxicity during photoconversion (Kachikwu et al., 2011). While there was an accumulation of effector Tcon cells and Treg cells in the irradiated LN as well as a reduction of naïve T cells in untreated animals, there was no change in frequencies of any of these subsets in FTY720-treated animals and the frequencies were comparable to non-irradiated LNs (Figure 5c-f). This supports the notion that the irradiation protocol is not inducing cytotoxicity, since it did not have an impact on the more photosensitive naïve T cell population.

Because photoconverted T cells (CD4⁺mD2^{RED}) retained their mD2^{RED} signal for up to 5 cell divisions (Figure 4c), the timeframe to label and track a T cell in an inflammatory setting, like EAE, is limited. Since *in vitro*-activated CD4⁺ T cells with anti-CD3/CD28 still retained a high mD2^{RED} signal after 2 days of irradiation (Figure 4b), I chose this duration for our EAE experiments initially and were able to find labeled T cells in the spleen and even the CNS on the day of analysis. The rationale why I chose EAE onset (a disease score of 1, approximately

day 11-13 after immunization) for the time point of photoconversion (Figure 6a) was two-fold. First, due to the oily antigen depot in myelin oligodendrocyte glycoprotein (MOG)-induced EAE, priming of T cells is ongoing for an extended period of time, and even at the onset of clinical symptoms, priming will still be maintained in peripheral lymph nodes (LNs). Second, by selecting the first onset of clinical symptoms, I was able to "synchronize" my read-out across studies and also control for the relative amount of inflammation since mice that showed first symptoms of disease would very likely go on to develop full-blown EAE. Notably, when I photoconverted T cells pre-onset in previous experiments, labelled T cells could not be detected in the CNS and only very few T cells were present overall. Therefore, in order to study inguinal derived (i)-T cells and mesenteric-derived (m)-T cells in the CNS, labeling of T cells in different LN stations at the onset of clinical signs of EAE was the appropriate set-up.

7.2 iLN and mLN are unique priming sites for CNS-infiltrating T cells

To study the impact of the priming site (gut versus skin-draining LNs) on the T cell phenotype in the context of CNS autoimmunity, I first had to decipher how much cross-trafficking of antigen-experienced T cells takes place between iLNs and mLNs during EAE. Hypothetically, if mLNs would be a station for iLN-primed effector T cells on their way to the CNS, it would be impossible to distinguish antigen-experienced mLN-primed T cells by photoconversion from iLN-primed effector T cells that trafficked to the mLNs and vice versa. Thus, I performed a series of experiments that allowed me to conclude that only negligible amounts of antigen-experienced T cells migrated between these two LN stations upon labeling at disease onset (as was done for most experiments in this study) (Figure 6) as well as earlier time points (Figure 7). This suggests that iLNs and mLNs are unique priming sites for CNS-infiltrating effector T cells in the periphery during EAE (Figure 20).

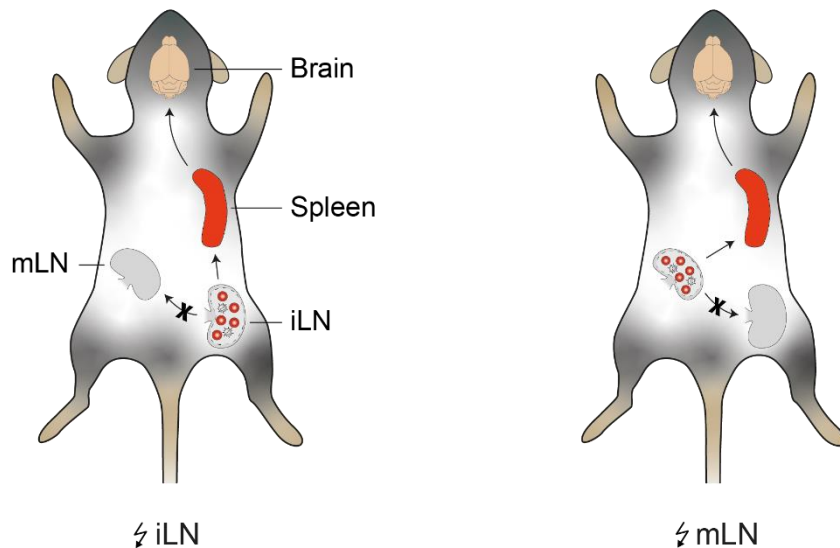


Figure 20: Potential routes of i- and m-T cells during EAE.

Schematic of primed i- and m-T cells on their way to the central nervous system (CNS) during experimental autoimmune encephalomyelitis (EAE). The experimental setup is described in Figure 6a. Irradiation is depicted as lightning symbol; inguinal lymph node (iLN); mesenteric lymph node (mLN).

Next, I examined if there is indeed MOG-specific priming taking place in both LN stations. Since iLNs are the primary draining LNs in our EAE model due to the tail-based application route of antigen and adjuvants, I needed to show that antigen-specific priming also occurs in mLNs. Indeed both antigen-specific recall experiments (Figure 9a) and *in vivo* imaging of TCR^{MOG} transgenic T cells (2D2) in iLNs and mLNs (performed by Isabel J. Bauer and Naoto Kawakami) (Figure 9b,c) indicated that antigen-specific priming also occurred in mLNs. This might be due to systemic antigen spreading at later time points after immunization as has been shown for subcutaneous protein administration (Kijanka et al., 2014).

Moreover, i- and m-T cells shared the same T cell receptor β -chain variable (TRBV) families (Figure 11a), which suggests that they might recognize similar antigens and is line with the fact that some of the enriched families have been associated with MOG-reactivity (Alli et al., 2008; Nguyen et al., 2010). This was corroborated by the notion that both i- and m-T cells isolated from the CNS bound to IAb-MOG tetramers (Figure 9d), indicating that there are indeed MOG-specific i- and m-T cells that infiltrated the CNS. Of note, no clear statement can be made about T cells that do not bind to the tetramer regarding their specificity to MOG antigen, since low affinity TCRs may not be picked up by the tetramer (which is a particular problem when used to stain self-specific TCRs) (Laugel et al., 2007; Sabatino et al., 2011). In addition, antigen-unspecific bystander T cells have been reported to contribute to the immunopathology in the CNS (Lee et al., 2019). This could mean that their functional phenotype (e.g. as defined by the site of their origin (iLN versus mLN)) may well be a crucial determinant of the amount and quality of the immunopathology in the target tissue.

Despite the overlap of the same TRBV families between i- and m-T cells, the lack of public clones between both streams supported the hypothesis of distinct streams from the iLN and mLN through the spleen to the CNS, respectively, without relevant cross-over between streams.

7.3 i- and m-T cells constitute distinct T cell subsets during EAE

To explain the current heterogeneity of Th subset *in vivo*, there is a debate about the stability and the extent of plasticity of Th subsets. The stability of Th-specific transcription factor expression is regulated by positive and negative feedback loops that induce the expression of a certain transcription factor and suppress the expression of the alternative transcription factors (Ivanova and Orekhov, 2015). Th1 (T-bet and IFN- γ) and Th2 (GATA-3 and IL-4) cell subsets are prime examples for this kind of regulation, which is the reason why these subsets are considered most stable (Murphy and Stockinger, 2010). Another kind of regulation is epigenetic control of transcription factor and cytokine gene loci by chromatin modifications, which has been shown to play an important role in T cell differentiation and plasticity, in particular in the Th17 cell lineage (Hirahara et al., 2011; Mukasa et al., 2010).

In addition, the site of priming has been linked with the imprinting of T cell features, specifically in the context of tissue-selective lymphocyte trafficking (Sigmundsdottir and Butcher, 2008). For example, lamina propria-derived dendritic cells (DCs) induce the expression of CCR9 and $\alpha 4\beta 7$ -integrin in T cells when exposed to vitamin A, thus, promoting gut-homing in these T cells (Iwata et al., 2004). On the other hand, gut-homing molecules are suppressed in T cells by DCs in iLNs, while CCR10 and cutaneous lymphocyte antigen (CLA) are induced to promote skin-homing in turn (Biedermann et al., 2006; Sigmundsdottir et al., 2007). Adding to this, my work suggests that skin- and gut-draining LNs with their own microenvironment act as unique priming sites that could imprint specific gene signatures in autoreactive T cells, which then infiltrate into the CNS and exert distinct effector functions based on the adjuvant cues they received in their original priming environment. The microbiome will likely provide some of the adjuvant cues, especially in mLNs, and multiple studies showed alterations and a potential link of the gut microbiome in CNS autoimmunity (Ivanov et al., 2009; Jangi et al., 2016; Lee et al., 2011; Ochoa-Reparaz et al., 2010). However, the role of the skin microbiome in CNS autoimmunity is still less explored (Akdis, 2021). The tool I generated here could be indeed used to probe the interaction and the impact of environmental cues on T cell-mediated immunopathology in remote organs.

While neither i-T cells nor m-T cells fully overlapped with Th1 or Th17 cells, my data suggested that a mixed set of Th and Treg cells was primed in both LNs (Figure 8a, Figure 12c, d, e), with a slight bias where the iLN favors the priming of CNS-infiltrating Th1 cells, while the mLN favors Treg cells (Figure 21).

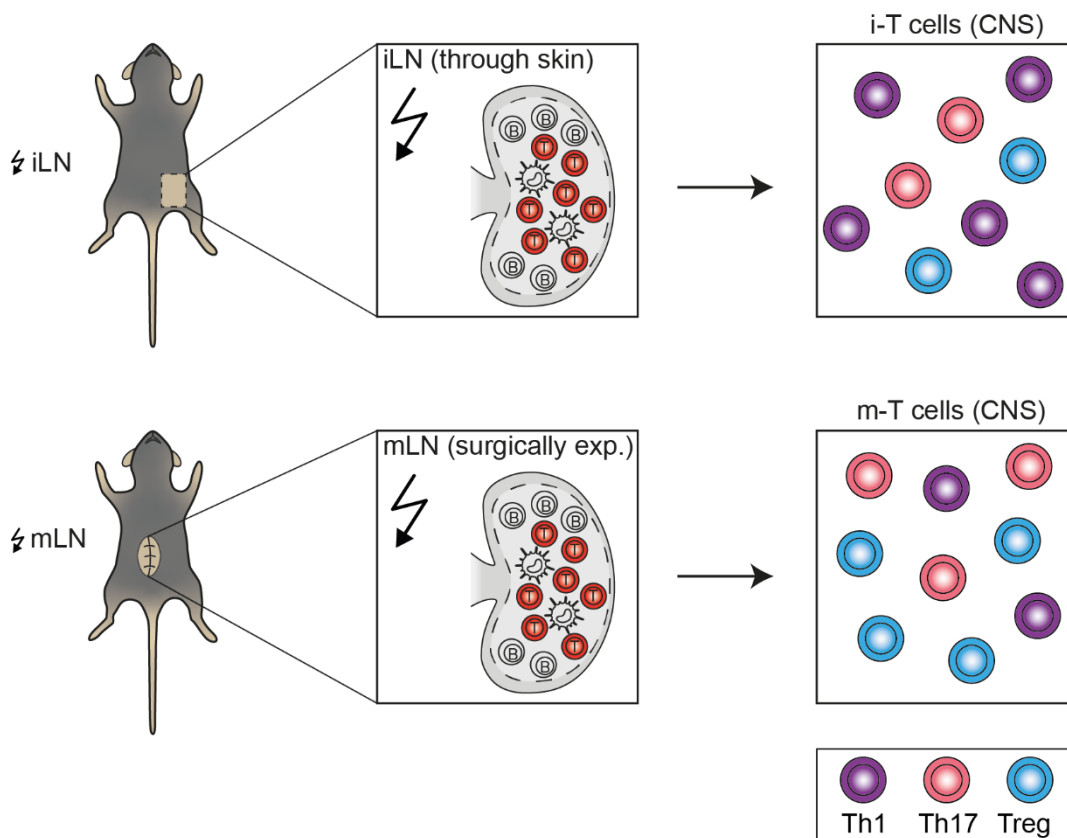


Figure 21: Mixed T cell phenotype of i- and m-T cells during EAE.

Schematic of primed i- and m-T cells and their distribution in the central nervous system (CNS) during experimental autoimmune encephalomyelitis (EAE). The experimental setup is described in Figure 6a. Irradiation is depicted as lightning symbol; inguinal lymph node (iLN); mesenteric lymph node (mLN).

However, since i- and m-T cells could not be assigned to any specific Th cell subset, we interrogated our scRNA-seq data for differential expressed genes that were upregulated in all organs of a certain stream (either i- or m-stream) compared to the other stream. We hypothesized that this would give us the means to identify i- or m-T cells based on their core gene signatures, which is ultimately defined by their respective priming site. This approach resulted in the identification of 94 i-T cell and 50 m-T cell core signature genes (Figure 13b).

Key markers to distinguish i- and m-T cells were the integrins *Itgb1* (i-T cells) and *Itga4* (m-T cells) (Figure 13e, f). Integrin $\alpha 4$ and $\beta 1$ are of particular interest in CNS autoimmunity because they form together the VLA-4 complex, which is known for CNS homing during autoimmunity because its ligand VCAM-1 is expressed highly on the vasculature of the inflamed brain (Wong and Dorovini-Zis, 1995). Blocking of VLA-4 with a monoclonal antibody against $\alpha 4$ -integrin prevented EAE in Lewis rats (Yednock et al., 1992) and has great efficacy in the treatment of MS patients (McCormack, 2013; Zameer and Hoffman, 2003). However, while m-T cells were all $\alpha 4$ -integrin positive and i-T cells were exclusively $\beta 1$ -integrin positive, the fraction of cells that expressed both subunits of the VLA-4 complex were comparable in the spleen (approximately 40%; Figure 15a left row, frequencies not shown). In fact, $\alpha 4$ -integrin can also pair with another β subunit, which is $\beta 7$ -integrin, to form the $\alpha 4\beta 7$ -integrin complex that is

known, together with CCR9, for homing to the intestine (Agace, 2006). Therefore, $\alpha 4$ -integrin positive T cells that are $\beta 1$ -integrin negative are consequently expressing $\beta 7$ -integrin and form the gut homing $\alpha 4\beta 7$ -integrin complex, which binds to mucosal addressin cell adhesion molecule-1 (MAdCAM-1) that is constitutively expressed on high endothelial venules (HEVs) of Peyer's patches and mLNs as well as on postcapillary venules of lamina propria in the gut (Gorfu et al., 2009). In contrast to $\beta 1$, which can bind to 12 different α subunits, $\beta 7$ only has two binding partners, $\alpha 4$ and αE , that have been associated with gut-selective lymphocyte homing ($\alpha 4\beta 7$) and retention in mucosal tissues ($\alpha E\beta 7$) (Hynes, 2002; Kilshaw, 1999). As described above, the gut homing markers $\alpha 4\beta 7$ -integrin and CCR9 can be imprinted in T cells by lamina propria-derived DCs in response to environmental cues like vitamin A (Iwata et al., 2004), which is in line with the high level of $\alpha 4\beta 7$ -integrin positive m-T cells. Selective imprinting of the gut homing complex $\alpha 4\beta 7$ -integrin in m-T cells compared to i-T cells further supported the hypothesis that these two priming stations form separate trajectories from the iLN and mLN through the spleen to the CNS, respectively, as the clonality analysis suggested (Figure 10d).

Homing of primed T cells to the inflamed CNS is indeed more nuanced, so it is not sufficient to focus on the $\alpha 4$ -integrin subunit and its binding partners. While VLA-4 expression has been shown to be essential for the infiltration of Th1 cells into the CNS, Th17 cells are able to infiltrate the CNS in the absence of VLA-4 in an LFA-1-mediated manner (Rothhammer et al., 2011; Schneider-Hohendorf et al., 2014). Moreover, Treg cells have also been shown to infiltrate the CNS in an LFA-1-dependent fashion in the absence of $\alpha 4$ -integrin, which might be a crucial ability of them to suppress Th17-mediated CNS autoimmunity independently of $\alpha 4$ -integrin (Glatigny et al., 2015). Following-up on the expression of LFA-1 as well as the impact of the ablation or blocking of VLA-4 and LFA-1 on the infiltration of i- and m-T cells into the CNS might add valuable insights about ways of targeting these two subsets specifically during CNS autoimmunity. Since m-T cells were comprised of a higher fraction of Treg cells in the CNS compared to i-T cells (Figure 8a), blocking the infiltration of i-T cells specifically could present a way that might prevent the influx of autoreactive effector T cells into the CNS, while allowing for the infiltration of more immune modulatory T cells.

Moreover, the chemokine receptor Cxcr6 was highly expressed in i-T cells on the RNA (Figure 13c, e, f) and protein level (Figure 15a, Figure 17c) compared to m-T cells. Cxcr6 is a marker for Th1 cells and is induced upon priming (Kim et al., 2001), which is in line with the enriched Th1 signature gene set in i-T cells, in particular in the CNS (Figure 12d). In an elegant fate-mapping study of GM-CSF expression during EAE, Komuczki and colleagues (Komuczki et al., 2019) showed that a subset of GM-CSF-expressing Th cells is pivotal for immunopathology and tissue destruction during EAE and that this subset expressed Cxcr6. This might highlight

the importance of *Cxcr6* (and in turn of i-T cells) on the immunopathology in the CNS, a point that will be addressed in more detail in chapter 7.6.

On the other hand, the purinergic receptor P2rx7 was highly expressed in m-T cells both on the RNA (Figure 13d, e, f) and protein level (Figure 15a) compared to i-T cells. P2rx7 is a sensor for extracellular adenosine triphosphate (eATP) with dual gating properties, meaning that low concentrations of eATP cause small amplitude currents while high concentrations result in cytolitic pore opening and cell death (Khadra et al., 2013). Stimulation of P2rx7 on T cells is context-dependent, based on the metabolic fitness and development stage of the T cell. While stimulation of P2rx7 in the thymus promotes $\gamma\delta$ T cell development, its stimulation in secondary lymphoid organs promotes the differentiation of Th1 and Th17 cells as well as the conversion of Treg cells to Th17 cells (Grassi, 2020). Interestingly, the intestinal environment is unique in regard to P2rx7 signaling, because it is the only milieu with a noteworthy concentration of eATP under physiologic conditions, which is produced by the microbiota (Proietti et al., 2019). Sensitivity to P2rx7-mediated cell death of T cells is defined by the intestinal microenvironment, for example by retinoic acid, which has been shown to upregulate P2rx7 on CD8⁺ and CD4⁺ T cells (Hashimoto-Hill et al., 2017; Heiss et al., 2008). In fact, most intestinal $\alpha\beta$ T cells, including Th1 and Th17 cells, and $\gamma\delta$ T cells express P2rx7 in a robust manner and intestinal effector T cells are eliminated by P2rx7-mediated cell death (Hashimoto-Hill et al., 2017). Contrary to that, it has been shown that P2rx7 activity is required for the generation and maintenance of central and tissue-resident memory CD8⁺ T cells by promoting metabolic fitness (Borges da Silva et al., 2018). This concept might also apply for CD4⁺ T cells and could suggest that m-T cells have a stronger memory potential, while i-T cells are more prone to have an effector phenotype, which is an interesting avenue that needs further investigation.

Moreover, we probed i- and m-T cells isolated from the spleen for differentially open chromatin regions with an assay for transposase-accessible chromatin with sequencing (ATAC-seq) analysis (Figure 14a). When we filtered for genes that were differently upregulated in i- or m-T cells (Figure 13c, d) and contained open chromatin, we identified 47 i-T cell genes and 18 m-T cell genes (Figure 14b). Key markers like *Itgb1* and *Cxcr6* for i-T cells as well as *Itga4* for m-T cells were among the list of genes with differentially open chromatin, supporting the notion that the core gene signatures for i- and m- T cells are indeed imprinted. In addition, we used a prediction model to assess transcription factor activity scores to probe for specific i- and m-T cell transcription factors. Interesting transcription factor candidates for i-T cells were *Crem*, *JunB*, *T-bet*, and *ROR γ t* and for m-T cells were *Tcf7*, *Maf*, *Prdm1*, and *Foxo1* (Figure 14d). While i-T cell transcription factor candidates are linked to effector functions, m-T cell transcription factor candidates are mainly associated with general T cell activation. These

candidates might provide good targets for future work to better understand the key differences of i- and m-T cells on a transcriptional level.

7.4 Integrity of the site-specific priming effects in alternative settings

The antigen dose and adjuvant concentration are known contributors to the T cell phenotype. Since iLNs are the primary draining LNs in EAE due to the route of administration in the form of subcutaneous tail-based immunization with MOG peptide 35-55 in complete Freund's adjuvants (CFA), it had to be excluded that the observed differences between i- and m-T cells were based on the nature of induction of the EAE model.

Neither the route of antigen delivery nor the antigen itself altered the expression of key i-T cell (*Cxcr6* and β 1-integrin) and m-T cell markers (*P2rx7* and α 4-integrin) in the spleen compared to the regular EAE model (Figure 15a, b). While this was also true for most of these markers in a spontaneous EAE model on a double transgenic TCR^{MOG} and B cell receptor (BCR)^{MOG} background, *Cxcr6* was quite comparable between both groups (Figure 15c). This might be due to an overall weaker inflammatory stimulus in spontaneous EAE mice compared to classical EAE mice due to the lack of adjuvants and much lower exposure to MOG antigen. However, on the RNA level *Cxcr6* was again moderately increased in i-T cells (Figure 16b), which could mean that the presentation of *Cxcr6* on the surface might take a bit longer than in the regular EAE model because of less inflammation. Importantly, i- and m-T cell core signatures from the regular EAE model were present in their counterparts in the spontaneous EAE model (Figure 16c), suggesting that these signatures were indeed imprinted in the T cells based on the specific LN station they were primed in, independent of the model that was used to study them.

7.5 Functional phenotypes of CNS-infiltrating i- and m-T cells

Thus far, I was able to show that i- and m-T cells have a unique transcriptional and open chromatin profile. However, in order to decipher functional phenotypes of these two Th cell subsets, I examined the CNS infiltration pattern during EAE since the integrins *Itga4* and *Itgb1* as well as the chemokine receptor *Cxcr6* were differentially expressed in both Th cell subsets.

Most interestingly, when I transferred CD44^{high} TCR^{MOG}-specific i- and m-T cells that were isolated from the spleen at day 8 after immunization into *Rag1*^{-/-} mice (experimental setup is described in Figure 18a), I not only observed that both i- and m-T cells were able to induce EAE in recipient mice (Figure 18b), but that they had a distinct CNS infiltration pattern. In the adoptive transfer system, both i- and m-T cells were able to infiltrate into the brainstem and the lumbar spinal cord, however, m-T cells were located predominantly in the white matter while i-T cells infiltrated both grey and white matter (Figure 18c). I tried to attribute this striking difference to specific disease manifestations. In a subset of diseased animals, I observed

atypical signs of EAE with absent motor deficits and predominant ataxia and severe imbalance at the disease onset that could be attributed to lesions localized in coordinative centers of the brain. However, both i- and m-T cell recipients were affected by this phenomenon and the maximal disease scores of i- and m-T cell recipients were comparable. Nevertheless, subtle differences like neurologic symptoms in form of an atypical EAE course are often difficult to detect at later disease stages as they are masked by paralysis that is caused by lesions in the lumbar spinal cord. Therefore, more efforts are necessary to elucidate what impact the i- and m-T cell-inherent CNS infiltration pattern has on the disease course.

One concern in adoptive transfer models is that the phenotype of the transferred cells might be unstable after transfer since Th cells are known to be plastic as discussed in chapter 7.3. In the context of EAE, it has been shown that adoptive transfer of *in vitro*-polarized Th cells with IL-12 or IL-23 induced distinct disease phenotypes and responsiveness to IFN- β treatment (Axtell et al., 2010; Kroenke et al., 2008), arguing that the transferred T cells were stable upon transfer to a certain degree. In line with this, adoptively transferred MOG-specific i- and m-T cells could still be distinguished by the expression of α 4-integrin after over 20 days of transfer (Figure 18d) and showed distinct CNS infiltration patterns in regard to white and grey matter distribution, which suggests that the imprinting of i- and m-T cell signatures was stable over many cell divisions.

7.6 Deciphering the underlying factors for differential CNS homing

When I tried to understand the causes behind the distinct grey versus white matter distribution of i- and m-T cells, I investigated the chemokine receptor Cxcr6 more closely. As described above, Cxcr6 is an important Th cell marker in the context of CNS autoimmunity and is predominantly expressed in i-T cells in the CNS.

The sole ligand of Cxcr6 is Cxcl16, which is expressed in the CNS (as well as many other tissues) and fulfills certain aspects that give it the potential to regulate immune responses in the CNS. For one, it is presented on the surface of antigen-presenting cells (APCs), like macrophages and DCs, and can act as an adhesion molecule for Cxcr6-expressing lymphocytes. In addition, shedding of Cxcl16 creates a chemotactic gradient that is able to attract activated T cells (Matloubian et al., 2000). Pneumococcal meningitis has been shown to up-regulate Cxcl16 in RAW264.7 macrophages in the cerebrospinal fluid (CSF) of patients and in the brain and CSF of mice, which led to the recruitment of Cxcr6-expressing neutrophils in a dose-dependent manner towards a Cxcl16 gradient (Woehrl et al., 2010). Moreover, DCs might be a potential source for Cxcl16 in the grey matter as they were found in CNS lesions (Serafini et al., 2006) and non-lesional grey matter in MS (Cudrici et al., 2007). Since the infiltration pattern of *Cxcr6*^{-/-} T cells in the lumbar spinal cord was comparable to m-T cells (Figure 19a), this suggested that the observed grey matter infiltration of i-T cells might be due

to their expression of *Cxcr6* that gave them the ability to sense and migrate to *Cxcl16* that was produced by APCs in the grey matter. Of note, *Cxcr6* expression was not essential for the infiltration of peripheral T cells into the CNS in the first place and *Cxcr6*^{-/-} mice showed similar disease manifestations when compared to wild-type (WT) mice (Figure 19b). Therefore, more work needs to be done to elucidate the impact of T cell localization in the CNS on the disease phenotype.

This work provides new insights on the influence of the peripheral site of Th cell priming on the Th cell transcriptome and phenotype in a remote organ like the CNS. Moreover, it demonstrates that T cells primed in skin- and gut-draining LNs can be identified by a LN-specific gene signature (i- versus m-T cells) rather than classical Th cell signatures. Defining Th cell subsets based on their site of peripheral priming might open a new and important avenue to understand and productively intervene with Th cell biology in autoimmune diseases and potentially any kind of adaptive immunity.

7.7 The role of tissue imprinting of immune cells on the immunopathology in remote organs

Imprinting of specific gene signatures in T cells based on their site of priming as shown here is an important concept that could improve our understanding of inflammatory processes in a wide variety of diseases. This work used models for CNS autoimmunity as an example to show how tissue-specific imprinting can affect the immunopathology in a remote organ, but likely is a general concept of Th cell biology. Importantly, priming site-specific imprinting in T cells was stable over time and was linked to specific disease phenotypes in the CNS, like infiltration patterns. Moreover, the CNS-infiltrating i-T cells seemed to have more of an effector phenotype, while m-T cells appeared overall more immune modulatory. In order to elucidate the mechanisms that are responsible for tissue imprinting on a molecular level, it will be crucial to identify the tissue-specific cues as well as the cells involved in the imprinting. Undoubtedly, DCs are prime candidates for T cell imprinting as has been shown in the context of tissue-specific lymphocyte trafficking (Sigmundsdottir and Butcher, 2008). In addition, identifying pathogenic T cell subsets that are associated with immunopathology in remote organs based on their tissue-imprinted signatures might improve our understanding of certain diseases and could provide ways to intervene with disease progression by targeting disease-relevant T cell subsets before they reach their target organ. Specifically blocking T cell subsets that induce immunopathology, while not obstructing T cell subsets that modulate immunopathology would have great therapeutic potential in organ-specific autoimmunity or chronic inflammatory diseases.

8 Bibliography

- Acuto, O., & Michel, F. (2003). CD28-mediated co-stimulation: a quantitative support for TCR signalling. *Nat Rev Immunol*, 3(12), 939-951. doi:10.1038/nri1248
- Adam, V., Berardozzi, R., Byrdin, M., & Bourgeois, D. (2014). Phototransformable fluorescent proteins: Future challenges. *Curr Opin Chem Biol*, 20, 92-102. doi:10.1016/j.cbpa.2014.05.016
- Adam, V., Moeyaert, B., David, C. C., Mizuno, H., Lelimosin, M., Dedecker, P., Ando, R., Miyawaki, A., Michiels, J., Engelborghs, Y., & Hofkens, J. (2011). Rational design of photoconvertible and biphotochromic fluorescent proteins for advanced microscopy applications. *Chem Biol*, 18(10), 1241-1251. doi:10.1016/j.chembiol.2011.08.007
- Agace, W. W. (2006). Tissue-tropic effector T cells: generation and targeting opportunities. *Nat Rev Immunol*, 6(9), 682-692. doi:10.1038/nri1869
- Agnello, D., Lankford, C. S., Bream, J., Morinobu, A., Gadina, M., O'Shea, J. J., & Frucht, D. M. (2003). Cytokines and transcription factors that regulate T helper cell differentiation: new players and new insights. *J Clin Immunol*, 23(3), 147-161. doi:10.1023/a:1023381027062
- Akdis, C. A. (2021). Does the epithelial barrier hypothesis explain the increase in allergy, autoimmunity and other chronic conditions? *Nat Rev Immunol*, 21(11), 739-751. doi:10.1038/s41577-021-00538-7
- Alizadeh, A., Dyck, S. M., & Karimi-Abdolrezaee, S. (2015). Myelin damage and repair in pathologic CNS: challenges and prospects. *Front Mol Neurosci*, 8, 35. doi:10.3389/fnmol.2015.00035
- Alli, R., Nguyen, P., & Geiger, T. L. (2008). Retrogenic modeling of experimental allergic encephalomyelitis associates T cell frequency but not TCR functional affinity with pathogenicity. *J Immunol*, 181(1), 136-145. doi:10.4049/jimmunol.181.1.136
- Alves de Lima, K., Rustenhoven, J., & Kipnis, J. (2020). Meningeal Immunity and Its Function in Maintenance of the Central Nervous System in Health and Disease. *Annu Rev Immunol*, 38, 597-620. doi:10.1146/annurev-immunol-102319-103410
- Ando, R., Hama, H., Yamamoto-Hino, M., Mizuno, H., & Miyawaki, A. (2002). An optical marker based on the UV-induced green-to-red photoconversion of a fluorescent protein. *Proc Natl Acad Sci U S A*, 99(20), 12651-12656. doi:10.1073/pnas.202320599
- Arpaia, N., Campbell, C., Fan, X., Dikiy, S., van der Veeken, J., deRoos, P., Liu, H., Cross, J. R., Pfeffer, K., Coffey, P. J., & Rudensky, A. Y. (2013). Metabolites produced by commensal bacteria promote peripheral regulatory T-cell generation. *Nature*, 504(7480), 451-455. doi:10.1038/nature12726
- Axtell, R. C., de Jong, B. A., Boniface, K., van der Voort, L. F., Bhat, R., De Sarno, P., Naves, R., Han, M., Zhong, F., Castellanos, J. G., Mair, R., Christakos, A., Kolkowitz, I., Katz, L., Killestein, J., Polman, C. H., de Waal Malefyt, R., Steinman, L., & Raman, C. (2010). T helper type 1 and 17 cells determine efficacy of interferon-beta in multiple sclerosis and experimental encephalomyelitis. *Nat Med*, 16(4), 406-412. doi:10.1038/nm.2110
- Baaten, B. J., Li, C. R., & Bradley, L. M. (2010). Multifaceted regulation of T cells by CD44. *Commun Integr Biol*, 3(6), 508-512. doi:10.4161/cib.3.6.13495
- Bartholomaeus, I., Kawakami, N., Odoardi, F., Schlager, C., Miljkovic, D., Ellwart, J. W., Klinkert, W. E., Flugel-Koch, C., Issekutz, T. B., Wekerle, H., & Flugel, A. (2009). Effector T cell interactions with meningeal vascular structures in nascent autoimmune CNS lesions. *Nature*, 462(7269), 94-98. doi:10.1038/nature08478

- Becattini, S., Latorre, D., Mele, F., Foglierini, M., De Gregorio, C., Cassotta, A., Fernandez, B., Kelderman, S., Schumacher, T. N., Corti, D., Lanzavecchia, A., & Sallusto, F. (2015). T cell immunity. Functional heterogeneity of human memory CD4(+) T cell clones primed by pathogens or vaccines. *Science*, 347(6220), 400-406. doi:10.1126/science.1260668
- Benson, R. A., Patakas, A., Conigliaro, P., Rush, C. M., Garside, P., McInnes, I. B., & Brewer, J. M. (2010). Identifying the cells breaching self-tolerance in autoimmunity. *J Immunol*, 184(11), 6378-6385. doi:10.4049/jimmunol.0903951
- Bettelli, E., Baeten, D., Jager, A., Sobel, R. A., & Kuchroo, V. K. (2006). Myelin oligodendrocyte glycoprotein-specific T and B cells cooperate to induce a Devic-like disease in mice. *J Clin Invest*, 116(9), 2393-2402. doi:10.1172/JCI28334
- Bettelli, E., Pagany, M., Weiner, H. L., Linington, C., Sobel, R. A., & Kuchroo, V. K. (2003). Myelin oligodendrocyte glycoprotein-specific T cell receptor transgenic mice develop spontaneous autoimmune optic neuritis. *J Exp Med*, 197(9), 1073-1081. doi:10.1084/jem.20021603
- Biedermann, T., Lametschwandtner, G., Tangemann, K., Kund, J., Hinteregger, S., Carballido-Perrig, N., Rot, A., Schwarzler, C., & Carballido, J. M. (2006). IL-12 instructs skin homing of human Th2 cells. *J Immunol*, 177(6), 3763-3770. doi:10.4049/jimmunol.177.6.3763
- Black, M., Bhattacharya, S., Philip, S., Norman, J. E., & McLernon, D. J. (2015). Planned Cesarean Delivery at Term and Adverse Outcomes in Childhood Health. *JAMA*, 314(21), 2271-2279. doi:10.1001/jama.2015.16176
- Borges da Silva, H., Beura, L. K., Wang, H., Hanse, E. A., Gore, R., Scott, M. C., Walsh, D. A., Block, K. E., Fonseca, R., Yan, Y., Hippen, K. L., Blazar, B. R., Masopust, D., Kelekar, A., Vulchanova, L., Hogquist, K. A., & Jameson, S. C. (2018). The purinergic receptor P2RX7 directs metabolic fitness of long-lived memory CD8(+) T cells. *Nature*, 559(7713), 264-268. doi:10.1038/s41586-018-0282-0
- Borgulya, P., Kishi, H., Muller, U., Kirberg, J., & von Boehmer, H. (1991). Development of the CD4 and CD8 lineage of T cells: instruction versus selection. *EMBO J*, 10(4), 913-918. doi:10.1002/j.1460-2075.1991.tb08024.x
- Bousso, P. (2008). T-cell activation by dendritic cells in the lymph node: lessons from the movies. *Nat Rev Immunol*, 8(9), 675-684. doi:10.1038/nri2379
- Bradley, L. M., Watson, S. R., & Swain, S. L. (1994). Entry of naive CD4 T cells into peripheral lymph nodes requires L-selectin. *J Exp Med*, 180(6), 2401-2406. doi:10.1084/jem.180.6.2401
- Bretscher, P. A. (1999). A two-step, two-signal model for the primary activation of precursor helper T cells. *Proc Natl Acad Sci U S A*, 96(1), 185-190. doi:10.1073/pnas.96.1.185
- Brickman, C. M., & Shoenfeld, Y. (2001). The mosaic of autoimmunity. *Scand J Clin Lab Invest Suppl*, 235, 3-15.
- Buenrostro, J. D., Giresi, P. G., Zaba, L. C., Chang, H. Y., & Greenleaf, W. J. (2013). Transposition of native chromatin for fast and sensitive epigenomic profiling of open chromatin, DNA-binding proteins and nucleosome position. *Nat Methods*, 10(12), 1213-1218. doi:10.1038/nmeth.2688
- Buenrostro, J. D., Wu, B., Chang, H. Y., & Greenleaf, W. J. (2015). ATAC-seq: A Method for Assaying Chromatin Accessibility Genome-Wide. *Curr Protoc Mol Biol*, 109, 21 29 21-29 29. doi:10.1002/0471142727.mb2129s109
- Butler, A., Hoffman, P., Smibert, P., Papalexi, E., & Satija, R. (2018). Integrating single-cell transcriptomic data across different conditions, technologies, and species. *Nat Biotechnol*, 36(5), 411-420. doi:10.1038/nbt.4096

- Butzkueven, H., Kappos, L., Pellegrini, F., Trojano, M., Wiendl, H., Patel, R. N., Zhang, A., Hotermans, C., Belachew, S., & Investigators, T. O. P. (2014). Efficacy and safety of natalizumab in multiple sclerosis: interim observational programme results. *J Neurol Neurosurg Psychiatry*, *85*(11), 1190-1197. doi:10.1136/jnnp-2013-306936
- Byrd, A. L., Deming, C., Cassidy, S. K. B., Harrison, O. J., Ng, W. I., Conlan, S., Program, N. C. S., Belkaid, Y., Segre, J. A., & Kong, H. H. (2017). Staphylococcus aureus and Staphylococcus epidermidis strain diversity underlying pediatric atopic dermatitis. *Sci Transl Med*, *9*(397). doi:10.1126/scitranslmed.aal4651
- Cho, J. H., & Gregersen, P. K. (2011). Genomics and the multifactorial nature of human autoimmune disease. *N Engl J Med*, *365*(17), 1612-1623. doi:10.1056/NEJMra1100030
- Chudakov, D. M., Lukyanov, S., & Lukyanov, K. A. (2007). Tracking intracellular protein movements using photoswitchable fluorescent proteins PS-CFP2 and Dendra2. *Nat Protoc*, *2*(8), 2024-2032. doi:10.1038/nprot.2007.291
- Cibrian, D., & Sanchez-Madrid, F. (2017). CD69: from activation marker to metabolic gatekeeper. *Eur J Immunol*, *47*(6), 946-953. doi:10.1002/eji.201646837
- Collaborators, G. B. D. N. (2019). Global, regional, and national burden of neurological disorders, 1990-2016: a systematic analysis for the Global Burden of Disease Study 2016. *Lancet Neurol*, *18*(5), 459-480. doi:10.1016/S1474-4422(18)30499-X
- Compston, A., & Coles, A. (2008). Multiple sclerosis. *Lancet*, *372*(9648), 1502-1517. doi:10.1016/S0140-6736(08)61620-7
- Corces, M. R., Trevino, A. E., Hamilton, E. G., Greenside, P. G., Sinnott-Armstrong, N. A., Vesuna, S., Satpathy, A. T., Rubin, A. J., Montine, K. S., Wu, B., Kathiria, A., Cho, S. W., Mumbach, M. R., Carter, A. C., Kasowski, M., Orloff, L. A., Risca, V. I., Kundaje, A., Khavari, P. A., Montine, T. J., Greenleaf, W. J., & Chang, H. Y. (2017). An improved ATAC-seq protocol reduces background and enables interrogation of frozen tissues. *Nat Methods*, *14*(10), 959-962. doi:10.1038/nmeth.4396
- Cudrici, C., Ito, T., Zafranskaia, E., Niculescu, F., Mullen, K. M., Vlaicu, S., Judge, S. I., Calabresi, P. A., & Rus, H. (2007). Dendritic cells are abundant in non-lesional gray matter in multiple sclerosis. *Exp Mol Pathol*, *83*(2), 198-206. doi:10.1016/j.yexmp.2007.05.006
- Daneman, R., & Prat, A. (2015). The blood-brain barrier. *Cold Spring Harb Perspect Biol*, *7*(1), a020412. doi:10.1101/cshperspect.a020412
- Donskoy, E., & Goldschneider, I. (1992). Thymocytopoiesis is maintained by blood-borne precursors throughout postnatal life. A study in parabiotic mice. *J Immunol*, *148*(6), 1604-1612.
- Flajnik, M. F., & Kasahara, M. (2010). Origin and evolution of the adaptive immune system: genetic events and selective pressures. *Nat Rev Genet*, *11*(1), 47-59. doi:10.1038/nrg2703
- Fletcher, J. M., Llorca, S. J., Sweeney, C. M., Tubridy, N., & Mills, K. H. (2010). T cells in multiple sclerosis and experimental autoimmune encephalomyelitis. *Clin Exp Immunol*, *162*(1), 1-11. doi:10.1111/j.1365-2249.2010.04143.x
- Ghasemi, N., Razavi, S., & Nikzad, E. (2017). Multiple Sclerosis: Pathogenesis, Symptoms, Diagnoses and Cell-Based Therapy. *Cell J*, *19*(1), 1-10. doi:10.22074/cellj.2016.4867
- Girgis, C. M., Champion, B. L., & Wall, J. R. (2011). Current concepts in graves' disease. *Ther Adv Endocrinol Metab*, *2*(3), 135-144. doi:10.1177/2042018811408488
- Glatigny, S., Duhon, R., Arbelaez, C., Kumari, S., & Bettelli, E. (2015). Integrin alpha L controls the homing of regulatory T cells during CNS autoimmunity in the absence of integrin alpha 4. *Sci Rep*, *5*, 7834. doi:10.1038/srep07834

- Goldmann, T., Wieghofer, P., Jordao, M. J., Prutek, F., Hagemeyer, N., Frenzel, K., Amann, L., Staszewski, O., Kierdorf, K., Krueger, M., Locatelli, G., Hochgerner, H., Zeiser, R., Eelman, S., Geissmann, F., Priller, J., Rossi, F. M., Bechmann, I., Kerschensteiner, M., Linnarsson, S., Jung, S., & Prinz, M. (2016). Origin, fate and dynamics of macrophages at central nervous system interfaces. *Nat Immunol*, *17*(7), 797-805. doi:10.1038/ni.3423
- Gorfu, G., Rivera-Nieves, J., & Ley, K. (2009). Role of beta7 integrins in intestinal lymphocyte homing and retention. *Curr Mol Med*, *9*(7), 836-850. doi:10.2174/156652409789105525
- Grassi, F. (2020). The P2X7 Receptor as Regulator of T Cell Development and Function. *Front Immunol*, *11*, 1179. doi:10.3389/fimmu.2020.01179
- Greiling, T. M., Dehner, C., Chen, X., Hughes, K., Iniguez, A. J., Boccitto, M., Ruiz, D. Z., Renfro, S. C., Vieira, S. M., Ruff, W. E., Sim, S., Kriegel, C., Glanternik, J., Chen, X., Girardi, M., Degnan, P., Costenbader, K. H., Goodman, A. L., Wolin, S. L., & Kriegel, M. A. (2018). Commensal orthologs of the human autoantigen Ro60 as triggers of autoimmunity in lupus. *Sci Transl Med*, *10*(434). doi:10.1126/scitranslmed.aan2306
- Gurskaya, N. G., Verkhusha, V. V., Shcheglov, A. S., Staroverov, D. B., Chepurnykh, T. V., Fradkov, A. F., Lukyanov, S., & Lukyanov, K. A. (2006). Engineering of a monomeric green-to-red photoactivatable fluorescent protein induced by blue light. *Nat Biotechnol*, *24*(4), 461-465. doi:10.1038/nbt1191
- Harbour, S. N., DiToro, D. F., Witte, S. J., Zindl, C. L., Gao, M., Schoeb, T. R., Jones, G. W., Jones, S. A., Hatton, R. D., & Weaver, C. T. (2020). TH17 cells require ongoing classic IL-6 receptor signaling to retain transcriptional and functional identity. *Sci Immunol*, *5*(49). doi:10.1126/sciimmunol.aaw2262
- Harel, M., & Shoenfeld, Y. (2006). Predicting and preventing autoimmunity, myth or reality? *Ann N Y Acad Sci*, *1069*, 322-345. doi:10.1196/annals.1351.031
- Hashimoto-Hill, S., Friesen, L., Kim, M., & Kim, C. H. (2017). Contraction of intestinal effector T cells by retinoic acid-induced purinergic receptor P2X7. *Mucosal Immunol*, *10*(4), 912-923. doi:10.1038/mi.2016.109
- Heinz, S., Benner, C., Spann, N., Bertolino, E., Lin, Y. C., Laslo, P., Cheng, J. X., Murre, C., Singh, H., & Glass, C. K. (2010). Simple combinations of lineage-determining transcription factors prime cis-regulatory elements required for macrophage and B cell identities. *Mol Cell*, *38*(4), 576-589. doi:10.1016/j.molcel.2010.05.004
- Heiss, K., Janner, N., Mahnss, B., Schumacher, V., Koch-Nolte, F., Haag, F., & Mittrucker, H. W. (2008). High sensitivity of intestinal CD8+ T cells to nucleotides indicates P2X7 as a regulator for intestinal T cell responses. *J Immunol*, *181*(6), 3861-3869. doi:10.4049/jimmunol.181.6.3861
- Hemmer, B., Kerschensteiner, M., & Korn, T. (2015). Role of the innate and adaptive immune responses in the course of multiple sclerosis. *Lancet Neurol*, *14*(4), 406-419. doi:10.1016/S1474-4422(14)70305-9
- Hiltensperger, M., Beltrán, E., Kant, R., Tyystjärvi, S., Lepennetier, G., Domínguez Moreno, H., Bauer, I. J., Grassmann, S., Jarosch, S., Schober, K., Buchholz, V. R., Kenet, S., Gasperi, C., Öllinger, R., Rad, R., Muschaweckh, A., Sie, C., Aly, L., Knier, B., Garg, G., Afzali, A. M., Gerdes, L. A., Kümpfel, T., Franzenburg, S., Kawakami, N., Hemmer, B., Busch, D. H., Misgeld, T., Dornmair, K., & Korn, T. (2021). Skin and gut imprinted helper T cell subsets exhibit distinct functional phenotypes in central nervous system autoimmunity. *Nature Immunology*. doi:10.1038/s41590-021-00948-8
- Hiltensperger, M., & Korn, T. (2018). The Interleukin (IL)-23/T helper (Th)17 Axis in Experimental Autoimmune Encephalomyelitis and Multiple Sclerosis. *Cold Spring Harb Perspect Med*, *8*(1). doi:10.1101/cshperspect.a029637

- Hirahara, K., Vahedi, G., Ghoreschi, K., Yang, X. P., Nakayamada, S., Kanno, Y., O'Shea, J. J., & Laurence, A. (2011). Helper T-cell differentiation and plasticity: insights from epigenetics. *Immunology*, *134*(3), 235-245. doi:10.1111/j.1365-2567.2011.03483.x
- Hirota, K., Duarte, J. H., Veldhoen, M., Hornsby, E., Li, Y., Cua, D. J., Ahlfors, H., Wilhelm, C., Tolaini, M., Menzel, U., Garefalaki, A., Potocnik, A. J., & Stockinger, B. (2011). Fate mapping of IL-17-producing T cells in inflammatory responses. *Nat Immunol*, *12*(3), 255-263. doi:10.1038/ni.1993
- Hsieh, C. S., Lee, H. M., & Lio, C. W. (2012). Selection of regulatory T cells in the thymus. *Nat Rev Immunol*, *12*(3), 157-167. doi:10.1038/nri3155
- Hynes, R. O. (2002). Integrins: bidirectional, allosteric signaling machines. *Cell*, *110*(6), 673-687. doi:10.1016/s0092-8674(02)00971-6
- Iliff, J. J., Wang, M., Liao, Y., Plogg, B. A., Peng, W., Gundersen, G. A., Benveniste, H., Vates, G. E., Deane, R., Goldman, S. A., Nagelhus, E. A., & Nedergaard, M. (2012). A paravascular pathway facilitates CSF flow through the brain parenchyma and the clearance of interstitial solutes, including amyloid beta. *Sci Transl Med*, *4*(147), 147ra111. doi:10.1126/scitranslmed.3003748
- Ivanov, I., Atarashi, K., Manel, N., Brodie, E. L., Shima, T., Karaoz, U., Wei, D., Goldfarb, K. C., Santee, C. A., Lynch, S. V., Tanoue, T., Imaoka, A., Itoh, K., Takeda, K., Umesaki, Y., Honda, K., & Littman, D. R. (2009). Induction of intestinal Th17 cells by segmented filamentous bacteria. *Cell*, *139*(3), 485-498. doi:10.1016/j.cell.2009.09.033
- Ivanova, E. A., & Orekhov, A. N. (2015). T Helper Lymphocyte Subsets and Plasticity in Autoimmunity and Cancer: An Overview. *Biomed Res Int*, *2015*, 327470. doi:10.1155/2015/327470
- Iwata, M., Hirakiyama, A., Eshima, Y., Kagechika, H., Kato, C., & Song, S. Y. (2004). Retinoic acid imprints gut-homing specificity on T cells. *Immunity*, *21*(4), 527-538. doi:10.1016/j.immuni.2004.08.011
- Jangi, S., Gandhi, R., Cox, L. M., Li, N., von Glehn, F., Yan, R., Patel, B., Mazzola, M. A., Liu, S., Glanz, B. L., Cook, S., Tankou, S., Stuart, F., Melo, K., Nejad, P., Smith, K., Topcuolu, B. D., Holden, J., Kivisakk, P., Chitnis, T., De Jager, P. L., Quintana, F. J., Gerber, G. K., Bry, L., & Weiner, H. L. (2016). Alterations of the human gut microbiome in multiple sclerosis. *Nat Commun*, *7*, 12015. doi:10.1038/ncomms12015
- Kachikwu, E. L., Iwamoto, K. S., Liao, Y. P., DeMarco, J. J., Agazaryan, N., Economou, J. S., McBride, W. H., & Schaeue, D. (2011). Radiation enhances regulatory T cell representation. *Int J Radiat Oncol Biol Phys*, *81*(4), 1128-1135. doi:10.1016/j.ijrobp.2010.09.034
- Katsarou, A., Gudbjornsdottir, S., Rawshani, A., Dabelea, D., Bonifacio, E., Anderson, B. J., Jacobsen, L. M., Schatz, D. A., & Lernmark, A. (2017). Type 1 diabetes mellitus. *Nat Rev Dis Primers*, *3*, 17016. doi:10.1038/nrdp.2017.16
- Kemter, A. M., & Nagler, C. R. (2019). Influences on allergic mechanisms through gut, lung, and skin microbiome exposures. *J Clin Invest*, *129*(4), 1483-1492. doi:10.1172/JCI124610
- Khadra, A., Tomic, M., Yan, Z., Zemkova, H., Sherman, A., & Stojilkovic, S. S. (2013). Dual gating mechanism and function of P2X7 receptor channels. *Biophys J*, *104*(12), 2612-2621. doi:10.1016/j.bpj.2013.05.006
- Kijanka, G., Prokopowicz, M., Schellekens, H., & Brinks, V. (2014). Influence of aggregation and route of injection on the biodistribution of mouse serum albumin. *PLoS One*, *9*(1), e85281. doi:10.1371/journal.pone.0085281
- Kilshaw, P. J. (1999). Alpha E beta 7. *Mol Pathol*, *52*(4), 203-207. doi:10.1136/mp.52.4.203

- Kim, C. H., Kunkel, E. J., Boisvert, J., Johnston, B., Campbell, J. J., Genovese, M. C., Greenberg, H. B., & Butcher, E. C. (2001). Bonzo/CXCR6 expression defines type 1-polarized T-cell subsets with extralymphoid tissue homing potential. *J Clin Invest*, *107*(5), 595-601. doi:10.1172/JCI11902
- Kirby, T. O., & Ochoa-Reparaz, J. (2018). The Gut Microbiome in Multiple Sclerosis: A Potential Therapeutic Avenue. *Med Sci (Basel)*, *6*(3). doi:10.3390/medsci6030069
- Klein, L., Robey, E. A., & Hsieh, C. S. (2019). Central CD4(+) T cell tolerance: deletion versus regulatory T cell differentiation. *Nat Rev Immunol*, *19*(1), 7-18. doi:10.1038/s41577-018-0083-6
- Komuczki, J., Tuzlak, S., Friebel, E., Hartwig, T., Spath, S., Rosenstiel, P., Waisman, A., Opitz, L., Oukka, M., Schreiner, B., Pelczar, P., & Becher, B. (2019). Fate-Mapping of GM-CSF Expression Identifies a Discrete Subset of Inflammation-Driving T Helper Cells Regulated by Cytokines IL-23 and IL-1beta. *Immunity*, *50*(5), 1289-1304 e1286. doi:10.1016/j.immuni.2019.04.006
- Korn, T., Bettelli, E., Oukka, M., & Kuchroo, V. K. (2009). IL-17 and Th17 Cells. *Annu Rev Immunol*, *27*, 485-517. doi:10.1146/annurev.immunol.021908.132710
- Korn, T., & Hiltensperger, M. (2021). Role of IL-6 in the commitment of T cell subsets. *Cytokine*, *146*, 155654. doi:10.1016/j.cyto.2021.155654
- Korn, T., & Kallies, A. (2017). T cell responses in the central nervous system. *Nat Rev Immunol*, *17*(3), 179-194. doi:10.1038/nri.2016.144
- Korn, T., Reddy, J., Gao, W., Bettelli, E., Awasthi, A., Petersen, T. R., Backstrom, B. T., Sobel, R. A., Wucherpfennig, K. W., Strom, T. B., Oukka, M., & Kuchroo, V. K. (2007). Myelin-specific regulatory T cells accumulate in the CNS but fail to control autoimmune inflammation. *Nat Med*, *13*(4), 423-431. doi:10.1038/nm1564
- Kremers, G. J., Hazelwood, K. L., Murphy, C. S., Davidson, M. W., & Piston, D. W. (2009). Photoconversion in orange and red fluorescent proteins. *Nat Methods*, *6*(5), 355-358. doi:10.1038/nmeth.1319
- Krishnamoorthy, G., Lassmann, H., Wekerle, H., & Holz, A. (2006). Spontaneous opticospinal encephalomyelitis in a double-transgenic mouse model of autoimmune T cell/B cell cooperation. *J Clin Invest*, *116*(9), 2385-2392. doi:10.1172/JCI28330
- Kroenke, M. A., Carlson, T. J., Andjelkovic, A. V., & Segal, B. M. (2008). IL-12- and IL-23-modulated T cells induce distinct types of EAE based on histology, CNS chemokine profile, and response to cytokine inhibition. *J Exp Med*, *205*(7), 1535-1541. doi:10.1084/jem.20080159
- Kyratsous, N. I., Bauer, I. J., Zhang, G., Pesic, M., Bartholomaeus, I., Mues, M., Fang, P., Worner, M., Everts, S., Ellwart, J. W., Watt, J. M., Potter, B. V. L., Hohlfeld, R., Wekerle, H., & Kawakami, N. (2017). Visualizing context-dependent calcium signaling in encephalitogenic T cells in vivo by two-photon microscopy. *Proc Natl Acad Sci U S A*, *114*(31), E6381-E6389. doi:10.1073/pnas.1701806114
- Langmead, B. (2010). Aligning short sequencing reads with Bowtie. *Curr Protoc Bioinformatics*, Chapter 11, Unit 11 17. doi:10.1002/0471250953.bi1107s32
- Lee, P. P., Fitzpatrick, D. R., Beard, C., Jessup, H. K., Lehar, S., Makar, K. W., Perez-Melgosa, M., Sweetser, M. T., Schlissel, M. S., Nguyen, S., Cherry, S. R., Tsai, J. H., Tucker, S. M., Weaver, W. M., Kelso, A., Jaenisch, R., & Wilson, C. B. (2001). A critical role for Dnmt1 and DNA methylation in T cell development, function, and survival. *Immunity*, *15*(5), 763-774. doi:10.1016/s1074-7613(01)00227-8
- Lee, Y. K., Menezes, J. S., Umesaki, Y., & Mazmanian, S. K. (2011). Proinflammatory T-cell responses to gut microbiota promote experimental autoimmune encephalomyelitis. *Proc Natl Acad Sci U S A*, *108 Suppl 1*, 4615-4622. doi:10.1073/pnas.1000082107

- Lee, Y. K., Turner, H., Maynard, C. L., Oliver, J. R., Chen, D., Elson, C. O., & Weaver, C. T. (2009). Late developmental plasticity in the T helper 17 lineage. *Immunity*, *30*(1), 92-107. doi:10.1016/j.immuni.2008.11.005
- Li, Z., Schulz, M. H., Look, T., Begemann, M., Zenke, M., & Costa, I. G. (2019). Identification of transcription factor binding sites using ATAC-seq. *Genome Biol*, *20*(1), 45. doi:10.1186/s13059-019-1642-2
- Liao, S., & von der Weid, P. Y. (2015). Lymphatic system: an active pathway for immune protection. *Semin Cell Dev Biol*, *38*, 83-89. doi:10.1016/j.semcdb.2014.11.012
- Liew, F. Y. (2002). T(H)1 and T(H)2 cells: a historical perspective. *Nat Rev Immunol*, *2*(1), 55-60. doi:10.1038/nri705
- Lind, E. F., Prockop, S. E., Porritt, H. E., & Petrie, H. T. (2001). Mapping precursor movement through the postnatal thymus reveals specific microenvironments supporting defined stages of early lymphoid development. *J Exp Med*, *194*(2), 127-134. doi:10.1084/jem.194.2.127
- Litzenburger, T., Fassler, R., Bauer, J., Lassmann, H., Linington, C., Wekerle, H., & Iglesias, A. (1998). B lymphocytes producing demyelinating autoantibodies: development and function in gene-targeted transgenic mice. *J Exp Med*, *188*(1), 169-180. doi:10.1084/jem.188.1.169
- Macosko, E. Z., Basu, A., Satija, R., Nemesh, J., Shekhar, K., Goldman, M., Tirosh, I., Bialas, A. R., Kamitaki, N., Martersteck, E. M., Trombetta, J. J., Weitz, D. A., Sanes, J. R., Shalek, A. K., Regev, A., & McCarroll, S. A. (2015). Highly Parallel Genome-wide Expression Profiling of Individual Cells Using Nanoliter Droplets. *Cell*, *161*(5), 1202-1214. doi:10.1016/j.cell.2015.05.002
- Manfredo Vieira, S., Hiltensperger, M., Kumar, V., Zegarra-Ruiz, D., Dehner, C., Khan, N., Costa, F. R. C., Tiniakou, E., Greiling, T., Ruff, W., Barbieri, A., Kriegel, C., Mehta, S. S., Knight, J. R., Jain, D., Goodman, A. L., & Kriegel, M. A. (2018). Translocation of a gut pathobiont drives autoimmunity in mice and humans. *Science*, *359*(6380), 1156-1161. doi:10.1126/science.aar7201
- Matloubian, M., David, A., Engel, S., Ryan, J. E., & Cyster, J. G. (2000). A transmembrane CXC chemokine is a ligand for HIV-coreceptor Bonzo. *Nat Immunol*, *1*(4), 298-304. doi:10.1038/79738
- McCormack, P. L. (2013). Natalizumab: a review of its use in the management of relapsing-remitting multiple sclerosis. *Drugs*, *73*(13), 1463-1481. doi:10.1007/s40265-013-0102-7
- Metzger, D., Clifford, J., Chiba, H., & Chambon, P. (1995). Conditional site-specific recombination in mammalian cells using a ligand-dependent chimeric Cre recombinase. *Proc Natl Acad Sci U S A*, *92*(15), 6991-6995. doi:10.1073/pnas.92.15.6991
- Mombaerts, P., Iacomini, J., Johnson, R. S., Herrup, K., Tonegawa, S., & Papaioannou, V. E. (1992). RAG-1-deficient mice have no mature B and T lymphocytes. *Cell*, *68*(5), 869-877. doi:10.1016/0092-8674(92)90030-g
- Mukasa, R., Balasubramani, A., Lee, Y. K., Whitley, S. K., Weaver, B. T., Shibata, Y., Crawford, G. E., Hatton, R. D., & Weaver, C. T. (2010). Epigenetic instability of cytokine and transcription factor gene loci underlies plasticity of the T helper 17 cell lineage. *Immunity*, *32*(5), 616-627. doi:10.1016/j.immuni.2010.04.016
- Murphy, E., Shibuya, K., Hosken, N., Openshaw, P., Maino, V., Davis, K., Murphy, K., & O'Garra, A. (1996). Reversibility of T helper 1 and 2 populations is lost after long-term stimulation. *J Exp Med*, *183*(3), 901-913. doi:10.1084/jem.183.3.901

- Murphy, K. M., & Stockinger, B. (2010). Effector T cell plasticity: flexibility in the face of changing circumstances. *Nat Immunol*, *11*(8), 674-680. doi:10.1038/ni.1899
- Nguyen, P., Liu, W., Ma, J., Manirarora, J. N., Liu, X., Cheng, C., & Geiger, T. L. (2010). Discrete TCR repertoires and CDR3 features distinguish effector and Foxp3+ regulatory T lymphocytes in myelin oligodendrocyte glycoprotein-induced experimental allergic encephalomyelitis. *J Immunol*, *185*(7), 3895-3904. doi:10.4049/jimmunol.1001550
- O'Gorman, C., Bukhari, W., Todd, A., Freeman, S., & Broadley, S. A. (2014). Smoking increases the risk of multiple sclerosis in Queensland, Australia. *J Clin Neurosci*, *21*(10), 1730-1733. doi:10.1016/j.jocn.2014.01.009
- Ochoa-Reparaz, J., Mielcarz, D. W., Wang, Y., Begum-Haque, S., Dasgupta, S., Kasper, D. L., & Kasper, L. H. (2010). A polysaccharide from the human commensal *Bacteroides fragilis* protects against CNS demyelinating disease. *Mucosal Immunol*, *3*(5), 487-495. doi:10.1038/mi.2010.29
- Ousman, S. S., & Kuberski, P. (2012). Immune surveillance in the central nervous system. *Nat Neurosci*, *15*(8), 1096-1101. doi:10.1038/nn.3161
- Papadopoulos, Z., Herz, J., & Kipnis, J. (2020). Meningeal Lymphatics: From Anatomy to Central Nervous System Immune Surveillance. *J Immunol*, *204*(2), 286-293. doi:10.4049/jimmunol.1900838
- Parekh, S., Ziegenhain, C., Vieth, B., Enard, W., & Hellmann, I. (2016). The impact of amplification on differential expression analyses by RNA-seq. *Sci Rep*, *6*, 25533. doi:10.1038/srep25533
- Patterson, G. H., & Lippincott-Schwartz, J. (2002). A photoactivatable GFP for selective photolabeling of proteins and cells. *Science*, *297*(5588), 1873-1877. doi:10.1126/science.1074952
- Petermann, F., & Korn, T. (2011). Cytokines and effector T cell subsets causing autoimmune CNS disease. *FEBS Lett*, *585*(23), 3747-3757. doi:10.1016/j.febslet.2011.03.064
- Pham, A. H., McCaffery, J. M., & Chan, D. C. (2012). Mouse lines with photo-activatable mitochondria to study mitochondrial dynamics. *Genesis*, *50*(11), 833-843. doi:10.1002/dvg.22050
- Proietti, M., Perruzza, L., Scribano, D., Pellegrini, G., D'Antuono, R., Strati, F., Raffaelli, M., Gonzalez, S. F., Thelen, M., Hardt, W. D., Slack, E., Nicoletti, M., & Grassi, F. (2019). ATP released by intestinal bacteria limits the generation of protective IgA against enteropathogens. *Nat Commun*, *10*(1), 250. doi:10.1038/s41467-018-08156-z
- Reboldi, A., Coisne, C., Baumjohann, D., Benvenuto, F., Bottinelli, D., Lira, S., Uccelli, A., Lanzavecchia, A., Engelhardt, B., & Sallusto, F. (2009). C-C chemokine receptor 6-regulated entry of TH-17 cells into the CNS through the choroid plexus is required for the initiation of EAE. *Nat Immunol*, *10*(5), 514-523. doi:10.1038/ni.1716
- Reich, D. S., Lucchinetti, C. F., & Calabresi, P. A. (2018). Multiple Sclerosis. *N Engl J Med*, *378*(2), 169-180. doi:10.1056/NEJMra1401483
- Robinson, A. P., Harp, C. T., Noronha, A., & Miller, S. D. (2014). The experimental autoimmune encephalomyelitis (EAE) model of MS: utility for understanding disease pathophysiology and treatment. *Handb Clin Neurol*, *122*, 173-189. doi:10.1016/B978-0-444-52001-2.00008-X
- Ronchi, F., Basso, C., Preite, S., Reboldi, A., Baumjohann, D., Perlini, L., Lanzavecchia, A., & Sallusto, F. (2016). Experimental priming of encephalitogenic Th1/Th17 cells requires pertussis toxin-driven IL-1 β production by myeloid cells. *Nat Commun*, *7*, 11541. doi:10.1038/ncomms11541

- Rothhammer, V., Heink, S., Petermann, F., Srivastava, R., Claussen, M. C., Hemmer, B., & Korn, T. (2011). Th17 lymphocytes traffic to the central nervous system independently of alpha4 integrin expression during EAE. *J Exp Med*, *208*(12), 2465-2476. doi:10.1084/jem.20110434
- Ruff, W. E., Greiling, T. M., & Kriegel, M. A. (2020). Host-microbiota interactions in immune-mediated diseases. *Nat Rev Microbiol*, *18*(9), 521-538. doi:10.1038/s41579-020-0367-2
- Sawcer, S., Ban, M., Maranian, M., Yeo, T. W., Compston, A., Kirby, A., Daly, M. J., De Jager, P. L., Walsh, E., Lander, E. S., Rioux, J. D., Hafler, D. A., Ivins, A., Rimmler, J., Gregory, S. G., Schmidt, S., Pericak-Vance, M. A., Akesson, E., Hillert, J., Datta, P., Oturai, A., Ryder, L. P., Harbo, H. F., Spurkland, A., Myhr, K. M., Laaksonen, M., Booth, D., Heard, R., Stewart, G., Lincoln, R., Barcellos, L. F., Hauser, S. L., Oksenberg, J. R., Kenealy, S. J., Haines, J. L., & International Multiple Sclerosis Genetics, C. (2005). A high-density screen for linkage in multiple sclerosis. *Am J Hum Genet*, *77*(3), 454-467. doi:10.1086/444547
- Scharschmidt, T. C., Vasquez, K. S., Truong, H. A., Gearty, S. V., Pauli, M. L., Nosbaum, A., Gratz, I. K., Otto, M., Moon, J. J., Liese, J., Abbas, A. K., Fischbach, M. A., & Rosenblum, M. D. (2015). A Wave of Regulatory T Cells into Neonatal Skin Mediates Tolerance to Commensal Microbes. *Immunity*, *43*(5), 1011-1021. doi:10.1016/j.immuni.2015.10.016
- Schneider-Hohendorf, T., Rossaint, J., Mohan, H., Boning, D., Breuer, J., Kuhlmann, T., Gross, C. C., Flanagan, K., Sorokin, L., Vestweber, D., Zarbock, A., Schwab, N., & Wiendl, H. (2014). VLA-4 blockade promotes differential routes into human CNS involving PSGL-1 rolling of T cells and MCAM-adhesion of TH17 cells. *J Exp Med*, *211*(9), 1833-1846. doi:10.1084/jem.20140540
- Selgrade, M. K., Cooper, G. S., Germolec, D. R., & Heindel, J. J. (1999). Linking environmental agents and autoimmune disease: an agenda for future research. *Environ Health Perspect*, *107 Suppl 5*, 811-813. doi:10.1289/ehp.99107s5811
- Serafini, B., Rosicarelli, B., Franciotta, D., Magliozzi, R., Reynolds, R., Cinque, P., Andreoni, L., Trivedi, P., Salvetti, M., Faggioni, A., & Aloisi, F. (2007). Dysregulated Epstein-Barr virus infection in the multiple sclerosis brain. *J Exp Med*, *204*(12), 2899-2912. doi:10.1084/jem.20071030
- Serafini, B., Rosicarelli, B., Magliozzi, R., Stigliano, E., Capello, E., Mancardi, G. L., & Aloisi, F. (2006). Dendritic cells in multiple sclerosis lesions: maturation stage, myelin uptake, and interaction with proliferating T cells. *J Neuropathol Exp Neurol*, *65*(2), 124-141. doi:10.1097/01.jnen.0000199572.96472.1c
- Sharpe, A. H., & Freeman, G. J. (2002). The B7-CD28 superfamily. *Nat Rev Immunol*, *2*(2), 116-126. doi:10.1038/nri727
- Shiow, L. R., Rosen, D. B., Brdickova, N., Xu, Y., An, J., Lanier, L. L., Cyster, J. G., & Matloubian, M. (2006). CD69 acts downstream of interferon-alpha/beta to inhibit S1P1 and lymphocyte egress from lymphoid organs. *Nature*, *440*(7083), 540-544. doi:10.1038/nature04606
- Shoenfeld, Y., Gilburd, B., Abu-Shakra, M., Amital, H., Barzilai, O., Berkun, Y., Blank, M., Zandman-Goddard, G., Katz, U., Krause, I., Langevitz, P., Levy, Y., Orbach, H., Pordeus, V., Ram, M., Sherer, Y., Toubi, E., & Tomer, Y. (2008). The mosaic of autoimmunity: genetic factors involved in autoimmune diseases--2008. *Isr Med Assoc J*, *10*(1), 3-7.
- Shoenfeld, Y., & Isenberg, D. A. (1989). The mosaic of autoimmunity. *Immunol Today*, *10*(4), 123-126. doi:10.1016/0167-5699(89)90245-4

- Shortman, K., & Wu, L. (1996). Early T lymphocyte progenitors. *Annu Rev Immunol*, *14*, 29-47. doi:10.1146/annurev.immunol.14.1.29
- Sigmundsdottir, H., & Butcher, E. C. (2008). Environmental cues, dendritic cells and the programming of tissue-selective lymphocyte trafficking. *Nat Immunol*, *9*(9), 981-987. doi:10.1038/ni.f.208
- Sigmundsdottir, H., Pan, J., Debes, G. F., Alt, C., Habtezion, A., Soler, D., & Butcher, E. C. (2007). DCs metabolize sunlight-induced vitamin D3 to 'program' T cell attraction to the epidermal chemokine CCL27. *Nat Immunol*, *8*(3), 285-293. doi:10.1038/ni1433
- Smith, P. M., Howitt, M. R., Panikov, N., Michaud, M., Gallini, C. A., Bohlooly, Y. M., Glickman, J. N., & Garrett, W. S. (2013). The microbial metabolites, short-chain fatty acids, regulate colonic Treg cell homeostasis. *Science*, *341*(6145), 569-573. doi:10.1126/science.1241165
- Sorensen, T. L., Tani, M., Jensen, J., Pierce, V., Lucchinetti, C., Folcik, V. A., Qin, S., Rottman, J., Sellebjerg, F., Strieter, R. M., Frederiksen, J. L., & Ransohoff, R. M. (1999). Expression of specific chemokines and chemokine receptors in the central nervous system of multiple sclerosis patients. *J Clin Invest*, *103*(6), 807-815. doi:10.1172/JCI5150
- Spits, H. (2002). Development of alphabeta T cells in the human thymus. *Nat Rev Immunol*, *2*(10), 760-772. doi:10.1038/nri913
- Spitz, F., & Furlong, E. E. (2012). Transcription factors: from enhancer binding to developmental control. *Nat Rev Genet*, *13*(9), 613-626. doi:10.1038/nrg3207
- Stoeckius, M., Zheng, S., Houck-Loomis, B., Hao, S., Yeung, B. Z., Mauck, W. M., 3rd, Smibert, P., & Satija, R. (2018). Cell Hashing with barcoded antibodies enables multiplexing and doublet detection for single cell genomics. *Genome Biol*, *19*(1), 224. doi:10.1186/s13059-018-1603-1
- Stuart, T., Butler, A., Hoffman, P., Hafemeister, C., Papalexi, E., Mauck, W. M., 3rd, Hao, Y., Stoeckius, M., Smibert, P., & Satija, R. (2019). Comprehensive Integration of Single-Cell Data. *Cell*, *177*(7), 1888-1902 e1821. doi:10.1016/j.cell.2019.05.031
- Subramanian, A., Tamayo, P., Mootha, V. K., Mukherjee, S., Ebert, B. L., Gillette, M. A., Paulovich, A., Pomeroy, S. L., Golub, T. R., Lander, E. S., & Mesirov, J. P. (2005). Gene set enrichment analysis: a knowledge-based approach for interpreting genome-wide expression profiles. *Proc Natl Acad Sci U S A*, *102*(43), 15545-15550. doi:10.1073/pnas.0506580102
- Suckale, J., Sim, R. B., & Dodds, A. W. (2005). Evolution of innate immune systems*. *Biochem Mol Biol Educ*, *33*(3), 177-183. doi:10.1002/bmb.2005.494033032466
- Summerday, N. M., Brown, S. J., Allington, D. R., & Rivey, M. P. (2012). Vitamin D and multiple sclerosis: review of a possible association. *J Pharm Pract*, *25*(1), 75-84. doi:10.1177/0897190011421839
- Takaba, H., & Takayanagi, H. (2017). The Mechanisms of T Cell Selection in the Thymus. *Trends Immunol*, *38*(11), 805-816. doi:10.1016/j.it.2017.07.010
- Tremlett, H., Yinshan, Z., & Devonshire, V. (2008). Natural history of secondary-progressive multiple sclerosis. *Mult Scler*, *14*(3), 314-324. doi:10.1177/1352458507084264
- Unutmaz, D., Xiang, W., Sunshine, M. J., Campbell, J., Butcher, E., & Littman, D. R. (2000). The primate lentiviral receptor Bonzo/STRL33 is coordinately regulated with CCR5 and its expression pattern is conserved between human and mouse. *J Immunol*, *165*(6), 3284-3292. doi:10.4049/jimmunol.165.6.3284

- Woehrl, B., Klein, M., Rupprecht, T., Schmetzer, H., Angele, B., Hacker, H., Hacker, G., Pfister, H. W., & Koedel, U. (2010). CXCL16 contributes to neutrophil recruitment to cerebrospinal fluid in pneumococcal meningitis. *J Infect Dis*, 202(9), 1389-1396. doi:10.1086/656532
- Wong, D., & Dorovini-Zis, K. (1995). Expression of vascular cell adhesion molecule-1 (VCAM-1) by human brain microvessel endothelial cells in primary culture. *Microvasc Res*, 49(3), 325-339. doi:10.1006/mvre.1995.1028
- Yang, S., Liu, F., Wang, Q. J., Rosenberg, S. A., & Morgan, R. A. (2011). The shedding of CD62L (L-selectin) regulates the acquisition of lytic activity in human tumor reactive T lymphocytes. *PLoS One*, 6(7), e22560. doi:10.1371/journal.pone.0022560
- Yednock, T. A., Cannon, C., Fritz, L. C., Sanchez-Madrid, F., Steinman, L., & Karin, N. (1992). Prevention of experimental autoimmune encephalomyelitis by antibodies against alpha 4 beta 1 integrin. *Nature*, 356(6364), 63-66. doi:10.1038/356063a0
- Zameer, A., & Hoffman, S. A. (2003). Increased ICAM-1 and VCAM-1 expression in the brains of autoimmune mice. *J Neuroimmunol*, 142(1-2), 67-74. doi:10.1016/s0165-5728(03)00262-5
- Zerrahn, J., Held, W., & Raulet, D. H. (1997). The MHC reactivity of the T cell repertoire prior to positive and negative selection. *Cell*, 88(5), 627-636. doi:10.1016/s0092-8674(00)81905-4
- Zhu, J., & Paul, W. E. (2010). Peripheral CD4+ T-cell differentiation regulated by networks of cytokines and transcription factors. *Immunol Rev*, 238(1), 247-262. doi:10.1111/j.1600-065X.2010.00951.x

9 Appendix

9.1 List of figures

Figure 1: T helper cell and T regulatory cell differentiation.	4
Figure 2: Potential routes of T cell entry into the CNS.	9
Figure 3: Photoconversion dynamics of Dendra2.	11
Figure 4: Characterization of the PhAM ^T reporter line.	38
Figure 5: Lymph node dynamics of CD4 ⁺ cells.	40
Figure 6: Migration patterns of i- and m-T cells during EAE.	42
Figure 7: Migration patterns of i-T cells at different time points during EAE.	43
Figure 8: Phenotyping of i- and m-T cells during EAE.	44
Figure 9: Antigen-specificity of i- and m-T cells during EAE.	46
Figure 10: Clonal expansion of i- and m-T cells during EAE.	48
Figure 11: Clonotype analysis of i- and m-T cells during EAE.	49
Figure 12: Phenotyping of i- and m-T cells during EAE.	51
Figure 13: Core gene signatures of i- and m-T cells during EAE.	53
Figure 14: Differentially open chromatin of i- and m-T cells during EAE.	55
Figure 15: Robust i- and m-T cell signature gene expression in alternative models.	57
Figure 16: Enrichment of distinct core signatures in i- and m-T cells during spontaneous EAE.	58
Figure 17: Distinct characteristics of i- and m-T cells in the CNS during EAE.	59
Figure 18: Distinct white versus grey matter distribution of i- and m-T cells in the CNS during EAE.	61
Figure 19: Recapitulation of distinct white matter localization of m-T cells in <i>Cxcr6</i> ^{-/-} T cells during EAE.	62
Figure 20: Potential routes of i- and m-T cells during EAE.	65
Figure 21: Mixed T cell phenotype of i- and m-T cells during EAE.	67

9.2 List of tables

Table 1: EAE scoring criteria (adapted from (Korn et al., 2007))	25
Table 2: PCR reaction mix	27
Table 3: PCR thermal cycler program for PhAM ^{floxed} and CD4-Cre mouse genotyping.	28
Table 4: PCR thermal cycler program for IL-17A-Cre mouse genotyping	28
Table 5: PCR thermal cycler program for TCR ^{MOG} /2D2 mouse genotyping	28

9.3 Attributions

The majority of the presented data in this thesis was published by (Hiltensperger et al., 2021) and permission for usage was kindly granted by Springer Nature.

Experiments with two-photon imaging of Ca²⁺ signaling in transduced T cells, shown in Figure 9b and c, were performed by Isabel J. Bauer and Naoto Kawakami.

Library preparations for scRNA-seq in Figure 10, Figure 11, Figure 12, and Figure 13 were performed by Sebastian Jarosch and scRNA-seq data was analyzed by Eduardo Beltrán.

Venn diagrams of i- and m-core signatures, shown in Figure 13b, were generated by Helena Domínguez Moreno.

ATAC-seq library preparation and analysis in Figure 14a, c, and d was performed by Helena Domínguez Moreno and analysis in Figure 14b was performed by Gildas Lepennetier.

RNA-seq library preparation in Figure 16 was performed by Rupert Öllinger and analysis was performed by Gildas Lepennetier.

Histology analyses in Figure 17a, Figure 18c, and Figure 19a and c were performed by Ravi Kant.

Sofia Tyystjärvi, Andreas Muschaweckh, Garima Garg, Lilian Aly, and Benjamin Knier helped with mouse organ collection and the preparation of single cell suspensions for some experiments and EAE mouse scoring was occasionally performed by lab members of the Korn group and Tobias Beyer of the Rothhammer group.

9.4 Acknowledgements

First, I want to thank Prof. Thomas Korn for giving me the opportunity to perform this exciting research project under his excellent supervision and for all the helpful advice and suggestions throughout my time as a doctoral candidate in his outstanding group. It has been a great pleasure for me to work in his fantastic group. I want to especially thank the members of my thesis advisory committee, Prof. Dietmar Zehn and Prof. Thomas Misgeld, for their dedication and expert feedback, which helped me to progress my doctoral project tremendously.

Special thanks go to my amazing lab mates for creating a great atmosphere at work and for their scientific and emotional support through thick and thin. I want to thank Eduardo Beltrán for his outstanding contributions to this project by performing all the scRNA-seq analyses and teaching me how to delve into that data myself. My thanks go out also to all other collaborators, without this project would not have been possible. From them I want to honor especially Ravi Kant for his fantastic histological contributions, Sofia Tyystjärvi for her tireless help during the revision phase of the publication, Helena Domínguez Moreno for her excellent ATAC-seq analyses, and Gildas Lepennetier for his computational analyses throughout the whole project. Furthermore, I would like to thank Monika Pfaller, Veronika Husterer, Esra Cetin, and Lucy Nirschl for their technical and theoretical support and for providing me with all the reagents and buffers that I needed for the project.

Finally, I want to thank my wife, Jelena, for proofreading my thesis and giving excellent feedback and for her endless support and faith in me. Thank you for everything!

Last but not least, I want to particularly thank my parents, Berti and Siegfried, and my sister, Anja, for all their tireless support during my whole studies and my life! Thank you for always listening to all my concerns and for being always there for me!